THE UNIVERSITY OF CHICAGO

K CHANNELS IN MAMMALIAN VESTIBULAR HAIR CELLS: FACILITATING RAPID SIGNALING OF HEAD MOTIONS

A DISSERTATION SUBMITTED TO
THE FACULTY OF THE DIVISION OF THE BIOLOGICAL SCIENCES
AND THE PRITZKER SCHOOL OF MEDICINE
IN CANDIDACY FOR THE DEGREE OF
DOCTOR OF PHILOSOPHY

COMMITTEE ON NEUROBIOLOGY

BY

HANNAH MARTIN

CHICAGO, ILLINOIS

AUGUST 2024

TABLE OF CONTENTS

LIST OF FIGURES

LIST OF TABLES

ACKNOWLEDGEMENTS

I would first like to thank my advisor, Ruth Anne Eatock, for creating a research environment that rewards curiosity, rigor, and teamwork. Her intelligence and conscientiousness have shaped my approach to experiments and the way I think about science. There is now a wrinkle in my prefrontal cortex labelled, “What would Ruth Anne ask.”

I have been fortunate to collaborate with many colleagues on these projects. I would like to thank our close collaborator, Anna Lysakowski, for many late nights in lab optimizing and iterating our immunocytochemistry experiments.

I’m enormously grateful to Omar Lopez-Ramirez, who so skillfully performed those challenging early experiments revealing that non-quantal transmission persisted in $K_V1.8$-null mice. Your guidance in the lab was an essential boost to my productivity.

I would like to thank Aravind Chenrayan Govindaraju for many thoughtful discussions and for exploring nonquantal transmission quantitatively, Brandie Morris Verone for diving into high-frequency vestibulo-ocular reflex, and Vicente Lumbreras for earlier work on type II hair cells.

I would like to thank Dana Silvian and Emily Scott for their partnership in our brave endeavor to set up behavioral tests and innovative analyses. I look forward to seeing the discoveries and journeys you have in science and in life.

I give a special thanks to all my labmates for sharing laughs over delicious food and commiserating over failed experiments. It’s been my pleasure seeing you all develop and watching your projects evolve as you tackle such interesting and challenging problems.

Lastly, I would like to thank the rest of my thesis committee, including Wei Wei, Dan McGehee, and Xiaoxi Zhuang, for their expert advice over the years.

ABSTRACT

In amniotes, head motions and tilt are detected by two types of vestibular hair cells (HCs) with strikingly different morphology and physiology. Type I HCs appeared in amniotes along with other adaptations to life out of water, likely to support faster vestibular signaling in the air. Mature type I HCs express a large and very unusual potassium conductance, $g_{K,L}$, which activates negative to resting potential, confers very negative resting potentials and low input resistances, and enhances a unique non-quantal transmission from type I HCs onto their calyceal afferent terminals. The molecular identity of $g_{K,L}$ has been long debated. Following clues pointing to $K_V1.8$ (KCNA10) in the Shaker K channel family as a candidate $g_{K,L}$ subunit, we compared whole-cell voltage-dependent currents from utricular hair cells of $K_V1.8$-null mice and littermate controls. We found that $K_V1.8$ was necessary not just for $g_{K,L}$ but also for fast-inactivating and delayed rectifier currents in the more ancient type II HCs, which activate positive to resting potential.

$K_V1.8$ accelerated and dampened receptor potentials in both types of hair cells, enhancing their ability to detect rapid head motions. $K_V1.8$ was essential for extending receptor potential tuning above 20 Hz and reducing delays in synaptic transmission to calyx-bearing vestibular afferents. $K_V1.8$-null mice had normal motor abilities but struggled on challenging vestibulomotor tasks such as crossing a narrow balance beam and rearing on hindlegs. In the water, where proprioceptive cues are limited, $K_V1.8$-null mice did not maintain horizontal swim posture or stable head position.

These investigations addressed a longstanding mystery about hair cell K channels and their role in type I HC-calyx transmission and vestibular function. Such features that speed up vestibular receptor potentials and non-quantal afferent transmission may have helped stabilize locomotion as tetrapods moved from water to land.

CHAPTER 1

INTRODUCTION

The vestibular inner ear transduces head motion and tilt into neural discharges corresponding to three axes of angular rotation and three axes of translational acceleration. These neural discharges linearly and accurately encode head motions to drive cerebellar and brainstem circuits that stabilize balance, posture, and gaze. To stabilize gaze, the inner ear detects head motions, and the vestibulo-ocular reflex drives ocular muscles to counter-rotate the eyes. The resulting smooth movie of the world lays the foundation for complex visually guided tasks such as swinging through trees, throwing a spear, and reading a book. To minimize lags in this seamless visual field, the vestibulo-ocular reflex spans 4-5 synapses and occurs in only 5-7 ms (Huterer & Cullen, 2002), making it one of the fastest human reflexes. A core question driving this project was understanding the structures and mechanisms in the inner ear that support such rapid signal transmission.

We study signal transmission in the mouse utricle, which detects horizontal acceleration and head tilt when these forces displace the otoconia, deflecting mechanosensitive hair bundles (**Fig. 1.1A**). Hair cells (HCs) then generate receptor potentials that drive synaptic transmission to afferent neurons, a signal transduction pathway that has been refined throughout evolution. We can gather clues about the origin of the speed of vestibular function by analyzing critical points in evolution when the need for speed increased, such as during the transition to life on land. Leaving behind water's high density and damping, amniotes experienced increased head motion power at high frequencies. These faster head motions may have outpaced existing vestibular organs' ability to keep up and faithfully drive linear head motion compensation. We posit that this selected for a new vestibular hair cell in amniotes: the type I hair cell, which extends head motion detection into higher frequency ranges.

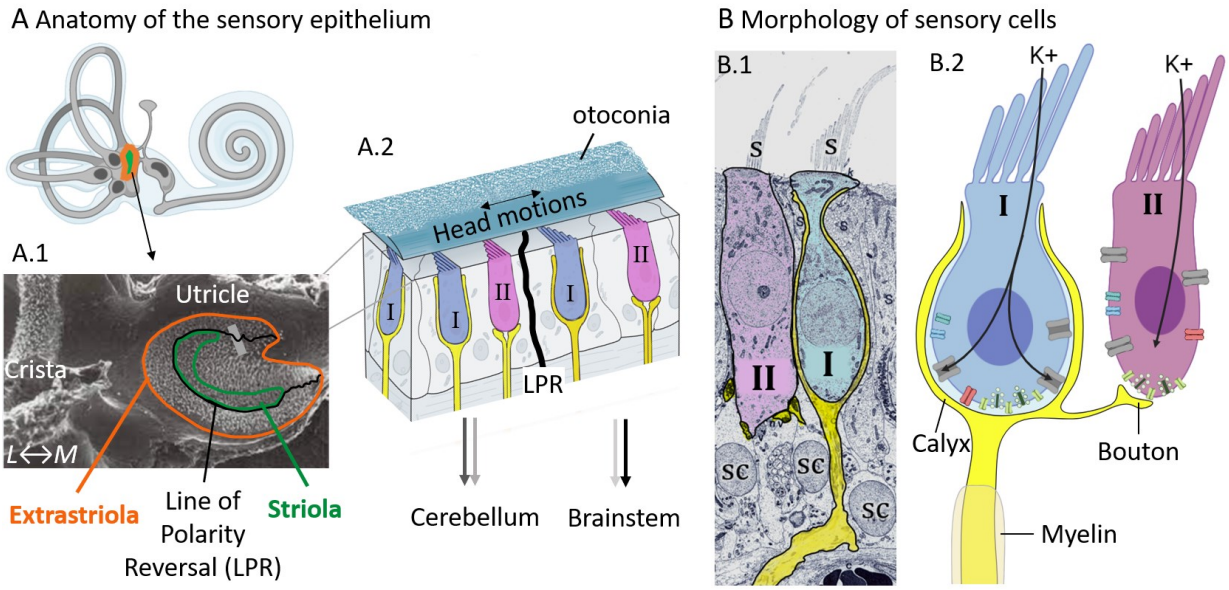

Figure 1.1. Anatomy and morphology in the utricle. (**A**) The vestibular labyrinth contains two otolith organs (saccule and utricle) and three semicircular canals. (**A.1**) Scanning electron micrograph of a hamster utricle and crista with the otoconia removed to reveal ~3000 hair bundles (adapted from Hunter-Duvar & Hinjosa, 1984). Type I and II hair cells are evenly distributed across two utricular zones: the striola (central zone, green outline) and extrastriola (peripheral zone, orange outline), which has a lateral and medial area. Hair bundles reverse orientation along the line of polarity reversal, which runs between the striola and lateral extrastriola. (**A.2**) Cartoon volume of utricular epithelia with type I (blue) and type II (purple) hair cells contacted by afferent terminals (yellow).

(**B**) Type I and II hair cells differ in morphology and postsynaptic terminal. (**B.1**) Transmission electron micrograph (adapted from Hunter-Duvar & Hinojosa, 1984). Type I HCs (blue) have large bundles of stereocilia (S), thin necks, and lower nuclei, and are wrapped by a postsynaptic calyx (yellow). Type II HCs (purple) have small bundles, a cylindrical shape, and higher nuclei, and are contacted by small boutons (yellow). Between hair cells are the thin processes of supporting cells (SC) which have nuclei below the hair cells. (**B.2**) Cartoon of type I and II hair cell with bundles deflected in the positive direction and apical-to-basal K^+ flow.

Unlike the more ancient type II hair cells present in anamniotes, type I hair cells are enveloped by a postsynaptic calyx, or cup-like, afferent terminal (**Fig. 1.1B**), and have a large, low-voltage-activated K^+ conductance, $g_{K,L}$. G (conductance) refers to a channel that conducts ions down their electrochemical gradient. Voltage-activated K channels physically open and conduct K^+ only when the membrane potential reaches a certain threshold. For $g_{K,L}$, that threshold is below the resting membrane potential of type I hair cells, meaning most $g_{K,L}$ channels are open and conductive at

rest—quite different from $g_{K,L}$'s counterparts in type II hair cells, which activate positive to rest. $g_{K,L}$ and the calyx are the most distinguishing features of the type I hair cell, and together they foster an unusual form of synaptic transmission driven by K^+ flow.

During a head motion or tilt, signals travel down the sensory transduction pathway. In brief, the hair bundle is displaced in the positive direction towards the tallest row of stereocilia, K^+ and Ca^{2+} enter, and the hair cell depolarizes, producing a receptor potential. Quantal transmission occurs when voltage-gated calcium channels open, triggering release of packets ("quanta") of glutamate that bind receptors on the postsynaptic membrane and evoke excitatory postsynaptic potentials in the afferent terminal. The most widespread afferents are dimorphic, forming both calyx and bouton terminals on type I and II hair cells, respectively (**Fig. 1.1B.2**). Bouton-only afferents are restricted to the extrastriola (**Fig. 1.1A.1**) and calyx-only afferents to the striola.

A key feature of the amniote-only type I hair cell-calyx synapse is a secondary form of synaptic transmission. Calyces foster an additional, unusual mode of synaptic transmission that doesn't rely on quantal neurotransmitter release or gap junctions, giving it the name "non-quantal transmission" (Holt et al., 2007; Songer and Eatock, 2013). First observed in 1990, non-quantal transmission seems synchronized to the hair cell receptor potential (Yamashita and Ohmori, 1990). Like the electrical synapses of reflex arcs, non-quantal transmission has the powerful ability to reduce transmission delay by bypassing the biochemical steps of neurotransmitter release. Non-quantal transmission also preserves a more linear relationship between the afferent signal and original head motion.

Recent electrophysiology and computational modeling work has added to our understanding of the mechanism behind non-quantal transmission. During a receptor potential, K^+ flows out of basolateral hair cell K channels, predominantly $g_{K,L}$, into the synaptic cleft (**Fig. 1.1B.2**). Excess

cleft K^+ depolarizes the calyx through two mechanisms that reduce standing current though low-voltage-activated K channels on the calyx inner face (Govindaraju et al., 2023). K^+ ions entering the cleft generate (1) *K^+ accumulation* that raises the K^+ equilibrium potential (E_K) (Contini et al., 2017, 2020; Lim et al., 2011), and (2) a spatially confined positive *ephaptic potential* that hyperpolarizes the transmembrane voltage only of the calyx inner face (Govindaraju et al., 2023).

In contrast, the more ancient type II hair cells are contacted by smaller bouton terminals and engage only in quantal transmission. They have more conventional delayed rectifier (g_{DR}) and fast-inactivating A-type (g_A) K^+ conductances that are opened by depolarization above resting potential (V_{rest}). Type II hair cells are thought to encode low frequency head motions, such as static tilt relative to gravity.

Low frequency head motions are preferentially transmitted by regular extrastriolar afferents, while high frequency head motions and vibrations excite irregular striolar afferents (Goldberg, 2000; Jamai et al., 2016; Tanimoto et al., 2022).

We hypothesize that $g_{K,L}$ exists in type I hair cells to provide open channels for K^+ flow into the synaptic cleft, increasing the speed and linearity of the transmitted signal (Songer and Eatock, 2013). However, until now, we haven't been able to test the relationship between $g_{K,L}$ and non-quantal transmission because we didn't know the molecular identity of $g_{K,L}$.

There have been many attempts to identify $g_{K,L}$. Various candidates included inward rectifiers, ERG, and KCNQ4 ($K_V7.4$). KCNQ4 was a strong candidate for $g_{K,L}$ for many years because it is a low-voltage-activated K channel expressed in many other cells in the inner ear (Kharkovets et al., 2000). Dominant negative experiments seemed to support KCNQ4's role as $g_{K,L}$ (Holt et al., 2007) despite earlier experiments indicating otherwise (Wong et al., 2004; Hurley et al., 2006). However, KCNQ4 was eventually ruled out with a knockout (Spitzmaul et al., 2011).

In the wake of KCNQ4, a little-known channel $K_V1.8$ (gene name KCNA10) became our new candidate. $K_V1.8^{-/-}$ mice lack the vestibular potential, a phasic response to head jerk stimuli, a sign of vestibular dysfunction in detection of high-speed head motions (Lee et al., 2013). We first noticed $K_V1.8$ when RNA-Seq experiments revealed extremely high $K_V1.8$ expression in vestibular hair cells (Scheffer et al., 2015). We further linked $K_V1.8$ to $g_{K,L}$ because the gene contains a cyclic nucleotide gated domain (Lang et al., 2000) with the potential to explain the cGMP sensitivity of $g_{K,L}$ (Chen and Eatock, 2000; Behrend et al., 1998).

In Chapter 2, we tested $K_V1.8^{-/-}$ mice for $g_{K,L}$ with whole-cell patch clamp in utricular hair cells. We found that $K_V1.8$ is necessary not just for $g_{K,L}$ but also for fast-inactivating and delayed rectifier currents in type II HCs, which activate positive to resting potential (Martin et al., 2024).

In Chapter 3, we assessed the contribution of $K_V1.8$ conductances to three levels of vestibular function: hair cell receptor potentials, synaptic transmission, and vestibulomotor behaviors. In both hair cell types, $K_V1.8$ conferred a low input resistance that was necessary for accelerating, dampening, and reducing receptor potentials. Without $K_V1.8$, lowpass corner frequencies of receptor potentials were ~20 Hz, much lower than in controls: ~370 Hz (type I hair cell) and ~70 Hz (type II hair cell). Such lower lowpass corner frequency would correspond to a deteriorated detection of high-frequency (10-100 Hz) head motions. $K_V1.8^{-/-}$ mice had impaired performance on challenging vestibulomotor tasks, such as crossing a narrow beam and rearing on hindlegs, but not basic motor tasks. In the water, where proprioceptive cues are limited, $K_V1.8^{-/-}$ mice did not maintain horizontal swim posture or stable head position. These vestibulomotor deficits likely occurred because impaired detection of high-frequency head motions in $K_V1.8^{-/-}$ mice failed to drive sufficient compensatory motions. This chapter comprises a manuscript being prepared for submission.

In Chapter 4, we investigated an artifact that can obscure measurements of mechanotransduction. In type I hair cells, extremely low input resistance degrades ideal voltage clamp, producing a false delay in the rise times of recorded mechanotransduction current. We suggest that experimenters take extra precautions to minimize this artifact in type I hair cells.

These investigations addressed a longstanding mystery about hair cell K channels and their role in type I HC-calyx transmission and vestibular circuit function. Such features that speed up vestibular receptor potentials and non-quantal afferent transmission may have helped stabilize locomotion as tetrapods moved from water to land.

CHAPTER 2

THE POTASSIUM CHANNEL SUBUNIT $K_V1.8$ (*KCNA10*) IS ESSENTIAL FOR THE DISTINCTIVE OUTWARDLY RECTIFYING CONDUCTANCES OF TYPE I AND II VESTIBULAR HAIR CELLS

2.1 ABSTRACT

In amniotes, head motions and tilt are detected by two types of vestibular hair cells (HCs) with strikingly different morphology and physiology. Mature type I HCs express a large and very unusual potassium conductance, $g_{K,L}$, which activates negative to resting potential, confers very negative resting potentials and low input resistances, and enhances an unusual non-quantal transmission from type I cells onto their calyceal afferent terminals. Following clues pointing to $K_V1.8$ (KCNA10) in the Shaker K channel family as a candidate $g_{K,L}$ subunit, we compared whole-cell voltage-dependent currents from utricular hair cells of $K_V1.8$-null mice and littermate controls. We found that $K_V1.8$ is necessary not just for $g_{K,L}$ but also for fast-inactivating and delayed rectifier currents in type II HCs, which activate positive to resting potential. The distinct properties of the three $K_V1.8$-dependent conductances may reflect different mixing with other K_V1 subunits. In $K_V1.8$-null HCs of both types, residual outwardly rectifying conductances include K_V7 (KCNQ) channels.

Current clamp records show that in both HC types, $K_V1.8$-dependent conductances increase the speed and damping of voltage responses. Features that speed up vestibular receptor potentials and non-quantal afferent transmission may have helped stabilize locomotion as tetrapods moved from water to land.

2.2 INTRODUCTION

The receptor potentials of hair cells (HCs) are strongly shaped by large outwardly rectifying K^+ conductances that are differentially expressed according to HC type. Here we report that a specific voltage-gated K^+ (K_V) channel subunit participates in very different K_V channels dominating the membrane conductances of type I and type II HCs in amniote vestibular organs.

Type I HCs occur only in amniote vestibular organs. Their most distinctive features are that they are enveloped by a calyceal afferent terminal (Wersäll, 1956; Lysakowski and Goldberg, 2004) and that they express $g_{K,L}$ (Correia and Lang, 1990; Rennie and Correia, 1994; Rüsch and Eatock, 1996a): a large non-inactivating conductance with an activation range from –100 to –60 mV, far more negative than other "low-voltage-activated" K_V channels. In addition to selectively attenuating and speeding up the receptor potentials of type I HCs (Correia et al., 1996; Rüsch and Eatock, 1996b), $g_{K,L}$ augments non-quantal transmission from type I hair cell to afferent calyx by providing open channels for K^+ flow into the synaptic cleft (Contini et al., 2012, 2017, 2020; Govindaraju et al., 2023), increasing the speed and linearity of the transmitted signal (Songer and Eatock, 2013).

Type II HCs have compact afferent synaptic contacts (boutons) where the receptor potential drives quantal release of glutamate. They have fast-inactivating (A-type, g_A) and delayed rectifier (g_{DR}) conductances that are opened by depolarization above resting potential (V_{rest}).

The unusual properties of $g_{K,L}$ have long attracted curiosity about its molecular nature. $g_{K,L}$ has been proposed to include "M-like" K_V channels in the K_V7 and/or erg channel families (Kharkovets et al., 2000; Hurley et al., 2006; Holt et al., 2007). The $K_V7.4$ subunit was of particular interest because it contributes to the low-voltage-activated conductance, $g_{K,n}$, in cochlear outer hair

cells, but was eventually eliminated as a $g_{K,L}$ subunit by experiments on $K_V7.4$-null mice (Spitzmaul et al., 2013).

Several observations suggested the $K_V1.8$ (KCNA10) subunit as an alternative candidate for $g_{K,L}$. $K_V1.8$ is highly expressed in vestibular sensory epithelia (Carlisle et al., 2012), particularly hair cells (Lee et al., 2013; Scheffer et al., 2015; McInturff et al., 2018), with slight expression elsewhere (skeletal muscle, Lee et al., 2013; kidney, Yao, 2002). $K_V1.8^{-/-}$ mice show absent or delayed vestibular-evoked potentials, the synchronized activity of afferent nerve fibers sensitive to fast linear head motions (Lee et al., 2013). Unique among K_V1 channels, $K_V1.8$ has a cyclic nucleotide binding domain (Lang et al., 2000) with the potential to explain $g_{K,L}$'s known cGMP dependence (Behrend et al., 1997; Chen and Eatock, 2000).

Our comparison of whole-cell currents and immunohistochemistry in type I HCs from $K_V1.8^{-/-}$ and $K_V1.8^{+/+,+/-}$ mouse utricles confirmed that $K_V1.8$ expression is necessary for $g_{K,L}$. More surprisingly, $K_V1.8$ expression is also required for A-type and delayed rectifier conductances of type II HCs. In both HC types, eliminating the $K_V1.8$-dependent major conductances revealed a smaller delayed rectifier conductance involving K_V7 channels. Thus, the distinctive outward rectifiers that produce such different receptor potentials in type I and II HCs both include $K_V1.8$ and K_V7 channels.

2.3 RESULTS

We compared whole-cell voltage-activated K^+ currents in type I and type II hair cells from homozygous knockout ($K_V1.8^{-/-}$) animals and their wildtype ($K_V1.8^{+/+}$) or heterozygote ($K_V1.8^{+/-}$) littermates. We immunolocalized $K_V1.8$ subunits in the utricular epithelium and pharmacologically characterized the residual K^+ currents of $K_V1.8^{-/-}$ animals. Current clamp experiments demonstrated the impact of $K_V1.8$-dependent currents on passive membrane properties.

We recorded from three utricular zones: lateral extrastriola (LES), striola, and medial extrastriola (MES) (**Fig. 2.3A.1**); striolar and extrastriolar zones have many structural and functional differences and give rise to afferents with different physiology (reviewed in Goldberg, 2000; Eatock and Songer, 2011). Recordings are from 412 type I and II HCs (53% LES, 30% MES, 17% striola) from mice between postnatal day (P) 5 and P370. We recorded from such a wide age range to test for developmental or senescent changes in the impact of the null mutation. Above P18, we did not see substantial changes in K_V channel properties, as reported (González-Garrido et al., 2021).

As reported (Lee et al., 2013), $K_V1.8^{-/-}$ animals appeared to be healthy and to develop and age normally.

$K_V1.8$ is necessary for $g_{K,L}$ in type I hair cells

The large low-voltage activated conductance, $g_{K,L}$, in $K_V1.8^{+/+,+/-}$ type I hair cells produces distinctive whole-cell current responses to voltage steps, as highlighted by our standard type I voltage protocol (**Fig. 2.1A**). From a holding potential within the $g_{K,L}$ activation range (here –74 mV), the cell is hyperpolarized to –124 mV, negative to E_K and the activation range, producing a

large inward current through open $g_{K,L}$ channels that rapidly decays as the channels deactivate. The large transient inward current is a hallmark of $g_{K,L}$. The hyperpolarization serves to close all channels, then probe the activation function with a series of depolarizing steps, obtaining the max conductance from the peak tail current at –44 mV (**Fig. 2.1A).** When $g_{K,L}$ is present, step depolarizations positive to the midpoint voltage produce tail currents that decay rapidly due to substantial K^+ accumulation in the calyceal cleft (Lim et al., 2011). We detected no difference between the Boltzmann parameters of $g_{K,L}$ G-V curves from $K_V1.8^{+/-}$ and $K_V1.8^{+/+}$ type I HCs.

For a similar voltage protocol, $K_V1.8^{-/-}$ type I HCs (**Fig. 2.1B**) produced no inward transient current at the step from –74 mV to –124 mV and much smaller depolarization-activated currents during the iterated steps, even at much more positive potentials. Figure 2.1C compares the conductance-voltage (G-V, activation) curves fit to tail currents (Eq. 2.1; see insets in **Fig. 2.1A-B**): the maximal conductance (g_{max}) of the $K_V1.8^{-/-}$ HC was over 10-fold smaller (**Fig. 2.1C.1**), and the curve was positively shifted by >40 mV (**Fig. 2.1C.2**). **Figure 2.1D** shows the G-V Boltzmann fit parameters for type I HCs from mice >P12, an age at which type I HCs normally express $g_{K,L}$ (Rüsch et al., 1998).

Suppl. Fig. S2.1 shows how G-V parameters of outwardly rectifying currents in type I HCs changed from P5 to P360. In $K_V1.8^{+/+,+,-}$ mice, the parameters transitioned over the first 15-20 postnatal days from values for a conventional delayed rectifier, activating positive to resting potential, to $g_{K,L}$ values, as previously described (Rüsch et al., 1998; Géléoc et al., 2004; Hurley et al., 2006). Between P5 and P10, some type I HCs have not yet acquired $g_{K,L}$, and the delayed rectifiers present were not detectably affected by $K_V1.8$ deletion (**Suppl. Fig. S2.1B**). In $K_V1.8^{-/-}$ type I HCs, $g_{K,L}$ was absent and G-V parameters did not change much with age from P5 to P370.

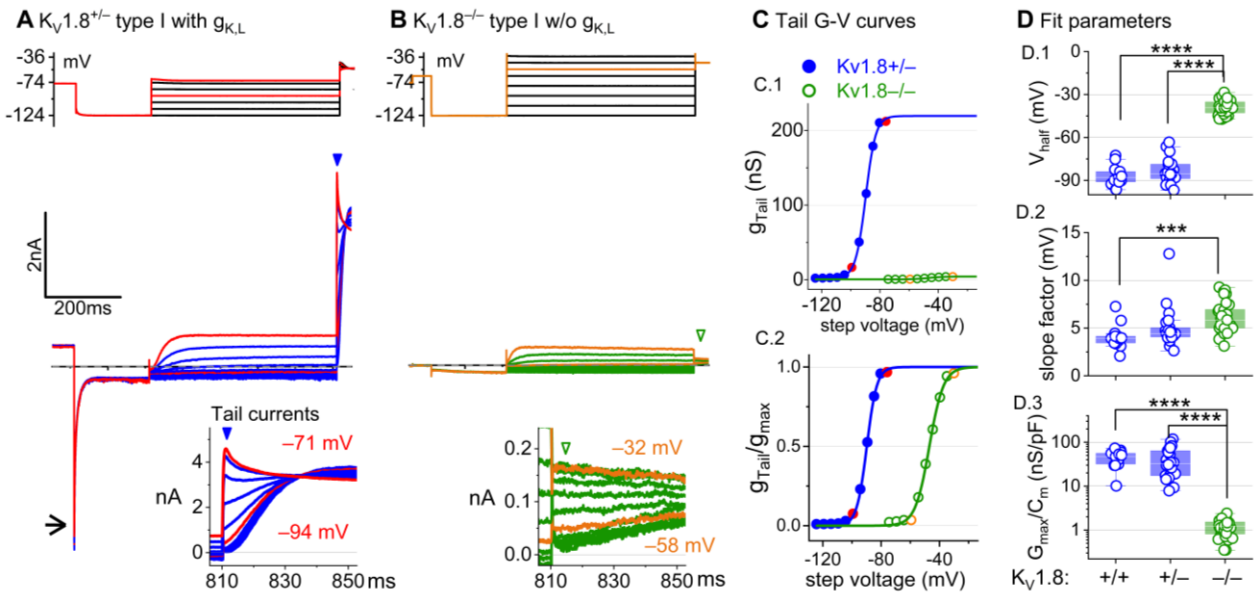

Figure 2.1. $K_V1.8^{-/-}$ type I hair cells lacked $g_{K,L}$, the dominant conductance in mature $K_V1.8^{+/+,+/-}$ type I HCs. Representative voltage-evoked currents in **(A)** a P22 $K_V1.8^{+/-}$ type I HC and **(B)** a P29 $K_V1.8^{-/-}$ type I HC. (A) *Arrow,* transient inward current that is a hallmark of $g_{K,L}$. Note that the voltage protocol (top) in B extends to more positive voltages. *Arrowheads,* tail currents, magnified in *insets*. **(C)** Activation (G-V) curves from tail currents in A and B; symbols, data; curves, Boltzmann fits (Eq. 2.1). **(D)** Fit parameters from mice >P12 show big effect of $K_V1.8^{-/-}$ and no difference between $K_V1.8^{+/-}$ and $K_V1.8^{+/+}$. *Asterisks* (here and elsewhere): *, $p<0.05$; **, $p<0.01$; ***, $p<0.001$; and ****, $p<0.0001$. *Line,* median; *Box,* interquartile range; *Whiskers*, outliers. See Table 2.1 for statistics.

The much smaller residual delayed rectifier activated positive to resting potential, with V_{half} ~– 40 mV and g_{max} density of 1.3 nS/pF. We characterize this $K_V1.8$-independent delayed rectifier later. A much larger non-$g_{K,L}$ delayed rectifier conductance ("$g_{DR,I}$") was reported in our earlier publication on mouse utricular type I HCs (Rüsch et al., 1998). This current was identified as that remaining after "blocking" $g_{K,L}$ with 20 mM external Ba^{2+}. Our new data suggest that there is no large non-$g_{K,L}$ conductance, and that instead high Ba^{2+} positively shifted the apparent voltage dependence of $g_{K,L}$.

$K_V1.8$ strongly affects type I passive properties and responses to current steps. While the cells of $K_V1.8^{-/-}$ and $K_V1.8^{+/-}$ epithelia appeared healthy, type I hair cells had smaller membrane capacitances (C_m) and presumably surface areas: 4-5 pF in $K_V1.8^{-/-}$ type I HCs, ~20% smaller than $K_V1.8^{+/-}$ type I HCs (~6 pF) and ~30% smaller than $K_V1.8^{+/+}$ type I HCs (6-7 pF; **Table 2.2**). The

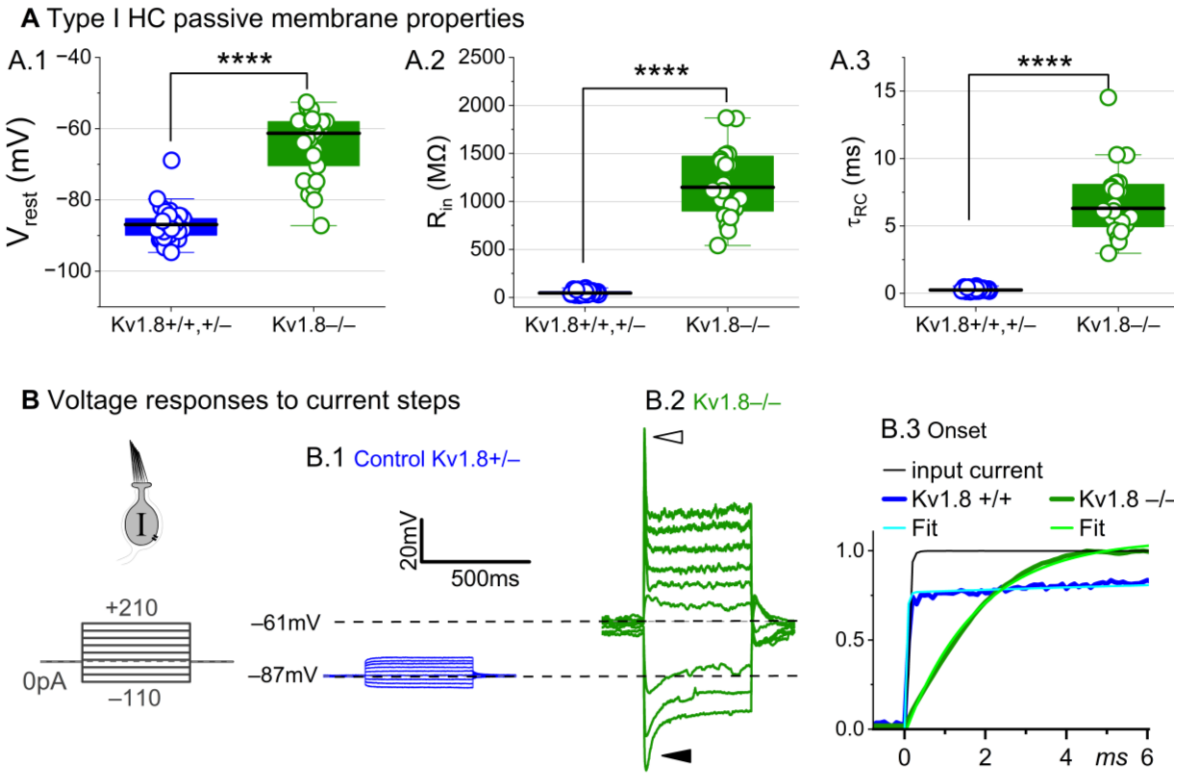

Figure 2.2. $K_V1.8^{-/-}$ type I hair cells had much longer membrane charging times and higher input resistances (voltage gains) than $K_V1.8^{+/+,+/-}$ type I HCs. (A) $g_{K,L}$ strongly affects passive membrane properties: (**A.1**) V_{rest} , (**A.2**) R_{in}, input resistance, and (**A.3**) membrane time constant, $t_{RC} = (R_{input} * C_m)$. See Table 2.2 for statistics. **(B)** Current clamp responses to the same scale from (B.1) $K_V1.8^{+/-}$ and (B.2) $K_V1.8^{-/-}$ type I cells, both P29. *Filled arrowhead (B.2),* sag indicating I_H activation. *Open arrowhead*, Depolarization rapidly decays as I_{DR} activates. B.3, The 1st 6 ms of voltage responses to 170-pA injection is normalized to steady-state value; overlaid curves are double-exponential fits ($K_V1.8^{+/+}$, τ 40 ms and 2.4 ms) and single-exponential fits ($K_V1.8^{-/-}$, τ 1.1 ms) .

decreased C_m may reflect deletion of a highly expressed trans-membrane protein (see discussion of $g_{K,L}$ channel density in Chen and Eatock, 2000, and for comparison the large decrease in outer hair cell size in the prestin null mutant (Liberman et al., 2002; Takahashi et al., 2018)).

Basolateral conductances help set the resting potential and passive membrane properties that regulate the time course and gain of voltage responses to small currents. To examine the effect of $K_V1.8$ on these properties, we switched to current clamp mode and measured resting potential (V_{rest}), input resistance (R_{in}, equivalent to voltage gain for small current steps, $\triangle V/\triangle I$), and membrane time constant (τ_{RC}). In $K_V1.8^{-/-}$ type I HCs, V_{rest} was much less negative (**Fig. 2.2A.1**),

R_{in} was greater by ~20-fold (**Fig. 2.2A.2**), and membrane charging times were commensurately longer (**Fig. 2.2A.3**).

The differences between the voltage responses of $K_V1.8^{+/+,+/-}$ and $K_V1.8^{-/-}$ type I HCs are expected from the known impact of $g_{K,L}$ on V_{rest} and R_{in} (Correia and Lang, 1990; Ricci et al., 1996; Rüsch and Eatock, 1996b; Songer and Eatock, 2013). The large K^+-selective conductance at V_{rest} holds V_{rest} close to E_K (K^+ equilibrium potential) and minimizes gain ($\triangle V/\triangle I$), such that voltage-gated conductances are negligibly affected by the input current and the cell produces approximately linear, static responses to iterated current steps. For $K_V1.8^{-/-}$ type I HCs, with their less negative V_{rest} and larger R_{in}, positive current steps evoked a fast initial depolarization (**Fig. 2.2B.2**), activating residual delayed rectifiers and repolarizing the membrane toward E_K. Negative current steps evoked an initial "sag" (**Fig. 2.2B.2**), a hyperpolarization followed by slow repolarization as the HCN1 channels open (Rüsch and Eatock, 1996b).

Overall, comparison of the $K_V1.8^{+/+,+/-}$ and $K_V1.8^{-/-}$ responses shows that with $K_V1.8$ ($g_{K,L}$), the voltage response of the type I hair cell is smaller but better reproduces the time course of the input current.

$K_V1.8$ is necessary for both inactivating and non-inactivating K_V currents in type II hair cells

Type II HCs also express $K_V1.8$ mRNA (McInturff et al., 2018; Orvis et al., 2021). Although their outwardly-rectifying conductances (g_A and g_{DR}) differ substantially in voltage dependence and size from $g_{K,L}$, both conductances were strongly affected by the null mutation: g_A was eliminated

Table 2.1. *Type I hair cell K_V activation voltage dependence and kinetics. Mean ± SEM (number of cells). g is effect size, Hedge's g. KWA is Kruskal-Wallis ANOVA.*

Zone	K_V1.8	Tail $V_{1/2}$, mV [a]	Tail S, mV [b]	Tail G_{max}, nS [c]	Tail G_{max}/C_m, nS/pF [d]	Age (median, range)
Extrastriola	+/+	–85 ± 2 (12)	4.3 ± 0.4 (12)	270 ± 40 (11)	47 ± 8 (11)	22, 14-287
	+/–	–83 ± 1 (40)	5.2 ± 0.3 (40)	210 ± 20 (40)	37 ± 4 (40)	19, 13-259
	–/–	–40.2 ± 0.9 (26)	5.7 ± 0.3 (26)	5.4 ± 0.3 (26)	1.11 ± 0.08 (26)	45, 14-277
Striola	+/+	–87 ± 3 (6)	4.3 ± 0.3 (6)	310 ± 70 (6)	41 ± 7 (6)	40, 15-59
	+/–	–88 ± 2 (3)	4.7 ± 0.9 (3)	270 ± 60 (3)	44 ± 6 (3)	19, 14-20
	–/–	–38 ± 1 (13)	6.2 ± 0.4 (13)	6.5 ± 0.6 (13)	1.5 ± 0.1 (13)	202, 14-370

[a] –/– vs +/+: 2-way ANOVA, p < 1E-9, g 7.7; –/– vs +/–: 2-way ANOVA, p < 1E-9, g 6.8
[b] –/– vs +/+: 2-way ANOVA, p = 8.4E-4, g 1.2
[c] –/– vs +/+: 2-way ANOVA, p < 1E-9, g 3.7; –/– vs +/–: 2-way ANOVA, p < 1E-9, g 2.1
[d] –/– vs +/+: 2-way ANOVA, p < 1E-9, g 3.6; –/– vs +/–: 2-way ANOVA, p < 1E-9, g 2.0

Table 2.2. *Type I hair cell* p*assive membrane properties. Mean ± SEM (number of cells). g is effect size, Hedge's g. KWA is Kruskal-Wallis ANOVA.*

Zone	*K_V1.8*	*V_{rest}, mV* [a, b]	R_{input}, MΩ [c]	τ_{RC}, ms [d]	C_m (pF) [e]	Age (median, range)
Extrastriola	+/+	–84 ± 3 (6)	44 ± 6 (6)	0.24 ± 0.03 (6)	6.1 ± 0.4 (13)	19.5, 14-287
	+/–	–88.0 ± 0.7 (28)	55 ± 5 (24)	0.32 ± 0.03 (23)	5.8 ± 0.2 (44)	21, 16-29
	–/–	–63 ± 2 (15)	1400 ± 100 (15)	6.4 ± 0.6 (15)	5 ± 0.2 (27)	45, 14-202
Striola	+/+	–87 ± 2 (4)	50 ± 8 (4)	0.30 ± 0.04 (4)	7.4 ± 0.7 (7)	43, 40-59
	+/–	–87 ± 3 (3)	38 ± 8 (2)	0.21 ± 0.01 (2)	5.9 ± 0.6 (3)	19, 19-20
	–/–	–74 ± 5 (5)	1000 ± 300 (4)	4.2 ± 1.0 (4)	4.4 ± 0.2 (14)	202, 24-370

[a] striolar –/– vs ES –/–: 2-way ANOVA, p = 0.006, g 1.2; striolar –/– vs striolar +/+,+/–: 2-way ANOVA, p = 0.005, g 1.7
[b] –/– vs +/+: 2-way ANOVA, p < 1E-9, g 2.3; –/– vs +/–: 2-way ANOVA, p < 1E-9, g 3.4
[c] –/– vs +/+: 2-way ANOVA, p < 1E-9, g 3.1; –/– vs +/–: 2-way ANOVA, p < 1E-9, g 3.9
[d] –/– vs +/+: 2-way ANOVA, p < 1E-9, g 2.7; –/– vs +/–: 2-way ANOVA, p < 1E-9, g 3.4
[e] –/– vs +/+: 2-way ANOVA, p = 3E-7, g 1.5; –/– vs +/–: 2-way ANOVA, p = 1.3E-4, g 1.0; +/– vs +/+: 2-way ANOVA, p = 0.048, g 0.6

and the delayed rectifier was substantially smaller. Below we describe g_A and g_{DR} in $K_V1.8^{+/+,+/-}$ type II HCs and the residual outward rectifying current in $K_V1.8^{-/-}$ type II HCs.

$K_V1.8^{+/+,+/-}$ type II HCs. Most (81/84) $K_V1.8^{+/+,+/-}$ type II HCs expressed a rapidly-activating, rapidly-inactivating A-type conductance (g_A). We define A current as the outwardly rectifying

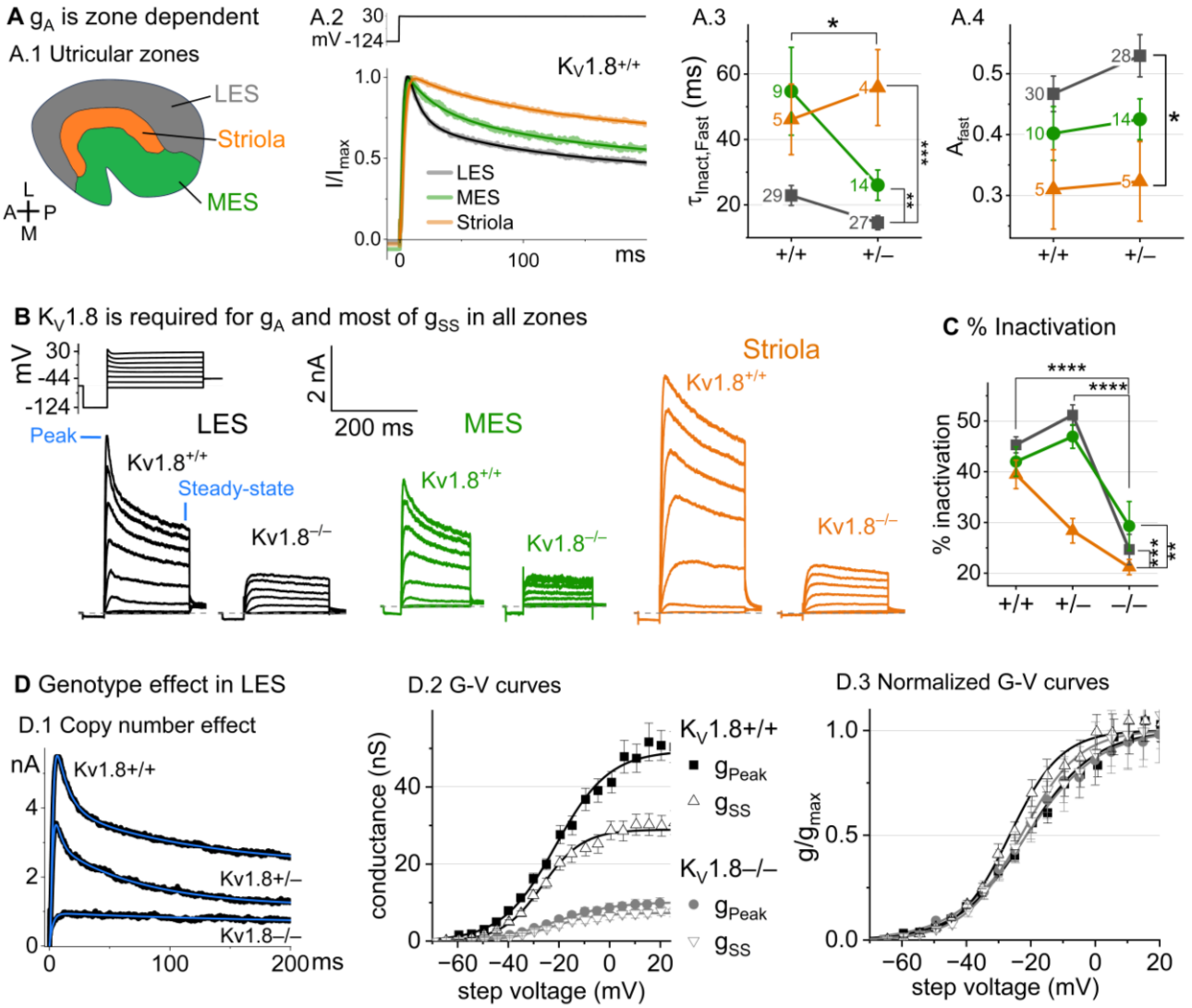

Figure 2.3. $K_V1.8^{-/-}$ type II HCs in all zones of the sensory epithelium lacked the major rapidly inactivating conductance, g_A, and had less delayed rectifier conductance. Activation and inactivation varied with epithelial zone and genotype. (**A**) g_A inactivation time course varied across zones. (**A.1**) Zones of the utricular epithelium. (**A.2**) Normalized currents evoked by steps from –124 mV to +30 mV with overlaid fits of Eq. 3. (**A.3**) $t_{Inact,Fast}$ was faster in $K_V1.8^{+/-}$ than $K_V1.8^{+/+}$ HCs , and faster in LES than other zones. Brackets show post hoc pairwise comparisons between two zones (vertical brackets) and horizontal brackets compare two genotypes; see Table 2.3 for statistics. (**A.4**) Fast inactivation was a greater fraction of total inactivation in LES than striola. (**B**) Exemplars; ages, *left to right*, P312, P53, P287, P49, P40, P154. (**C**) % inactivation at 30 mV was much lower in $K_V1.8^{-/-}$ than $K_V1.8^{+/-}$ and $K_V1.8^{+/+}$, and lower in striola than LES and MES. Interaction between zone and genotype was significant (Table 2.3). (**D**) Exemplar currents and G-V curves from LES type II HCs show a copy number effect. (**D.1**) Currents for examples of the 3 genotypes evoked by steps from –124 mV to +30 mV fit with Eq. 3. (**D.2**) Averaged peak and steady-state conductance-voltage datapoints from LES cells (+/+, n=37; –/–, n=20) were fit with Boltzmann equations (Eq. 1) and normalized by g_{max} in (**D.3**). See Table 2.4 for statistics.

current that inactivates by over 30% within 200 ms. g_A was more prominent in extrastriolar zones, as reported (Holt et al. 1999, Weng and Correia 1999).

We compared the activation and inactivation time course and inactivation prominence for 200-ms steps from –124 mV to ~30 mV. Outward currents fit with Eq. 2.3 yielded fast inactivation time constants ($\tau_{Inact, Fast}$) of ~30 ms in LES (**Fig. 2.3A.2**). $\tau_{Inact, Fast}$ was faster in LES than in MES or striola (**Fig. 2.3A.3**) and fast inactivation was a larger fraction of the total inactivation in LES than striola (~0.5 vs. 0.3, **Fig. 2.3A.4**).

To show voltage dependence of activation, we generated G-V curves for peak currents (sum of A-current and delayed rectifier) and steady-state currents measured at 200 ms, after g_A has mostly inactivated (**Fig. 2.3D.2**). $K_V1.8^{+/–}$ HCs had smaller currents than $K_V1.8^{+/+}$ HCs, reflecting a smaller g_{DR} (**Fig. 2.3D**) and faster fast inactivation (**Fig. 2.3A.3**). As discussed later, these effects may relate to effects of the $K_V1.8$ gene dosage on the relative numbers of different $K_V1.8$ heteromers.

For $K_V1.8^{+/+}$ and $K_V1.8^{+/–}$ HCs, the voltage dependence as summarized by V_{half} and slope factor (S) was similar. Relative to g_{SS}, g_{Peak} had a more positive V_{half} (~–21 vs. ~–26) and greater S (~12 vs. ~9, **Fig. 2.3D**, **Table 2.4**). Because g_{Peak} includes channels with and without fast inactivation, the shallower g_{Peak}-V curve may reflect a more heterogeneous channel population. Only g_{Peak} showed zonal variation, with more positive V_{half} in LES than striola (~–20 mV vs. ~–24 mV, **Fig. 2.3D**, **Table 2.4**). We later suggest that variable subunit composition may drive zonal variation in g_{Peak}.

$K_V1.8^{–/–}$ type II HCs from all zones were missing g_A and 30-50% of g_{DR} (**Fig. 2.3B-D**). The residual delayed rectifier (1.3 nS/pF) had a more positive V_{half} than g_{DR} in $K_V1.8^{+/+,+/–}$ HCs (~–20 mV *vs.* ~–26 mV, **Fig. 2.3D.2**). We refer to the $K_V1.8$-dependent delayed rectifier component as $g_{DR}(K_V1.8)$ and to the residual, $K_V1.8$-*in*dependent delayed rectifier component as $g_{DR}(K_V7)$ because, as we show later, it includes K_V7 channels.

Supplemental Figure S2.3A shows the development of $K_V1.8$-dependent and independent K_V currents in type II HCs with age from P5 to over P300. In $K_V1.8^{+/+,+/-}$ type II HCs, g_A was present at all ages with a higher % inactivation after P18 than at P5-P10 (**Suppl. Fig. S2.3A.4**). g_{Peak} did not change much above P12 except for a compression of conductance density from P13 to P370 (partial correlation coefficient = –0.4, p = 2E-5, **Suppl. Fig. S2.3A.3**).

We saw small rapidly inactivating outward currents in a minority of $K_V1.8^{-/-}$ type II HCs (23%, 7/30), all >P12 and extrastriolar (**Suppl. Fig. S2.4**). These currents overlapped with g_A in percent inactivation, inactivation kinetics, and activation voltage dependence but were very small. As discussed later, we suspect that these currents flow through homomers of inactivating K_V subunits that in control hair cells join with $K_V1.8$ subunits and confer inactivation on the heteromeric conductance.

$K_V1.8$ affects type II passive properties and responses to current steps.

In type II HCs, absence of $K_V1.8$ did not change V_{rest} (**Fig. 2.4A.1)** because g_A and g_{DR} both activate positive to rest, but significantly increased R_{in} and τ_{RC} (**Fig. 2.4A.2-A.3**).

Positive current steps evoked an initial depolarizing transient in both $K_V1.8^{+/+}$ and $K_V1.8^{-/-}$ type II HCs, but the detailed time course differed (**Fig. 2.4B**). Both transient and steady-state responses were larger in $K_V1.8^{-/-}$, consistent with their larger R_{in} values.

Table 2.3. *Type II hair cell K_V currents: Activation and inactivation time course at +30 mV. Mean ± SEM. g is effect size, Hedge's g. KWA is Kruskal-Wallis ANOVA.*

Zone	K_V1.8	τ_{Act} at 30 mV, ms [a, b]	$\tau_{Inact,Fast}$ at 30 mV, ms [c, d]	Fast inactivation prominence [e]	Inactivation % [f, g]	N cells	Age (median, range)
LES	+/+	2.11 ± 0.09	23 ± 3	0.46 ± 0.03	45 ± 2	30	46, 14-312
	+/–	1.64 ± 0.09	15 ± 2	0.53 ± 0.03	51 ± 2	27	29, 13-280
	–/–	4.4 ± 0.5	*NA*	*NA*	25 ± 3	21	128, 15-355
MES	+/+	2.8 ± 0.5	50 ± 10	0.40 ± 0.04	42 ± 3	9	94, 22-296
	+/–	2.2 ± 0.2	90 ± 60	0.42 ± 0.03	47 ± 2	15	24, 13-52
	–/–	10 ± 7	*NA*	*NA*	29 ± 5	10	84, 28-355
Striola	+/+	2.7 ± 0.3	50 ± 10	0.31 ± 0.07	39 ± 3	5	45, 40-287
	+/–	2.9 ± 0.4	300 ± 200	0.3 ± 0.06	28 ± 2	5	19, 14-30
	–/–	7 ± 2	*NA*	*NA*	22 ± 2	6	202, 29-298

[a] –/– vs +/+: KWA, p = 0.0048, g 0.6; –/– vs +/–: KWA, p = 2.3E-7, g 0.6
[b] Striola vs LES: KWA, p = 5.7E-4, g 1.0
[c] +/– vs +/+: KWA, p = 0.027, g 0.2
[d] LES vs MES: KWA, p = 0.0018, g 0.3; LES vs Striola: KWA, p = 1.9E-4, g 0.8
[e] LES vs Striola: 2-way ANOVA, p = 0.0041, g 0.7
[f] –/– vs +/+: 2-way ANOVA, p < 1E-9, g 1.7; –/– vs +/–: 2-way ANOVA, p < 1E-9, g 1.8
[g] Striola vs LES: 2-way ANOVA, p = 3.4E-5, g 0.9; Striola vs MES: 2-way ANOVA, p = 0.0011, g 1.0; Interaction between genotype and Zone: 2-way ANOVA, p = 0.026

Table 2.4. *Type II hair cell K_V currents: Activation voltage dependence. Mean ± SEM. g is effect size, Hedge's g. KWA is Kruskal-Wallis ANOVA.*

Zone	*K_V1.8*	*Peak $V_{1/2}$, mV* [a]	Peak S, mV [b, c]	A-type g_{max}/C_m, nS/pF [d]	SS V_{half}, mV [e]	SS S, mV [f]	SS g_{max}/C_m, nS/pF [g, h]	N cells	Age (median, range)
LES	+/+	–19.8 ± 0.6	11.8 ± 0.4	4.0 ± 0.3	–25.0 ± 0.5	8.7 ± 0.3	7.1 ± 0.8	37	46, 14-312
	+/–	–19.8 ± 0.8	12.8 ± 0.4	3.8 ± 0.3	–26.8 ± 0.8	8.7 ± 0.3	4.9 ± 0.4	35	29, 13-280
	–/–	–18 ± 1	11.7 ± 0.4	0.37 ± 0.05	–19 ± 1	12.1 ± 0.5	1.8 ± 0.2	20	128, 15-355
MES	+/+	–22 ± 1	11 ± 0.7	4.1 ± 0.7	–26 ± 1	8.3 ± 0.5	9 ± 1	11	94, 22-296
	+/–	–21 ± 1	11.8 ± 0.4	3.6 ± 0.5	–27 ± 1	9.0 ± 0.3	5.9 ± 0.7	16	24, 13-52
	–/–	–19 ± 1	10.8 ± 0.6	0.6 ± 0.1	–20 ± 1	10.7 ± 0.7	2.5 ± 0.3	15	84, 28-355
Striola	+/+	–24 ± 1	9.6 ± 0.5	5 ± 1	–26.6 ± 0.9	8.2 ± 0.4	12 ± 1	7	45, 40-287
	+/–	–25 ± 2	9.4 ± 0.4	2.6 ± 0.6	–28 ± 2	8.2 ± 0.3	10 ± 2	6	19, 14-30
	–/–	–21.3 ± 0.9	10.3 ± 0.5	0.7 ± 0.1	–21.7 ± 0.8	10.5 ± 0.6	3.9 ± 0.5	8	202, 29-298

[a] Striola vs LES: 2-way ANOVA, p = 0.00116, g 0.9
[b] Striola vs MES: 2-way ANOVA, p = 0.016, g 0.8; Striola vs LES: 2-way ANOVA, p = 7.5E-6, g 1.2
[c] –/– vs +/–: 2-way ANOVA, p = 0.036, g 0.5
[d] –/– vs +/+: Welch ANOVA, p < 1E-9, g 2.3; –/– vs +/–: Welch ANOVA, p < 1E-9, g 2.3
[e] –/– vs +/+: 2-way ANOVA, p < 1E-9, g 1.4; –/– vs +/–: 2-way ANOVA, p < 1E-9, g 1.6
[f] –/– vs +/+: 2-way ANOVA, p < 1E-9, g 1.4; –/– vs +/–: 2-way ANOVA, p = 4.5E-7, g 1.1
[g] –/– vs +/+: Welch ANOVA, p < 1E-9, g 1.6; –/– vs +/–: Welch ANOVA, p < 1E-9, g 1.3; +/+ vs +/–: Welch ANOVA, p = 0.007, g 1.6
[h] Striola vs LES: 1-way ANOVA, p = 0.001, g 0.9); Striola vs MES: 1-way ANOVA, p = 0.01, g 0.8

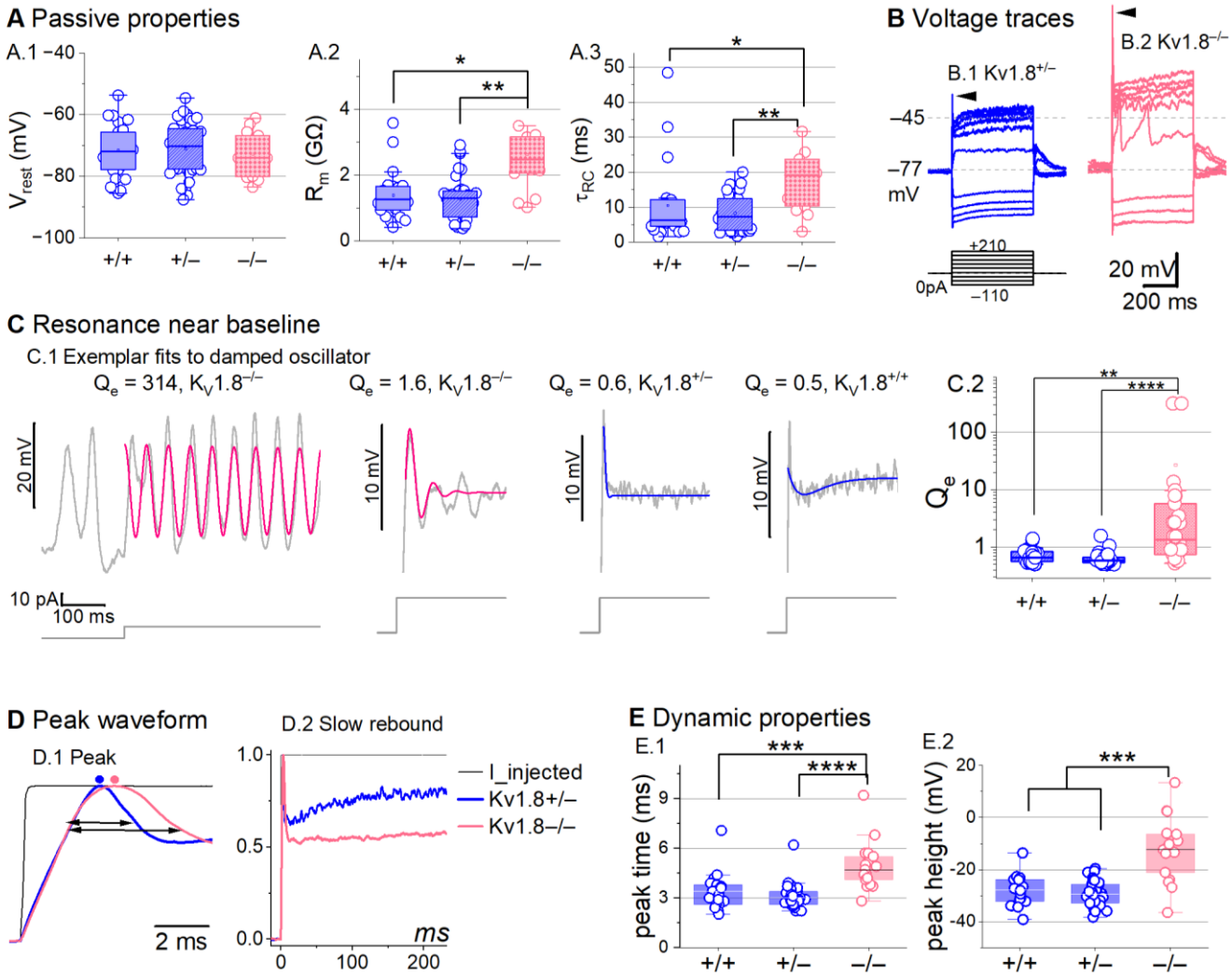

Figure 2.4. $K_V1.8^{-/-}$ type II hair cells had larger, slower voltage responses and more electrical resonance. **(A)** Passive membrane properties near resting membrane potential: A.1) Resting potential. R_{input} (A.2) and τ_{RC} (A.3) were obtained from single exponential fits to voltage responses < 15 mV. See Table 2.5 for statistics. **(B)** Exemplar voltage responses to iterated current steps (*bottom)* illustrate key changes in gain and resonance with $K_V1.8$ knockout. **(B.1)** $K_V1.8^{+/-}$ type II HC (P24, LES) and **(B.2)** $K_V1.8^{-/-}$ type II HC (P53, LES). *Arrowheads,* depolarizing transients. **(C)** Range of resonance illustrated for $K_V1.8^{-/-}$ type II HCs (*left, pink curves fit to Eq. 5*) and controls (*right, blue fits*). **(C.1)** *Resonant frequencies, left to right:* 19.6, 18.4, 34.4, 0.3 Hz. Leftmost cell resonated spontaneously (before step). **(C.2)** Tuning quality (Q_e; Eq. 2.6) was higher for $K_V1.8^{-/-}$ type II HCs (KWA, p = 0.0064 vs. $K_V1.8^{+/+}$; p = 7E-8 vs. $K_V1.8^{+/-}$). **(D)** $K_V1.8^{-/-}$ type II HCs had higher, slower peaks and much slower rebound potentials in response to large (170-pA) current steps. **(D.1)** Normalized to show initial depolarizing transient (*filled circles*, times of peaks; *horizontal arrows*, peak width at half-maximum). **(D.2)** Longer time scale to highlight how null mutation reduced post-transient rebound. **(E)** In $K_V1.8^{-/-}$ HCs, depolarizing transients evoked by a +90-pA step were slower to peak **(E.1)** and **(E.2)** larger.

Absence of $K_V1.8$ increased the incidence of sharp electrical resonance in type II HCs.

Electrical resonance, which manifests as ringing responses to current steps, can support receptor

Table 2.5. *Type II hair cell passive membrane properties. Mean ± SEM (number of cells). g is effect size, Hedge's g. KWA is Kruskal-Wallis ANOVA.*

Zone	$K_V1.8$	V_{rest}, mV	R_{input}, GΩ [a]	τ_{RC}, ms [b]	Peak height, mV, 170 [c]	Peak time, ms [d]	C_m, pF	Age (median, range)
Extrastriola	+/+	–71 ± 2 (19)	1.4 ± 0.2 (16)	11 ± 3 (16)	–20 ± 2 (15)	2.5 ± 0.2 (15)	4.7 ± 0.2 (50)	45, 16-312
	+/–	–71 ± 2 (34)	1.2 ± 0.1 (27)	9 ± 1 (27)	–20 ± 1 (30)	2.44 ± 0.08 (30)	4.6 ± 0.1 (52)	27, 13-280
	–/–	–76 ± 2 (9)	2.3 ± 0.3 (7)	16 ± 3 (7)	2 ± 6 (7)	3.6 ± 0.3 (7)	4.6 ± 0.2 (35)	53, 15-154
Striola	+/+	–73.1 ± 1.0 (6)	1.4 ± 0.1 (6)	9 ± 1 (6)	–20 ± 2 (5)	2.7 ± 0.1 (5)	4.6 ± 0.2 (7)	45, 40-224
	+/–	–71 ± 3 (5)	1.4 ± 0.3 (6)	7 ± 2 (6)	–20 ± 2 (6)	2.3 ± 0.1 (6)	4.8 ± 0.2 (6)	19, 19-30
	–/–	–68 ± 2 (6)	3.0 ± 0.7 (6)	26 ± 10 (6)	2 ± 7 (4)	4 ± 1 (4)	4.4 ± 0.3 (7)	178, 29-298

[a] –/– vs +/+: KWA, p = 0.015, g 1.2; –/– vs +/–: KWA, p = 0.002, g 1.5
[b] –/– vs +/+: KWA, p = 0.016, g 0.7; –/– vs +/–: KWA, p = 0.008, g 1.2
[c] –/– vs +/+: KWA, p = 0.006, g 2.1; –/– vs +/–: KWA, p = 2E-4, g 2.6
[d] –/– vs +/+: 2-way ANOVA, p <1E-9, g 1.3; –/– vs +/–: 2-way ANOVA, p < 1E-9, g 1.9

potential tuning (Ashmore, 1983; Fettiplace, 1987; Hudspeth and Lewis, 1988; Ramanathan and Fuchs, 2002). Larger R_{in} values made $K_V1.8^{-/-}$ type II HCs more prone to electrical resonance; **Figure 2.4C.1** shows a striking example. Median resonance quality (Q_e, sharpness of tuning) was greater in $K_V1.8^{-/-}$ (1.33, n=26) than $K_V1.8^{+/+}$ (0.66, n=23) or $K_V1.8^{+/-}$ (0.59, n=44) type II HCs.

$K_V1.8$ affected the time course of the initial peak in response to much larger current injections (**Fig. 2.4D-E**). Fast activation of g_A in control type II HCs rapidly repolarizes the membrane and then inactivates, allowing the constant input current to progressively depolarize the cell, producing a slow rebound (**Fig 2.4D.2**). This behavior has the potential to counter MET adaptation (Vollrath and Eatock, 2003).

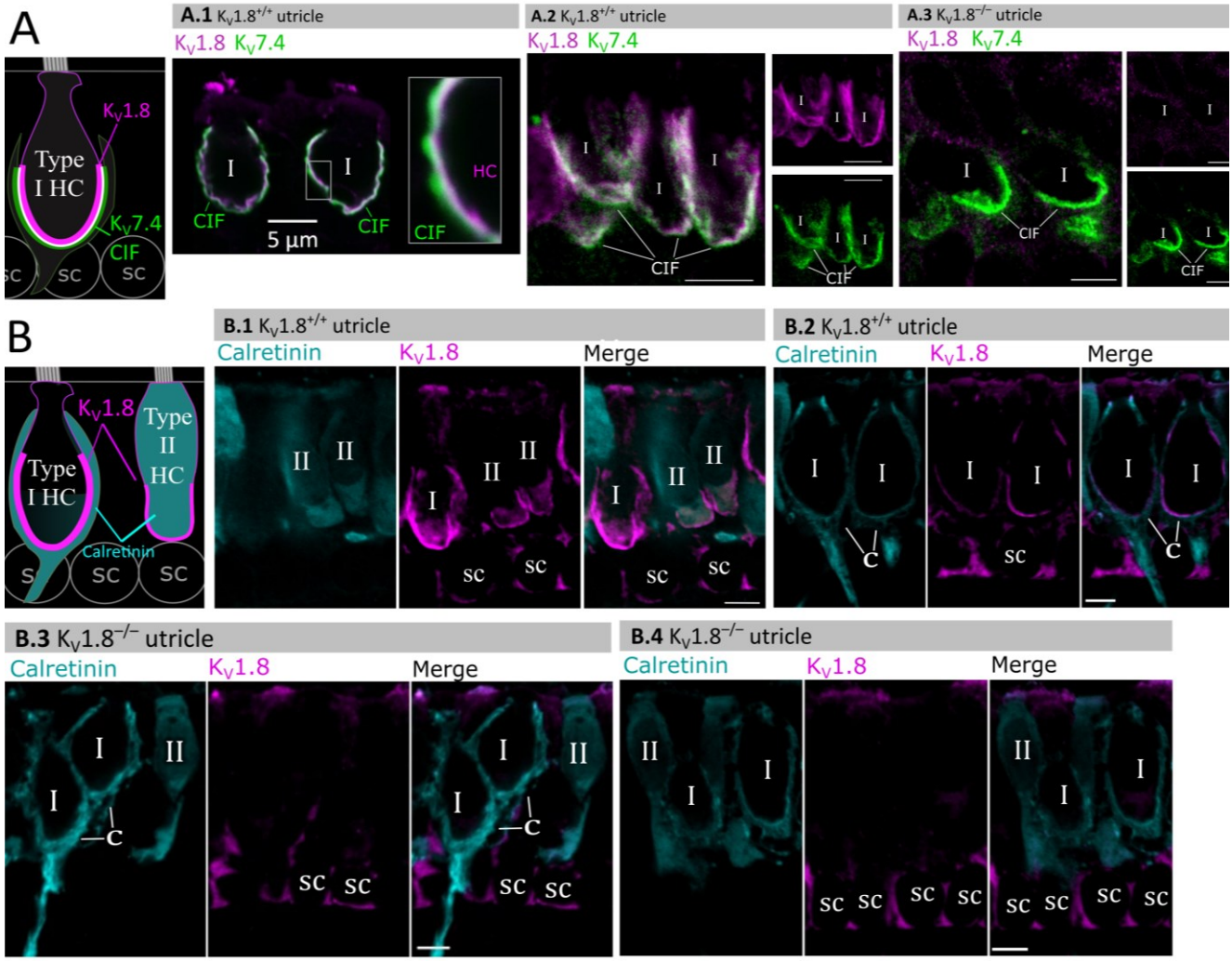

Figure 2.5. **Type I and type II HC basolateral membranes show specific immunoreactivity to Kv1.8 antibody (magenta).** Antibodies for $K_V7.4$ (A, green) and calretinin (B, cyan) were used as counterstains for calyx membrane (Kv7.4), type II HC cytoplasm (calretinin) and cytoplasm of striolar calyx-only afferents (calretinin). (**A**) *Left,* Cartoon showing $K_V7.4$ on the calyx inner face membrane (CIF) and $K_V1.8$ on the type I HC membrane. SC, supporting cell nuclei. *A.1-3*, Adult mouse utricle sections. $K_V7.4$ antibody labeled calyces on two $K_V1.8$-positive type I HCs (**A.1**), four $K_V1.8$-positive type I HCs (**A.2**), and two $K_V1.8$-negative type I HCs from a $K_V1.8^{-/-}$ mouse (**A.3**). (**B**) *Left,* Cartoon showing cytoplasmic calretinin stain in calyx-only striolar afferents and most type II HCs, and $K_V1.8$ on membranes of both HC types. In wildtype utricles, $K_V1.8$ immunolocalized to basolateral membranes of type I and II HCs (**B.1**). $K_V1.8$ immunolocalized to type I HCs in striola (**B.2**). Staining of supporting cell (SC) membranes by Kv1.8 antibody was non-specific, as it was present in $K_V1.8^{-/-}$ tissue (**B.3, B.4**).

$K_V1.8$ immunolocalized to basolateral membranes of both type I and II HCs

If $K_V1.8$ is a pore-forming subunit in the $K_V1.8$-dependent conductances $g_{K,L}$, g_A, and g_{DR}, it should localize to hair cell membranes. **Figure 2.5** compares $K_V1.8$ immunoreactivity in $K_V1.8^{+/+}$ and $K_V1.8^{-/-}$ utricles, showing specific immunoreactivity along the basolateral membranes of both hair

cell types in $K_V1.8^{+/+}$ utricles. To identify hair cell type and localize the hair cell membrane, we used antibodies against $K_V7.4$ (KCNQ4), an ion channel densely expressed in the calyceal "inner-face" membrane next to the synaptic cleft (Hurley et al., 2006; Lysakowski et al., 2011), producing a cup-like stain around type I HCs (**Fig. 2.5A**). $K_V1.8$ immunoreactivity was present in hair cell membrane apposing $K_V7.4$-stained calyx inner face in $K_V1.8^{+/+}$ utricles (**Fig. 2.5A.1, A.2**) and not in $K_V1.8^{-/-}$ utricles (**Fig. 2.5A.3**).

In other experiments, we used antibodies against calretinin (Calb2), a cytosolic calcium binding protein expressed by many type II HCs and also by striolar calyx-only afferents (Desai et al., 2005; Lysakowski et al., 2011) (**Fig. 2.5B**). A hair cell is type II if it is calretinin-positive (**Fig. 2.5B.1**) or if it lacks a $K_V7.4$-positive or calretinin-positive calyceal cup (**Fig. 2.5A.2, 5B.3**, rightmost cells). Hair cell identification was confirmed with established morphological indicators: for example, type II HCs tend to have basolateral processes (feet) (Pujol et al., 2014) and, in the extrastriola, more apical nuclei than type I HC.

Previously, Carlisle et al. (2012) reported $K_V1.8$-like immunoreactivity in many cell types in the inner ear. In contrast, Lee et al. (2013) found that gene expression reporters indicated expression only in hair cells and some supporting cells. Here, comparison of control and null tissue showed selective expression of HC membranes, and that some supporting cell staining is non-specific.

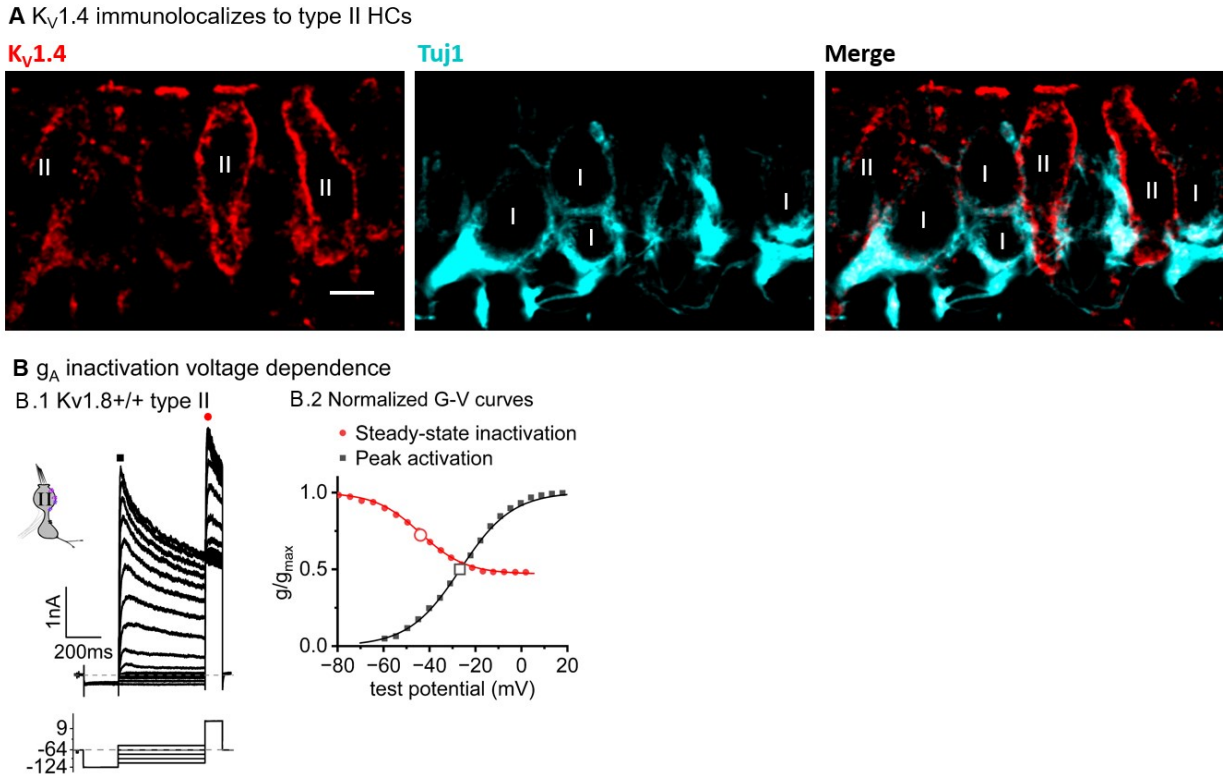

Figure 2.6. K_V1.4 subunits may contribute to g_A in extrastriolar type II HCs.
(**A**) Immunostaining of adult rat utricular epithelium with K_V1.4 antibody and TUJ-1, which labels afferent terminals, shows strong K_V1.4-like immunoreactivity on the membranes of 2 type II HCs. *Scale bar,* 5 µm. (**B**) Voltage dependence of g_A's steady-state inactivation (h_∞ curve) and peak activation are consistent with K_V1.4 heteromers. $K_V1.8^{+/+,+/-}$ type II HCs, n=11, P40-P210, median P94. (**B.1**) The inactivation voltage protocol, bottom. Tail current is a function of the voltage dependence of accumulated steady-state inactivation. 100 µM ZD7288 in bath prevented contamination by HCN current. (**B.2**) Overlapping normalized activation and inactivation ("h-infinity") G-V curves for data in B.1 at time points shown: peak currents (black squares, activation) and tail currents (red circles, inactivation). *Curves,* Boltzmann fits (Eq. 2.1). Average fit parameters for inactivation: V_{half}, –42 ±2 mV (n=11); S, 11 ± 1 mV. Activation: V_{half}, –23 ± 1 mV (n=11); S, 11.2 ± 0.4 mV.

K_V1.4 may also contribute to g_A

Results with the K_V1.8 knockout suggest that type II hair cells have an inactivating K_V1 conductance that includes K_V1.8 subunits. K_V1.8, like most K_V1 subunits, does not show fast inactivation as a heterologously expressed homomer (Lang et al., 2000; Ranjan et al., 2019; Dierich et al., 2020), nor do the K_V1.8-dependent channels in type I HCs, as we show, and cochlear inner hair cells (Dierich et al., 2020). K_V1 subunits without intrinsic inactivation can produce rapidly inactivating currents by associating with $K_V\beta$1 (KCNB1) or $K_V\beta$3 subunits. $K_V\beta$1 is present

in type II HCs alongside $K_V\beta2$ (McInturff et al., 2018; Jan et al., 2021; Orvis et al., 2021), which does not confer rapid inactivation (Dwenger et al., 2022).

An alternative possibility is that in type II HCs, $K_V1.8$ subunits heteromultimerize with $K_V1.4$ subunits – the only K_V1 subunits which, when expressed as a homomer, have complete N-type (fast) inactivation (Stühmer et al., 1989). Multiple observations support this possibility. $K_V1.4$ has been linked to g_A in pigeon type II HCs (Correia et al., 2008) and is the second-most abundant K_V1 transcript in mammalian vestibular HCs, after $K_V1.8$ (Scheffer et al., 2015). $K_V1.4$ is expressed in type II HCs but not type I HCs (McInturff et al., 2018; Orvis et al., 2021), and is not found in striolar HCs (Jan et al., 2021; Orvis et al., 2021), where even in type II HCs, inactivation is slower and less extensive (**Fig. 2.3A**).

In $K_V1.8^{+/+,+/-}$ type II HCs, the time course (**Fig. 2.3A**, $\tau_{Fast,Inac}$ of ~30 ms +30 mV) and voltage dependence of inactivation of g_A (V_{half} –41 mV, **Fig. 2.6B.2**), are consistent with heterologously expressed heteromers of $K_V1.4$ with $K_V1.x$ and/or $K_V\beta1$ (Imbrici et al., 2006; Al-Sabi et al., 2011). In further support, we observed $K_V1.4$-like immunoreactivity along the basolateral membranes of extrastriolar type II HCs in rat utricles (**Fig. 2.6A**).

K_V7 channels contribute a small delayed rectifier in type I and type II hair cells

In $K_V1.8^{-/-}$ HCs, absence of $I_{K,L}$ and I_A revealed smaller delayed rectifier K^+ currents that, unlike $I_{K,L}$, activated positive to resting potential and, unlike I_A, lacked fast inactivation. Candidate channels include members of the K_V7 (KCNQ, M-current) family, which have been identified previously in rodent vestibular HCs (Kharkovets et al., 2000; Rennie et al., 2001; Hurley et al., 2006; Scheffer et al., 2015).

We test for K_V7 contributions in $K_V1.8^{-/-}$ type I HCs, $K_V1.8^{-/-}$ type II HCs, and $K_V1.8^{+/+,+/-}$ type II HCs of multiple ages by applying XE991 at 10 μM (**Fig. 2.7A**), a dose selective for K_V7 channels (Brown et al., 2002) and close to the IC_{50} (Alexander et al., 2019). In $K_V1.8^{-/-}$ HCs of both types, 10 μM XE991 blocked about half of the residual K_V conductance (**Fig. 2.7B.1**), consistent with K_V7 channels conducting most or all of the non-$K_V1.8$ delayed rectifier current. In all tested HCs (P8-355, median P224), the XE991-sensitive conductance did not inactivate substantially within 200 ms at any voltage, consistent with $K_V7.2$, 7.3, 7.4, and 7.5 currents (Wang, 1998; Kubisch et al., 1999; Schroeder et al., 2000; Jensen et al., 2007; Xu et al., 2007). We refer to this component as $g_{DR}(K_v7)$. The voltage dependence and Gmax density (G_{max}/C_m) of $g_{DR}(K_v7)$ were comparable across HC types and genotypes (**Fig. 2.7B.2-4**). Although $K_V7.4$ was not detectable in HCs during immunostaining (**Fig. 2.5**), $K_V7.4$ has been shown in type I HCs with immunogold labeling (Kharkovets et al., 2000; Hurley et al., 2006).

These results are consistent with similar K_V7 channels contributing a relatively small delayed rectifier in both HC types. In addition, the similarity of XE991-sensitive currents of $K_V1.8^{+/+}$ and $K_V1.8^{-/-}$ type II HCs indicates that knocking out $K_V1.8$ did not cause general effects on ion channel expression. We did not test XE991 on $K_V1.8^{+/+,+/-}$ type I HCs because $g_{K,L}$ runs down in ruptured patch recordings (Rüsch and Eatock, 1996a; Chen and Eatock, 2000; Hurley et al., 2006), which could contaminate the XE991-sensitive conductance obtained by subtraction.

In one striolar $K_V1.8^{-/-}$ type I HC, XE991 also blocked a small conductance that activated negative to rest (**Suppl. Fig. S2.5A-B**). This conductance (V_{half} ~= –100 mV, **Suppl. Fig. S2.5C**) was detected only in $K_V1.8^{-/-}$ type I HCs from the striola (5/23 vs. 0/45 extrastriolar). The V_{half} and $\tau_{deactivation}$ at –124 mV were similar to values reported for $K_V7.4$ channels in cochlear HCs (Wong et al., 2004; Dierich et al., 2020). This very negatively activating K_V7 conductance

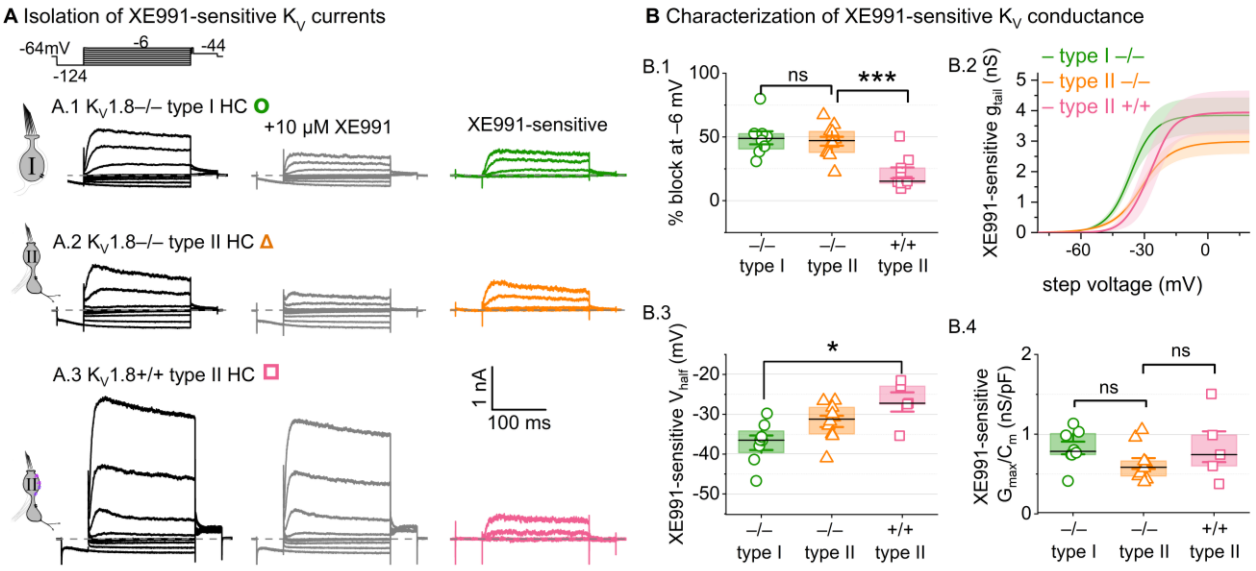

Figure 2.7. A K_V7-selective blocker, XE991, reduced residual delayed rectifier currents in $K_V1.8^{-/-}$ type I and II HCs. (A) XE991 (10 µM) partly blocked similar delayed rectifier currents in type I and type II $K_V1.8^{-/-}$ HCs and a type II $K_V1.8^{+/+}$ HC. **(B)** Properties of XE991-sensitive conductance, $g_{DR}(K_V7)$. (**B.1**) % Block of steady-state current. (**B.2**) tail G-V curves for $K_V1.8^{-/-}$ type I HCs (n=8), $K_V1.8^{-/-}$ type II HCs (9), and $K_V1.8^{+/+}$ type II HCs (5); mean ± SEM. (**B.3**) V_{half} was less negative in $K_V1.8^{+/+}$ type II than $K_V1.8^{-/-}$ type I HC (p = 0.01, KWA). (**B.4**) Conductance density was similar in all groups (ANOVA, non-significant at 40% power (*left*), 20% power (*right*).

coexisted with the larger less negatively activating K_V7 conductance (**Suppl. Fig. S2.5C**) and was too small (<0.5 nS/pF) to contribute significantly to $g_{K,L}$ (~10-100 nS/pF, **Fig. 1D**).

Other channels

While our data are consistent with $K_V1.8$- and K_V7- containing channels carrying most of the outward-rectifying current in mouse utricular hair cells, there is evidence in other preparations for additional channels, including K_V11 (KCNH, Erg) channels in rat utricular type I hair cells (Hurley et al., 2006) and BK (KCNMA1) channels in rat utricle and rat and turtle semicircular canal hair cells (Schweizer et al., 2009; Contini et al., 2020).

BK is expressed in mouse utricular hair cells (McInturff et al., 2018; Jan et al., 2021; Orvis et al., 2021). However, Ca^{2+}-dependent currents have not been observed in mouse utricular HCs, and

we found little to no effect of the BK-channel blocker iberiotoxin at a dose (100 nM) well beyond the IC_{50}: percent blocked at –30 mV was 2 ± 6% (3 $K_V1.8^{-/-}$ type I HCs); 1 ± 5% (5 $K_V1.8^{+/+,+/-}$ type II HCs); 7% and 14% (2 $K_V1.8^{-/-}$ type II HCs). We also did not see N-shaped I-V curves typical of many Ca^{2+}-dependent K^+ currents. In our ruptured-patch recordings, Ca^{2+}-dependent BK currents and erg channels may have been eliminated by wash-out of the hair cells' small Ca_V currents (Bao et al., 2003) or cytoplasmic second messengers (Hurley et al., 2006).

To check whether the constitutive $K_V1.8$ knockout has strong non-specific effects on channel trafficking, we examined the summed HCN and inward rectifier currents (I_H and I_{Kir}) at –124 mV, and found them similar across genotypes (**Suppl. Fig. S2.6**). In the process, we noted zonal differences in I_H and I_{Kir} that have not been reported in hair cells. In type I HCs from both control and null utricles, I_H and I_{Kir} were less prevalent in striola than extrastriola, and, when present, the combined inward current was smaller (**Suppl. Fig. S2.6B**).

We occasionally noted voltage-gated sodium current (I_{NaV}) in control and Kv1.8-null type II HCs up to P300, evident as a transient inward current as voltage was stepped from –124 mV to the tail potential of –44 mV (**Suppl. Fig S2.7A**). Its transient nature (it rapidly returned to 0 pA) indicated that it flowed through Na_V channels, not Ca_V channels, which are relatively sustained in HCs (Bao et al., 2003; Manca et al., 2021). Na_V currents are widely expressed in developing utricular hair cells (Géléoc et al., 2004) in two varieties with distinct voltage dependence; after P10, only the more negatively activating version, "$I_{Na,l}$" (likely $Na_V1.5$, which is more highly expressed in striolar HCs), is observed (Wooltorton et al., 2007). In **Supplementary Figure S2.7**, we examined whether I_{NaV} correlated with age (P5-P370), zone, and genotype. I_{NaV} was equally likely in all genotypes but was much more likely in striolar type II HCs (~70%) than extrastriolar

type II HCs (~10 %) (**Suppl. Fig. S2.7C.1**). The voltage midpoints of activation and inactivation (**Suppl. Fig S2.7**) matched those of the $I_{Na,1}$ subtype.

Such high I_{NaV} incidence rates in hair cells from adult vestibular epithelia haven't been reported before, but this may reflect neglect of striola in electrophysiology. Denervation during experiments may have also amplified observations of I_{NaV}. In our *ex vivo* semi-intact prep, the afferent nerves were severed close to the base of the utricle during dissection, which can lead to degradation and retraction of terminals from HCs. Others have shown that such denervation can lead to rapid Na_V unmasking (Brugeaud et al., 2006, 2007). Striolar afferents are often more susceptible to degradation, resulting in denervated striolar type II HCs that express I_{NaV}. $I_{Na,1}$ can also indicate recently regenerated type II HCs (González-Garrido et al., 2021), but zonal control over mammalian regeneration of hair cells is not well understood.

2.4 Discussion

We have shown that constitutive knockout of $K_V1.8$ eliminated $g_{K,L}$ in type I HCs, and g_A and much of g_{DR} in type II HCs. $K_V1.8$ immunolocalized specifically to the basolateral membranes of type I and II HCs. We conclude that $K_V1.8$ is a pore-forming subunit of $g_{K,L}$, g_A, and part of g_{DR} [$g_{DR}(K_V1.8)$]. We suggest that fast inactivation of g_A may arise from heteromultimerization of non-inactivating $K_V1.8$ subunits and inactivating $K_V1.4$ subunits. Finally, we showed that a substantial component of the residual delayed rectifier current in both type I and type II HCs comprises K_V7 channels.

$K_V1.8$ is expressed in hair cells from mammalian cochlea (Dierich et al., 2020), avian utricle (Scheibinger et al., 2022), and zebrafish (Erickson and Nicolson, 2015). Our work suggests that in

anamniotes, which lack type I cells and $g_{K,L}$, $K_V1.8$ contributes to g_A and g_{DR}, which are widespread in vertebrate HCs (reviewed in Meredith and Rennie, 2016). $K_V1.8$ expression has not been detected in rodent brain but is reported in the pacemaker nucleus of weakly electric fish (Smith et al., 2018).

$K_V1.8$ subunits may form homomultimers to produce $g_{K,L}$ in type I hair cells

Recent single-cell expression studies on mouse utricles (McInturff et al., 2018; Jan et al., 2021; Orvis et al., 2021) have detected just one K_V1 subunit, $K_V1.8$, in mouse type I HCs. Given that $K_V1.8$ can only form multimers with K_V1 family members, and given that $g_{K,L}$ channels are present at very high density (~150 per mm^2 in rat type I, Chen and Eatock, 2000), it stands to reason that most or all of the channels are $K_V1.8$ homomers. Other evidence is consistent with this proposal. $g_{K,L}$ (Rüsch and Eatock, 1996a) and heterologously expressed $K_V1.8$ homomers in oocytes (Lang et al., 2000) are non-inactivating and blocked by millimolar Ba^{2+} and 4-aminopyridine and >10 mM TEA. Unlike channels with $K_V1.1$, $K_V1.2$, and $K_V1.6$ subunits, $g_{K,L}$ is not sensitive to 10 nM α-dendrotoxin (Rüsch and Eatock, 1996a). $g_{K,L}$ and heterologously expressed $K_V1.8$ channels have similar single-channel conductances (~20 pS for $g_{K,L}$ at positive potentials, Chen and Eatock, 2000; 11 pS in oocytes, Lang et al., 2000). $g_{K,L}$ is inhibited—or positively voltage-shifted—by cGMP (Behrend et al., 1997; Chen and Eatock, 2000), presumably via the C-terminal cyclic nucleotide binding domain of $K_V1.8$.

A major novel property of $g_{K,L}$ is that it activates 30-60 mV negative to type II $K_V1.8$ conductances and most other low-voltage-activated K_V channels (Ranjan et al., 2019). The very negative activation range is a striking difference between $g_{K,L}$ and known homomeric $K_V1.8$ channels. Heterologously expressed homomeric $K_V1.8$ channels have an activation V_{half} of –10 to

0 mV (*X. laevis* oocytes, Lang et al., 2000; CHO cells, Dierich et al., 2020). In cochlear inner HCs, currents attributed to $K_V1.8$ (by subtraction of other candidates) have a near-zero activation V_{half} (–4 mV, Dierich et al., 2020).

Possible factors in the unusually negative voltage dependence of $g_{K,L}$ include:

1) elevation of extracellular K^+ by the enveloping calyceal terminal, unique to type I HCs (Lim et al., 2011; Contini et al., 2012; Spaiardi et al., 2020; Govindaraju et al., 2023). High K^+ increases conductance though $g_{K,L}$ channels (Contini et al., 2020), perhaps through K^+-mediated relief of C-type inactivation (López-Barneo et al., 1993; Baukrowitz and Yellen, 1995). We note, however, that $g_{K,L}$ is open at rest even in neonatal mouse utricles cultured without innervation (Rüsch et al., 1998) and persists in dissociated type I HCs (Chen and Eatock, 2000; Hurley et al., 2006).

2) The high density of $g_{K,L}$ (~50 nS/pF in striolar $K_V1.8^{+/+}$ HCs) implies close packing of channels, possibly represented by particles (12-14 nm) seen in freeze-fracture electron microscopy of the type I HC membrane (Gulley and Bagger-Sjöbäck, 1979; Sousa et al., 2009). Such close channel packing might hyperpolarize *in situ* voltage dependence of $g_{K,L}$, as proposed for $K_V7.4$ channels in outer hair cells (Perez-Flores et al., 2020). Type I HC-specific partners that may facilitate this close packing include ADAM11 (McInturff et al., 2018), which clusters presynaptic $K_V1.1$ and $K_V1.2$ to enable ephaptic coupling at a cerebellar synapse (Kole et al., 2015).

3) Modulation by accessory subunits. Type I HCs express $K_V\beta1$ (McInturff et al., 2018; Orvis et al., 2021), an accessory subunit that can confer fast inactivation and hyperpolarize activation V_{half} by ~10 mV. $K_V\beta1$ might interact with $K_V1.8$ to shift voltage dependence negatively. Arguments against this possibility include that $g_{K,L}$ lacks fast inactivation (Rüsch and Eatock, 1996a; Hurley et al., 2006; Spaiardi et al., 2017) and that cochlear inner hair cells co-express $K_V1.8$

and $K_V\beta1$ (Liu et al., 2018) but their $K_V1.8$ conductance has a near-0 V_{half} (Dierich et al., 2020).

$K_V1.8$ subunits may heteromerize with variable numbers of inactivating $K_V1.4$ subunits to produce g_A and $K_V1.8$-dependent g_{DR} in type II HCs

The $K_V1.8$-dependent conductances of type II HCs vary in their fast and slow inactivation. In not showing fast inactivation (Lang et al., 2000; Ranjan et al., 2019; Dierich et al., 2020), heterologously expressed $K_V1.8$ subunits resemble most other K_V1 family subunits, with the exception of $K_V1.4$ (for comprehensive review, see Ranjan et al., 2019). $K_V1.4$ is a good candidate to provide fast inactivation based on immunolocalization and voltage dependence (Figs. 2.4, 2.6). We suggest that g_A and $g_{DR}(K_V1.8)$ are $K_V1.8$-containing channels that may include a variable number of $K_V1.4$ subunits and $K_V\beta2$ and $K_V\beta1$ accessory subunits.

$K_V1.4$-$K_V1.8$ heteromeric assembly could account for several related observations. The faster $\tau_{Inact,Fast}$ in $K_V1.8^{+/-}$ relative to $K_V1.8^{+/+}$ type II HCs (**Fig. 2.3A.3, Suppl. Fig. S2.2A.1**) could reflect an increased ratio of $K_V1.4$ to $K_V1.8$ subunits and therefore more N-terminal inactivation domains per heteromeric channel. Zonal variation in the extent and speed of N-type inactivation (Fig. 2.3A) might arise from differential expression of $K_V1.4$. The small fast-inactivating conductance in ~20% of extrastriolar $K_V1.8^{-/-}$ type II HCs (**Suppl. Fig. 2.4)** might flow through $K_V1.4$ homomers.

Fast inactivation may also receive contribution from $K_V\beta$ subunits. $K_V\beta1$ is expressed in type II HCs (McInturff et al., 2018; Jan et al., 2021; Orvis et al., 2021), and, together with $K_V1.4$, has been linked to g_A in pigeon vestibular HCs (Correia et al., 2008). $K_V\beta2$, also expressed in type II HCs (McInturff et al., 2018; Orvis et al., 2021), does not confer fast inactivation.

It is not likely that g_A and $g_{DR}(K_V1.8)$ are different kinetic components of current through homogeneous incompletely inactivating K_V channels. As discussed, g_A may include heteromers of $K_V1.8$ and other subunits lending rapid inactivation. $g_{DR}(K_V1.8)$ may comprise homomeric $K_V1.8$ channels, which do not have N-type inactivation.

$K_V1.8$ relevance for vestibular function

In both type I and type II utricular HCs, $K_V1.8$-dependent channels strongly shape receptor potentials in ways that promote temporal fidelity rather than electrical tuning (Lewis, 1988), consistent with the utricle's role in driving reflexes that compensate for head motions as they occur. This effect is especially pronounced for type I HCs, where the current-step evoked voltage response reproduces the input with great speed and linearity (**Fig. 2.2**).

$g_{K,L}$ dominates passive membrane properties in mature $K_V1.8^{+/+,+/-}$ type I HCs such that $K_V1.8^{-/-}$ type I HCs are expected to have receptor potentials with higher amplitudes but lower low-pass corner frequencies, closer to those of type II HCs and immature HCs of all types (Correia et al., 1996; Rüsch and Eatock, 1996a; Songer and Eatock, 2013). In $K_V1.8^{-/-}$ epithelia, we expect the lack of a large basolateral conductance open at rest to reduce the speed and gain of non-quantal transmission, which depends on K^+ ion efflux from the type I HC to change electrical and K^+ potentials in the synaptic cleft (Govindaraju et al., 2023). In hair cells, K^+ enters the mechanosensitive channels of the hair bundle from the K^+-rich apical endolymph and exits through basolateral potassium conductances into the more conventional low-K+ perilymph. For the type I-calyx synapse, having in the hair cell a large, non-inactivating K^+ conductance open across the physiological range of potentials avoids channel gating time and allows for instantaneous changes in current into the cleft and fast afferent signaling (Pastras et al., 2023).

In contrast, mature type II HCs face smaller synaptic contacts and have $K_V1.8$-dependent currents that are not substantially activated at resting potential. They do affect the time course and gain of type II HC responses to input currents, speeding up depolarizing transients, producing a repolarizing rebound during the step, and reducing resonance.

Type I and II vestibular hair cells are closely related, such that adult type II HCs acquire type I-like properties upon deletion of the transcription factor Sox2 (Stone et al., 2021). In normal development of the two cell types, the Kcna10 gene generates different ion channels, presenting a natural experiment in functional differentiation of sensory receptor cells.

2.5 Materials and methods

Preparation

All procedures for handling animals followed the NIH Guide for the Care and Use of Laboratory Animals and were approved by the Institutional Animal Care and Use Committees of the University of Chicago and the University of Illinois Chicago. Most mice belonged to a transgenic line with a knockout allele of *Kcna10* (referred to here as $K_V1.8^{-/-}$). Our breeding colony was established with a generous gift of such animals from Sherry M. Jones and Thomas Friedman. These animals are described in their paper (Lee et al., 2013). Briefly, the Texas A&M Institute for Genomic Medicine generated the line on a C57BL/6;129SvEv mixed background by replacing Exon 3 of the *Kcna10* gene with an IRES-bGeo/Purocassette. Mice in our colony were raised on a 12:12h light-dark cycle with access to food and water *ad libitum*.

Semi-intact utricles were prepared from ~150 male and ~120 female mice, postnatal days (P) 5-375, for same-day recording. Hair cell K_V channel data were pooled across sexes as most results did not appear to differ by sex; an exception was that $g_{K,L}$ had a more negative V_{half} in males

(**Suppl. Table S2.1**), an effect not clearly related to age, copy number, or other properties of the activation curve.

Preparation, stimulation, and recording methods followed our previously described methods for the mouse utricle (Vollrath and Eatock, 2003). Mice were anesthetized through isoflurane inhalation. After decapitation, each hemisphere was bathed in ice-cold, oxygenated Liebowitz-15 (L15) media. The temporal bone was removed, the labyrinth was cut to isolate the utricle, and the nerve was cut close to the utricle. The utricle was treated with proteinase XXIV (100 mg/mL, ~10 mins, 22ºC) to facilitate removal of the otoconia and attached gel layer and mounted beneath two glass rods affixed at one end to a coverslip.

Electrophysiology

We used the HEKA Multiclamp EPC10 with Patchmaster acquisition software, filtered by the integrated HEKA filters: a 6-pole Bessel filter at 10 kHz and a second 4-pole Bessel filter at 5 kHz, and sampled at 10-100 kHz. Recording electrodes were pulled (PC-100, Narishige) from soda lime glass (King's Precision Glass R-6) wrapped in paraffin to reduce pipette capacitance. Internal solution contained (in mM) 135 KCl, 0.5 $MgCl_2$, 3 MgATP, 5 HEPES, 5 EGTA, 0.1 $CaCl_2$, 0.1 Na-cAMP, 0.1 LiGTP, 5 $Na_2CreatinePO_4$ adjusted to pH 7.25 and ~280 mmol/kg by adding ~30 mM KOH. External solution was Liebowitz-15 media supplemented with 10 mM HEPES (pH 7.40, 310 ± 10 mmol/kg). Recording temperature was 22-25ºC. Pipette capacitance and membrane capacitance transients were subtracted during recordings with Patchmaster software. Series resistance (8-12 MΩ) was measured after rupture and compensated 60-80% with the amplifier, to final values of ~2 MΩ. Potentials are corrected for remaining (uncompensated) series resistance and liquid junction potential of ~+4 mV, calculated with LJPCalc software (Marino et al., 2014).

Type I HCs with $g_{K,L}$ were transiently hyperpolarized to –90 mV to close $g_{K,L}$ enough to increase R_{input} above 100 MΩ, as needed to estimate series resistance and cell capacitance. The average resting potential, V_{rest}, was –87 mV ± 1 (41), similar to the calculated E_K of –86.1 mV, which is not surprising given the large K^+ conductance of these cells (**Fig. 2.1**). V_{rest} is likely more positive *in vivo*, where lower endolymphatic Ca^{2+} increases standing inward current through MET channels.

Voltage protocols to characterize K_V currents differed slightly for type I and II HCs. In standard protocols, the cell is held at a voltage near resting potential (–74 mV in type I and –64 mV in type II), then jumped to –124 mV for 200 ms in type I HCs in order to fully deactivate $g_{K,L}$ and 50 ms in type II HCs in order to remove baseline inactivation of g_A. The subsequent iterated step depolarizations lasted 500 ms in type I HCs because $g_{K,L}$ activates slowly (Wong et al., 2004) and 200 ms in type II HCs, where K_V conductances activate faster. The 50-ms tail voltage was near the reversal potential of HCN channels (–44 mV in mouse utricular hair cells, Rüsch et al., 1998) to avoid HCN current contamination.

G-V (activation) parameters for control type I cells may be expected to vary across experiments on semi-intact (as here), organotypically cultured and denervated (Rüsch et al.,1998), or dissociated-cell preparations, reflecting variation in retention of the calyx (Discussion) and voltage step durations (Wong et al., 2004) which elevate K^+ concentration around the hair cell. Nevertheless, the values we obtained for type I and type II HCs resemble values recorded elsewhere, including experiments in which extra care was taken to avoid extracellular K^+ accumulation (Spaiardi et al., 2017, 2020). The effects of K^+ accumulation on $g_{K,L}$'s steady-state activation curves are small because the operating range is centered on E_K and can be characterized with relatively small currents (**Fig. 2.1A**).

Pharmacology

Drug-containing solutions were locally with BASI Bee Hive syringes at a final flow rate of 20 µL/min and a dead time of ~30 s. Global bath perfusion was paused during drug perfusion and recording, and only one cell was used per utricle. Aliquots of test agents in solution were prepared, stored at –20°C, and thawed and added to external solution on the recording day (see Key Resources Table).

Analysis

Data analysis was performed with software from OriginLab (Northampton, MA) and custom MATLAB scripts using MATLAB fitting algorithms.

Fitting voltage dependence and time course of conductances

G-V curves. Current was converted to conductance (G) by dividing by driving force ($V - E_K$; E_K calculated from solutions). For type I HCs, tail G-V curves were generated from current 1 ms after the end of the iterated voltage test step. For type II HCs, peak G-V curves were generated from peak current during the step and steady-state G-V curves were generated from current 1 ms before the end of a 200 ms step. Sigmoidal voltage dependence of G-V curves was fit with the first-order Boltzmann equation (Eq. 2.1).

$$G(V) = G_{min} + \frac{G_{max}}{1 + e^{\frac{V_{half} - V}{S}}} \qquad (2.1)$$

V_{half} is the midpoint and S is the slope factor, inversely related to curve steepness near activation threshold.

Activation time course of type II HCs. For type II HCs lacking fast inactivation, outward current activation was fit with Eq. 2.2.

$$I(t) = I_{SS} * \left(1 - e^{-\frac{t}{\tau_w}}\right)^n + I_0 \qquad (2.2)$$

I_{SS} is steady-state current, τ_w is activation time constant, n is the state factor related to the number of closed states (typically constrained to 3), and I_o is baseline current.

To measure activation and inactivation time course of g_A, we used Eq. 2.3 to fit outward K^+ currents evoked by steps from –125 mV to above –50 mV (Rothman and Manis, 2003b).

$$I(t) = I_{max} * \left(1 - e^{-\frac{t}{\tau_w}}\right)^n * (1 - Z * (f * \left(1 - e^{-\frac{t}{\tau_{zf}}}\right) + (1 - f) * \left(1 - e^{-\frac{t}{\tau_{zs}}}\right)) + I_0 \qquad (2.3)$$

Z is total steady-state inactivation ($0 \leq Z < 1$ means incomplete inactivation, which allows the equation to fit non-inactivating delayed rectifier currents), f is the fraction of fast inactivation relative to total inactivation, I_{max} is maximal current, τ_{zf} and τ_{zs} are the fast and slow inactivation time constants. We chose to compare fit parameters at 30 ± 2 mV (91), where fast and slow inactivation were consistently separable and g_A was maximized. In most $K_V1.8^{-/-}$ and some striolar $K_V1.8^{+/+,+/-}$ cells, where fast inactivation was absent and adjusted R^2 did not improve on a single-exponential fit by >0.01, we constrained f in Eq. 2.3 to 0 to avoid overfitting.

For *Peak* G-V relations, peak conductance was taken from fitted curves (Eqs. 2.2 and 2.3). To construct '*Steady-state'* G-V relations, we used current at 200 ms (6 ± 1 % (94) greater than steady-state estimated from fits to Eq. 2.3 (Fig. 2.3C-D)).

Percent inactivation was calculated at 30 mV with Eq. 2.4 :

$$\%\, Inactivation = (I_{Peak} - I_{SS})/I_{Peak} \qquad (2.4)$$

I_{Peak} is maximal current, and I_{SS} is current at the end of a 200 ms voltage step.

The electrical resonance of type II HCs was quantified by fitting voltage responses to current injection steps (Songer and Eatock, 2013). We fit Eq. 2.5, a damped sinusoid, to the voltage trace from half-maximum of the initial depolarizing peak until the end of the current step.

$$V(t) = V_{ss} + V_p * e^{-\frac{t}{\tau_e}} * \sin(2\pi f_e - \theta) \quad (2.5)$$

V_{SS} is steady-state voltage, V_p is the voltage of the peak response, τ_e is the decay time constant, f_e is the fundamental frequency, and θ is the phase angle shift.

Quality factor, Q_e, was calculated with Eq. 2.6 (Crawford and Fettiplace, 1981).

$$Q_e = [(\pi f_e \tau_e)^2 + 0.25]^{1/2} \quad (2.6)$$

Statistics

We give means ± SEM for normally-distributed data, and otherwise, median and range. Data normality was assessed with the Shapiro-Wilk test for n<50 and the Kolmogorov-Smirnov test for n>50. To assess homogeneity of variance we used Levene's test. With homogeneous variance, we used two-way ANOVA for genotype and zone with the posthoc Tukey's test. When variance was non-homogeneous, we used one-way Welch ANOVA with the posthoc Games-Howell test. For data that were not normally distributed, we used the non-parametric one-way Kruskal-Wallis ANOVA (KWA) with posthoc Dunn's test. Effect size is Hedge's g (g). For age dependence, we used partial correlation coefficients controlling for genotype and zone. Statistical groups may have different median ages, but all have overlapping age ranges. In figures, asterisks represent p-value ranges as follows: *, p<0.05; **, p<0.01; ***, p<0.001; ****, p<0.0001.

Immunohistochemistry

Mice were anesthetized with Nembutal (80 mg/kg), then perfused transcardially with 40mL of physiological saline containing heparin (400 IU), followed by 2 mL/g body weight fixative (4%

paraformaldehyde, 1% picric acid, and 5% sucrose in 0.1 M phosphate buffer at pH 7.4, sometimes with 1% acrolein). Vestibular epithelia were dissected in phosphate buffer, and tissues were cryoprotected in 30% sucrose-phosphate buffer overnight at 4ºC. Otoconia were dissolved with Cal-Ex (Fisher Scientific) for 10 min. Frozen sections (35 μm) were cut with a sliding microtome. Immunohistochemistry was performed on free-floating sections. Tissues were first permeabilized with 4% Triton X-100 in PBS for 1 h at room temperature, then incubated with 0.5% Triton X-100 in a blocking solution of 0.5% fish gelatin and 1% BSA for 1 h at room temperature. Sections were incubated with 2-3 primary antibodies for 72 h at 4ºC and with 2-3 secondary antibodies. Sections were rinsed with PBS between and after incubations and mounted on slides in Mowiol (Calbiochem).

Table 2.6. Key Resources Table

Antibody	Source	Catalog Number	Lot Number	Dilution
Rabbit anti-K_V1.8	Alomone	APC-157	0102	1:200 or 1:400
Mouse anti-K_V1.4	NeuroMab	P15385	5HK-05	1:400
Mouse IGg2a-conjugated anti-Tuj1	Covance	MMS-435P	B205808	1:300
Goat anti-calretinin	Millipore	AB1550	9669	1:600
Mouse IgG1-conjugated anti-K_V7.4	NeuroMab	2HK-65		1:200
Donkey anti-Rabbit Secondary Antibody, Alexa Fluor 594	Invitrogen	A21207	8652	1:200
Donkey anti-Goat 488 nm	Invitrogen	A21125	1920483	1:200
Goat anti-Mouse IgG1 594	Invitrogen	A11055	1869589	1:200
Chemicals and Peptides	Source	Catalog Number	Diluent	
Iberiotoxin	Alomone	STI-400	Water	
XE991 dihydrochloride	Sigma	X2254	Water	
ZD7288	Tocris	APN18035-2	Water	
Bovine serum albumin	Fisher	BP671	water	

Data Availability

Data used in this study are available on Dryad (https://doi.org/10.5061/dryad.37pvmcvrw).

Acknowledgements

This study was supported by NIH grant R01 DC012347 to RAE and AL and an NSF Graduate Research Fellowship to HRM. We thank Drs. Thomas Friedman and Sherri Jones for the generous gift of the $K_V1.8^{-/-}$ mouse line, and Drs. Zheng-Yi Chen and Deborah I. Scheffer for bringing the expression of this subunit in mouse vestibular hair cells to our attention.

We acknowledge Dr. Vicente Lumbreras for insights from his prior experiments on g_A in mouse utricular hair cells, and thank him for helpful further discussions.

We acknowledge Steven D. Price for his help with immunocytochemistry. Imaging was performed at the University of Chicago Integrated Light Microscopy Core RRID: SCR_019197.

We thank Drs. Rebecca Lim and Ebenezer Yamoah for their critical feedback on the manuscript, and Drs. Rob Raphael and Aravind Chenrayan Govindaraju for feedback and many helpful discussions. We thank Drs. Joe Burns, Gabi Pregernig, and Lars Becker (Decibel Therapeutics, Inc.) for helpful discussions.

Author Contributions

HRM designed and performed experiments, analyzed data, and wrote the paper; RAE helped design experiments, analyze data, and write the paper; AL performed immunohistochemistry experiments and reviewed and edited the manuscript.

CHAPTER 3

KNOCKOUT OF $K_V1.8$ SUBUNITS IMPAIRS VESTIBULAR HAIR CELL RECEPTOR POTENTIALS, SYNAPTIC TRANSMISSION, AND BALANCE

3.1 ABSTRACT

Epithelial hair cells underlie detection of head motion, gravity, and sound in vertebrates, and underwent drastic specialization in tetrapods during the transition to life on land. As tetrapods gained more mobile necks and experienced higher frequency motion in the air, signal transmission delays may have been reduced in the newly developed type I vestibular hair cell through its large, low-voltage-activated K^+ conductance ($g_{K,L}$) and postsynaptic calyx, two unique features absent in the more ancient type II hair cells. We recently reported that $K_V1.8$ is a necessary subunit in $g_{K,L}$ and also in the A-type K^+ conductance and most of the delayed rectifier K^+ conductance in type II hair cells.

In Chapter 3, we assessed the contribution of these $K_V1.8$ conductances to three levels of vestibular function: hair cell receptor potentials, synaptic transmission, and vestibulomotor behaviors. In both hair cell types, $K_V1.8$ conferred a low input resistance that was necessary for accelerating, dampening, and reducing receptor potentials. Without $K_V1.8$, lowpass corner frequencies (f_{LP}) of receptor potentials were ~20 Hz, much lower than in controls: ~370 Hz (type I hair cell) and ~70 Hz (type II hair cell). In $K_V1.8^{-/-}$ calyces, signals transmitted via non-quantal transmission had greater phase and smaller responses at higher frequencies; f_{LP} dropped from 14 Hz in controls to 7 Hz in $K_V1.8^{-/-}$ calyces. Such lower f_{LP} would correspond to a deteriorated detection of high-frequency (10-100 Hz) head motions. $K_V1.8^{-/-}$ mice had impaired performance on challenging vestibulomotor tasks, such as crossing a narrow beam and rearing on hindlegs, but

not basic motor tasks. In the water, where proprioceptive cues are limited, $K_V1.8^{-/-}$ mice did not maintain horizontal swim posture or stable head position. These vestibulomotor deficits likely occurred because impaired detection of high-frequency head motions in $K_V1.8^{-/-}$ mice failed to drive sufficient compensatory motions. These findings support the conclusion that

3.2 INTRODUCTION

Vestibular hair cells transduce head motions into receptor potentials that are strongly shaped by large outwardly rectifying K^+ conductances according to cell type. Here, we report that absence of the major outwardly rectifying K^+ conductances in mouse utricular type I and II hair cells lowered the lowpass corner frequency of receptor potentials and synaptic transmission, and resulted in poorer performance on challenging balance tasks.

Detecting high frequency head motions and stabilizing head position are critical to navigating life on land. During the transition to life on land, amniotes developed type I hair cells, which extend head motion detection into higher frequency ranges than the more ancient type II hair cells. Type I hair cells' most distinctive features are that they are enveloped by a calyceal afferent terminal (Wersäll, 1956; Lysakowski and Goldberg, 2004) and that they express $g_{K,L}$: a large, low-voltage-activated K^+ conductance (Correia and Lang, 1990; Rennie and Correia, 1994; Rüsch and Eatock, 1996a). Unlike the outwardly rectifying K^+ conductances in type II hair cells, which activate after depolarization positive to resting potential, $g_{K,L}$ is open at rest and lowers input resistance to reduce receptor potential charging time (e.g. $\tau_m = R_{in} * C_m$; Correia et al., 1996, Rüsch and Eatock, 1996b). Faster receptor potentials extend the receptor potential frequency range in type I hair cells (lowpass corner frequency, $f_{LP} = 1/(2\pi * \tau_m)$) and accelerate quantal glutamate release.

Calyx terminals also foster a novel form of non-quantal transmission with type I hair cells. Non-quantal transmission is a chemoelectrical coupling that reduces transmission delay by bypassing the biochemical steps of neurotransmitter release. During a receptor potential, K^+ flows out of basolateral hair cell K^+ channels, predominantly $g_{K,L}$, into the synaptic cleft; excess cleft K^+ depolarizes the afferent by raising the K^+ equilibrium potential, E_K (Lim et al., 2011; Contini et al., 2017, 2020), and the spatially confined ephaptic potential in the cleft (Govindaraju et al., 2023). $g_{K,L}$ augments non-quantal transmission by providing open channels for K^+ flow into the synaptic cleft (Songer and Eatock, 2013).

In contrast, the more ancient type II hair cells are contacted by smaller bouton terminals and engage only in quantal transmission. They have more conventional delayed rectifier (g_{DR}) and fast-inactivating A-type (g_A) K^+ conductances that are opened by depolarization above resting potential (V_{rest}). Type II hair cells are thought to encode low frequency head motions, such as static tilt relative to gravity.

These distinct K channel repertoires shape quite different roles for type I and II hair cells, yet we recently found that $g_{K,L}$, g_A, and part of g_{DR} all require $K_V1.8$ subunits (Martin et al., 2024). $K_V1.8$ knockout mice ($K_V1.8^{-/-}$) lack vestibular-evoked potentials, the synchronized activity of afferent nerve fibers responding to fast linear head motions (Lee et al., 2013).

In this study, we connect $K_V1.8$'s cellular roles to its overall importance for vestibular function. We performed physiology in the mouse utricle, which detects translational horizontal acceleration and head tilt when these forces displace a layer of crystals tethered to the sensory epithelium. We also tested mice for performance on challenging balance tasks.

$K_V1.8^{-/-}$ hair cells had larger but slower receptor potentials, consistent with Ohmic expectations. During receptor potentials, K^+ efflux from type I hair cells drives nonquantal

transmission with calyces; in $K_V1.8^{-/-}$ calyces, nonquantal postsynaptic signals had greater phase (slower response) and lower f_{LP} than control counterparts. Slower nonquantal transmission in $K_V1.8^{-/-}$ calyces may be due to slower receptor potentials as well as the additional time required for the residual delayed rectifier channels to open relative to $g_{K,L}$ (Martin et al., 2024). Poorer vestibular function at higher frequencies may have caused $K_V1.8^{-/-}$ mice, which otherwise performed normally on motor tasks, to struggle on challenging balance tasks and fail to suppress head tremor.

3.3 RESULTS

We recorded from type I and II hair cells and calyces from the extrastriolar utricles of 45 mice between postnatal day (P) 7 and P200. Hair bundles were displaced by a stiff probe with step and sinusoidal waveforms. We compared transducer currents (I_{MET}) and receptor potentials (V_{RP}) in type I and II hair cells from homozygous knockout ($K_V1.8^{-/-}$) animals and their wildtype ($K_V1.8^{+/+}$) or heterozygote ($K_V1.8^{+/-}$) littermates. $K_V1.8^{+/+}$ and $K_V1.8^{+/-}$ data were pooled because they did not differ in input resistance, resting membrane potential, or voltage dependence of K_V conductances (Martin et al., 2024). We focused on extrastriolar bundles, which are reliably intact after dissection at all ages, to record from enough transducing hair cells in mature (>P12) preps. Striolar bundles are less often intact, possibly because they couple differently to the otoconia, and this is especially true at older ages when extensive ossification requires a rougher dissection.

$K_V1.8$ channels reduced receptor potential gain and latency

Head motion-induced bundle deflections can be mimicked *in vitro* with stiff probe deflection of hair bundles. A single hair bundle is displaced in its preferred direction while a patch electrode has

whole-cell access to the hair cell body. In **Figure 3.1A**, inward transduction currents flow when step displacements open mechanotransduction channels at the tips of the hair bundles. Transduction currents subsequently adapt, or desensitize, by up to 70% (**Fig. 3.1A1-2, Suppl. Fig. S3.1A1-2**). Hair cells were routinely held negative to –80 mV to maximize mechanotransduction current and to improve voltage clamp quality by closing $g_{K,L}$ channels.

Transducer current mechanical sensitivity and time course were similar in control and $K_V1.8^{-/-}$ type I and II hair cells. Mechanical sensitivity was determined by plotting the $I_{MET}(X)$ relation (peak current against displacement) and fitting with a second-order sigmoidal activation function (Eq. 1, **Fig. 3.1A.3, Suppl. Fig. S3.1A.3**), producing a midpoint of activation ($X_{1/2}$) ~0.3 μm (**Table 3.1**). Time course was assessed qualitatively by overlapping the first 10 ms of step-evoked transducer current (**Fig. 3.1A.4, Suppl. Fig. S.3.1A.4**).

We switched to current clamp to record displacement-evoked receptor potentials. Note that, at baseline, membrane potential was more hyperpolarized in control than $K_V1.8^{-/-}$ type I hair cells (**Fig. 3.1B.1-2**) because $g_{K,L}$ anchors V_m closer to E_K.

Genotype strongly impacted the magnitude and time course of receptor potentials. In control type I hair cells, receptor potentials were small and unchanging with time because open $g_{K,L}$ channels minimized input resistance at baseline ($V = IR$, **Fig. 3.1B.1**). In contrast, $K_V1.8^{-/-}$ type I hair cells produced receptor potentials that were initially quite large due to high input resistance and subsequently relaxed as delayed rectifier K channels opened (**Fig. 3.1B.2**). Receptor potential-displacement curves (**Fig. 3.1B.3**) emphasize the difference in gain (mV/μm).

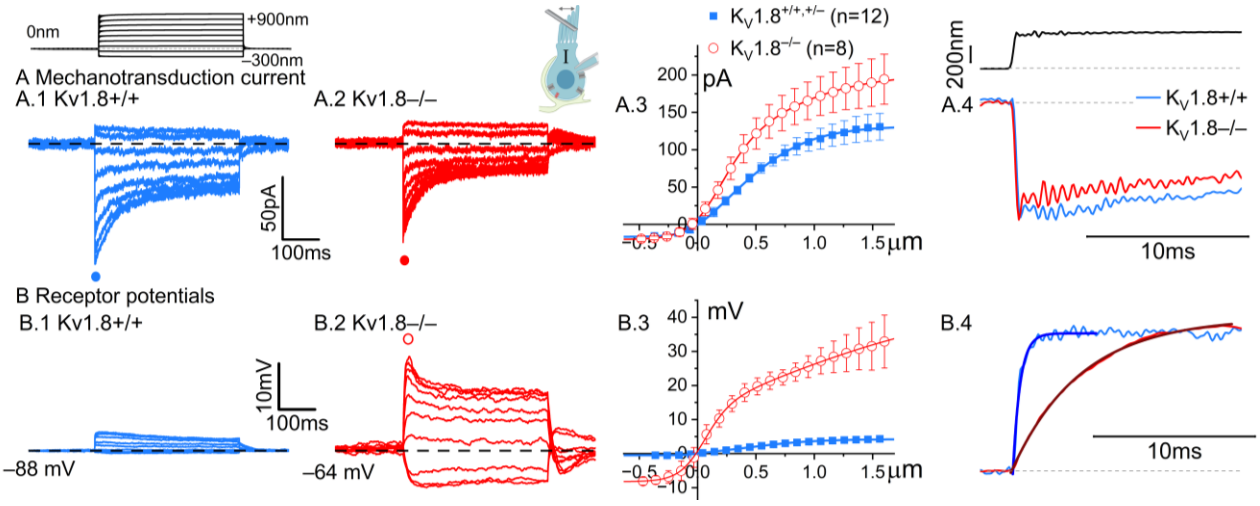

Figure 3.1. $K_V1.8^{-/-}$ type I hair cells produced larger but more delayed receptor potentials than $K_V1.8^{+/+,-/-}$ type I HCs. (**A**) Transduction current (I_{MET}) was similar across genotypes. The step stimulus above applies to the entire figure. Exemplar step-evoked transduction current at holding potentials –87 mV in A.1 and –84 mV in A.2. Averages of 3-6 presentations. (**A.3**) Peak $I_{MET}(X)$ relation were averaged across multiple cells and then fit with Eq. 3.2: *control,* x_1 0.4 nm, k_1 0.3 nm, x_2 0.02 nm, k_2 0.14 nm, I_{max} 148.2 pA, I_{min} –16.6 pA; *knockout,* x_1 0.14 nm, k_1 0.5 nm, x_2 0.24 nm, k_2 0.16 nm, I_{max} 223 pA, I_{min} –20.2 pA. (**A.4**) Onset responses to +0.5 µm displacement were similar. High frequency oscillations are undamped probe resonance.

(**B**) Receptor potentials (V_{RP}) were much larger and slower in $K_V1.8^{-/-}$ type I HCs. Exemplar step-evoked receptor potentials are from cells with different V_m. (**B.3**) Peak $V_{RP}(X)$ were averaged across cells and then fit with Eq. 3.2: *control,* x_1 0.45 nm, k_1 0.28 nm, x_2 –0.03 nm, k_2 0.07 nm, V_{max} 4.72 mV, V_{min} –0.49 mV; *knockout,* x_1 0.42 nm, k_1 1 nm, x_2 0.1 nm, k_2 0.12 nm, V_{max} 53.8 mV, V_{min} –8.24 mV. (**B.4**) Onset responses from to +0.5 µm displacements show the faster membrane time constant in $K_V1.8^{+/+,-/-}$ type I HCs. Double-exponential fits (Eq. 3.3) are overlaid. Statistics are in Table 1.

The payoff of lower gain is faster timing. Receptor potentials charged much more quickly in control than $K_V1.8^{-/-}$ type I hair cells (**Fig. 3.1B.4**). Exponential fits estimated the RC time constant (τ_m); low τ_m enabled control type I hair cell receptor potentials to occur as fast as the stimulus itself while high τ_m introduced delays into the $K_V1.8^{-/-}$ type II hair cell receptor potential.

In control type II hair cells, receptor potentials initially formed a sharp positive-going peak that relaxed as g_A's rapid activation and a decaying driving force repolarized the membrane toward an equilibrium (**Suppl. Fig. S3.1B.1**; Hudspeth & Lewis, 1988). In $K_V1.8^{-/-}$ type II hair cells, receptor

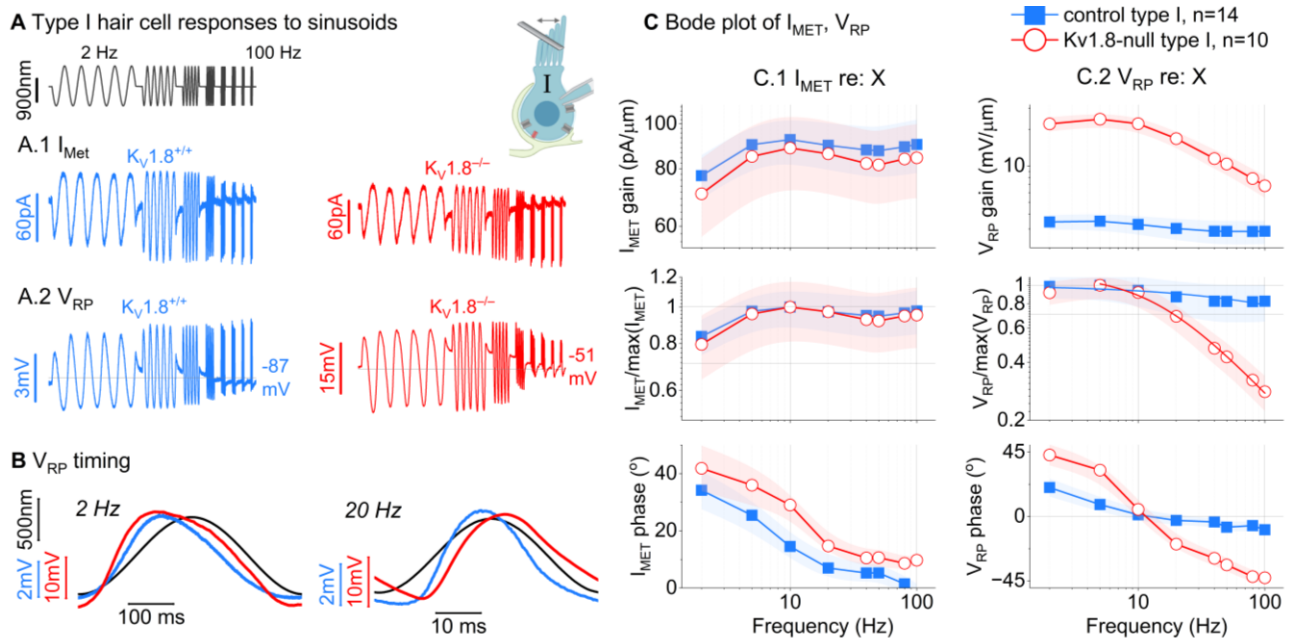

Figure 3.2. $g_{K,L}$ raised the lowpass corner frequency of receptor potentials, with the most impact on gain and response latency above 10 Hz. (**A**) I_{MET} and V_{RP} are averages of 6-13 presentations of the sinusoidal stimuli (X) at the top. Baseline potential is indicated to the right of each V_{RP} trace. (**B**) Single V_{RP} sinusoidal cycles are overlaid with the stimulus (black) to show the phase (timing) advance of the peak response of control relative to $K_V1.8^{-/-}$ HCs: (**C-D**) Gain and phase of responses referenced to input signals as functions of frequency; mean ± SEM values (see key for n). ***C***, I_{MET} referenced to X : peak-to-peak gain (***C.1,*** actual, ***C.2,*** normalized) and phase (***C.3***). ***D***, V_{RP} referenced to X; peak-to-peak gain (***D.1,*** actual, ***D.2,*** normalized) and phase (***D.3***).

potentials were larger because of higher input resistance and relaxed slowly (**Suppl. Fig. S3.1B.2**). Relaxation was faster in controls (**Suppl. Fig. S3.1B.4**) because g_A has faster activation kinetics than the residual K_V7 delayed rectifier channels in $K_V1.8^{-/-}$ type II hair cells (Martin et al., 2024).

$K_V1.8^{-/-}$ HC receptor potentials had lower lowpass corner frequencies

Natural head motions are often analyzed in the frequency domain. To examine how the large differences in step-evoked responses affect tuning, we displaced bundles with 2-100 Hz sinusoids (**Fig. 3.2A-B, Suppl. Fig. S3.2A-B**), which spans the upper range of natural head motion

Table 1. Genotype comparisons of transduction and adaptation in extrastriolar hair cells. Mean ± SEM (number of cells, all extrastriolar). g is effect size, Hedge's g. A, ANOVA; W, Welch ANOVA; K, Kruskal-Wallis.

				G(X) Boltzmann parameters			Adaptation at $X_{1/2}$	
Type	**K_V1.8 Genotype**	**n**	**Age (median)**	**Max G_{MET} (nS)**	**$X_{1/2}$ (nm)**	**S (nm)**	**τ_F (ms)**	**τ_S (ms)**
I	+/+,+/–	13	7-29 (19)	1.9 ± 0.2	350 ± 40	300 ± 30	39 ± 9 (10)	300 ± 90 (7)
	–/–	8	15-60 (45)	2.5 ± 0.3	300 ± 50	230 ± 30	12 ± 3 (8)	100 ± 40 (6)
			p-value:	A 0.13	K 0.19	K 0.06	W 0.013	K 0.03
			g:				1.27	1.01
		Statistics	**NS power**:	0.33				
II	+/+,+/–	8	7-47 (20)	1.6 ± 0.2	200 ± 50	240 ± 40	13 ± 2 (8)	160 ± 90 (7)
	–/–	8	6-60 (49)	2.5 ± 0.5	290 ± 100	240 ± 40	13 ± 2 (4)	160 ± 90 (4)
			p-value:	K 0.058	A 0.33	A 0.99	A 0.8	A 0.96
		Statistics	**g:**					
			NS power:		0.16	0.06	0.06	0.05

Table 2. Genotype comparisons of receptor potential magnitude and speed in extrastriolar hair cells.

				V(X) Boltzmann parameters			Onset kinetics
Type	**K_V1.8 Genotype**	**N**	**Age (median)**	**Max V_{RP} (mV)**	**$X_{1/2}$ (nm)**	**S (nm)**	**τ_{Onset} (ms) at $X_{1/2}$**
I	+/+,+/–	11	7-29 (19)	**6.5 ± 0.6**	**390 ± 50**	250 ± 20	0.4
	–/–	8	15-60 (45)	41 ± 4	100 ± 90	270 ± 40	1.8
			p-value:	W 8.2E-5	W 2.5E-4	K 0.74	K 0.005
		Statistics	**g:**	4.0	2.0		
			NS power:				
II	+/+,+/–	8	7-47 (20)	39 ± 5	150 ± 60	290 ± 50	1.5
	–/–	7	6-60 (49)	51 ± 6	130 ± 40	170 ± 30	2.3
			p-value:	A 0.33	A 0.82	A 0.06	K 0.7
		Statistics	**g:**				
			NS power:	0.16	0.06	0.49	

frequencies in mice (Carriot et al., 2017). We analyzed the response gain, normalized gain, and phase as functions of frequency (**Fig. 3.2C, Suppl. Fig. 3.2C**).

I_{MET} did not differ by genotype in type I or II hair cells. Peak-to-peak gain increased gently from 2 to 100 Hz in data traces (**Fig. 3.2A.1, Suppl. Fig. S3.2A.1**), reflecting the high-pass filter property of transducer adaptation (**Fig. 3.2C.1, Suppl. Fig. S3.2C.1**). I_{MET} phase declined with increasing frequency (**Fig. 3.2C.1**, **Suppl. Fig. S3.2C.1**), consistent with a high-pass filter in this

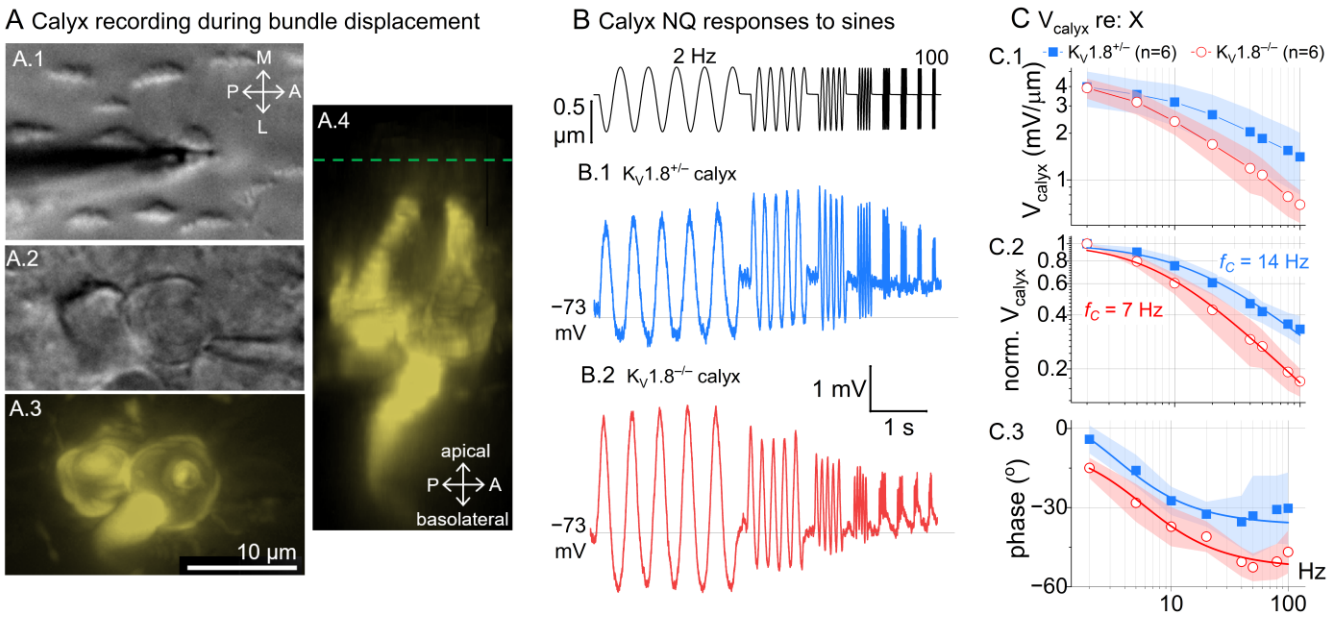

Figure 3.3. Synaptic transmission in $K_V1.8^{-/-}$ utricles had reduced gains at higher frequencies. (**A**) Exemplar afferent arbor bearing two calyces in the lateral extrastriola. (**A.1**) DIC image of stiff probe placed behind the bundle of the type I HC enclosed in the rightmost calyx being patched, seen in DIC (**A.2**) and in the maximum intensity projection of the dye fill (**A.3**). (**A.4**) 3D projection of the dye filled afferent arbor. Dotted line is level of cuticular plates. Scalebar (10 µm) applies to all. *Compass rose*: medial (M), lateral (L), posterior (P), anterior (A). (**B**) Sinusoidal type I HC bundle deflections drove voltage responses in extrastriolar calyces. Stimulus trace is an offline photodiode recording of probe motion. (**C**) Gain, normalized gain, and phase of sinusoidal responses were referenced to the stimulus and plotted against frequency. Datapoints are extrastriola population means with shaded SEM: control n=6, P12-105, median P99; null n=6, P15-220, median P37. (**C.1**) Calyx voltage gains were greatest and most similar at 2 Hz in $K_V1.8^{-/-}$ and $K_V1.8^{+/-}$ synapses. (**C.2**) Calyx responses were normalized to their best frequency, and population averages were fit with Eq 3.4: *control*, f_{LP} 13.9 Hz, n 0.57; *knockout*, f_{LP} 7, n 0.67. (**C.3**) Phase of the responses re: stimulus, fit with Eq 3.5: *control*, steepness 31°, f_{LP} 21 Hz, baseline 13°; *knockout*, steepness 31°, f_{LP} 37 Hz, baseline –5°.

range. In all cases, as stimulus frequency increased, I_{MET} increased and response phase decreased, from a lead of 20° at 2 Hz to 0° (in phase) at 100 Hz

V_{RP} magnitude was constant across frequency in control but started decreasing above 10 Hz in $K_V1.8^{-/-}$ type I hair cells (**Fig. 3.2A.2**). Control and $K_V1.8^{-/-}$ V_{RP} responses were normalized (**Fig.**

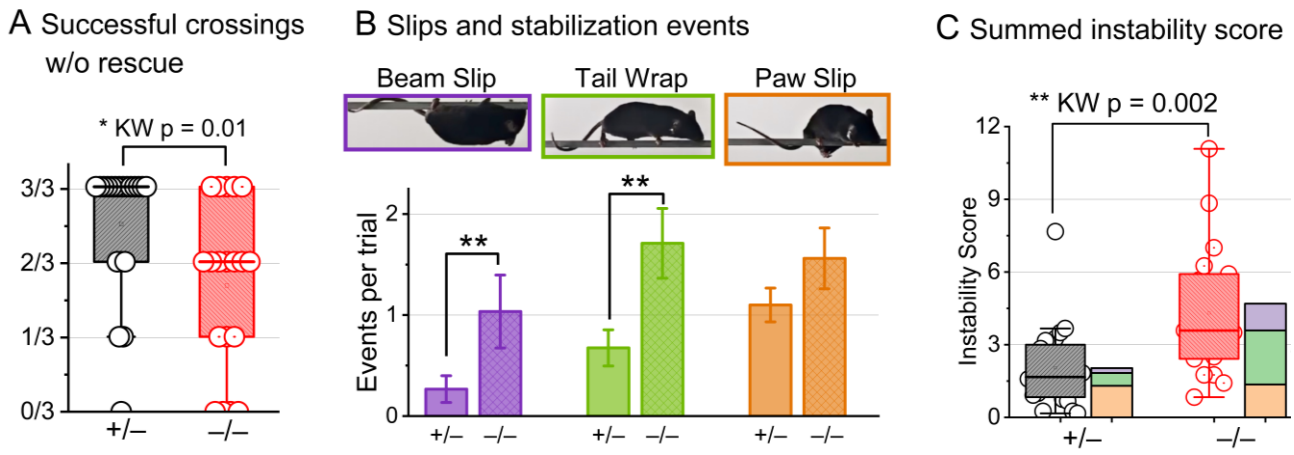

Figure 3.4. $K_V1.8^{-/-}$ mice display signs of difficulty and compensatory strategies while crossing narrow balance beam. (**A**) Fraction of trials on which mice crossed without requiring rescue. (**B**) Occurrences of three key behavioral events per trial per mouse were summed in (**C**) as an Instability Score to account for individual variability. Statistics for $K_V1.8^{+/-}$ and $K_V1.8^{-/-}$ mice in Table 3.3.

3.2C.2) and fit with a lowpass filter transfer function (Eq. 3.4) to estimate f_{LP} (inversely related to RC time constant). Control V_{RP} had a flat voltage-frequency relationship (f_{LP} = 230 Hz) whereas $K_V1.8^{-/-}$ V_{RP} fell off (f_{LP} = 14 Hz).

In $K_V1.8^{-/-}$ type I hair cells, decreased gain above 10 Hz was associated with delays in response timing. **Figure 3.2B** overlays single cycle responses at 2 and 20 Hz with the stimulus trace to demonstrate responses delays. At 2 Hz, both control and $K_V1.8^{-/-}$ responses peaked before the stimulus (phase > 0°), but, at 20 Hz, only the control response maintained a positive phase lead whereas the $K_V1.8^{-/-}$ response lagged the stimulus (phase < 0°).

In control type II hair cells, V_{RP} showed bandpass tuning: a highpass filter dominated below 10 Hz while a lowpass filter (f_{LP} = 70 Hz) dominated above 20 Hz (**Suppl. Fig. S3.2C.2**). The highpass filter may be a function of both transducer adaptation and K_V activation kinetics, which in control cells was sufficiently fast (τ = ~7 ms at –30 mV) to actively reduce gain below 10 Hz. At 20 Hz, K_V channels finished activating *after* V_{RP} had charged, resulting in a skewed response of a prominent peak that then relaxed (**Suppl. Fig. 3.2B**). More examples are found in step-evoked

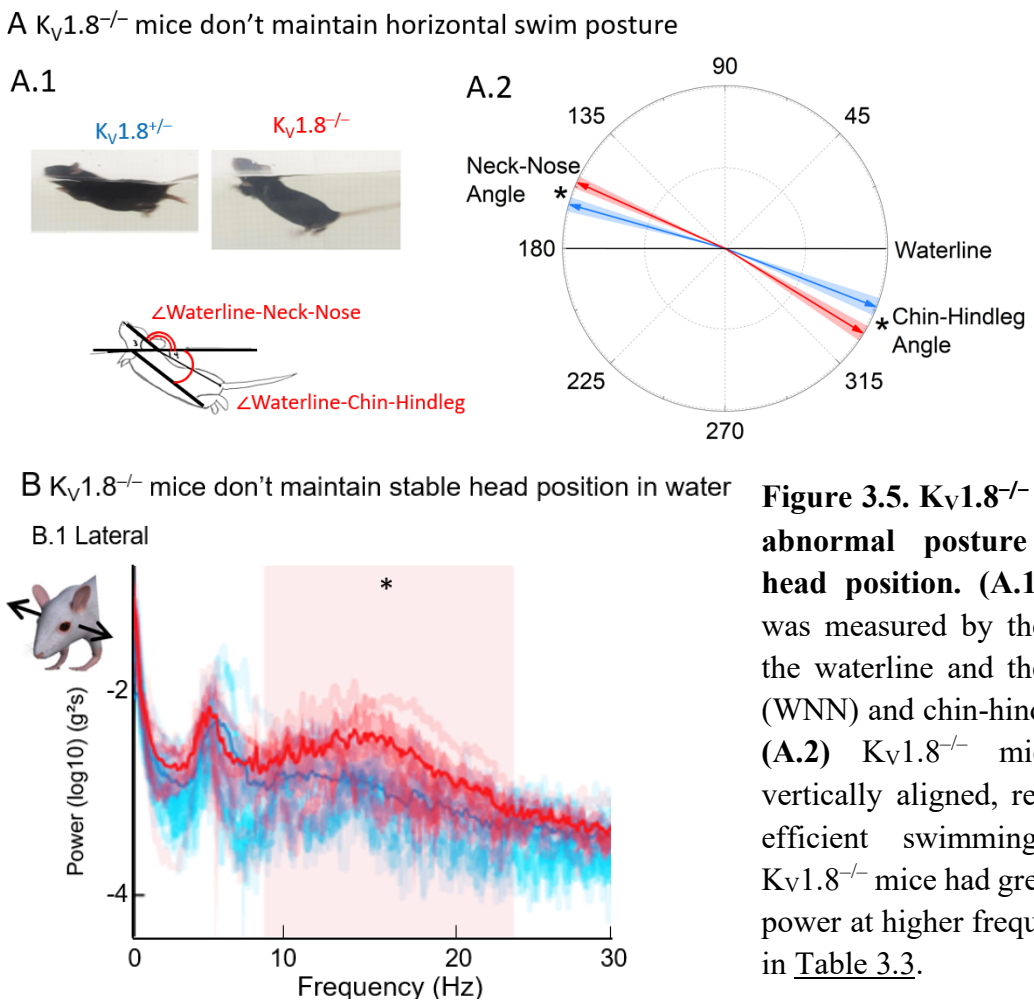

Figure 3.5. $K_V1.8^{-/-}$ mice swim with abnormal posture and unstable head position. (A.1) Swim posture was measured by the angle between the waterline and the neck-nose line (WNN) and chin-hindleg line (WCT). **(A.2)** $K_V1.8^{-/-}$ mice were more vertically aligned, resulting in a less efficient swimming posture. **(B)** $K_V1.8^{-/-}$ mice had greater head motion power at higher frequencies. Statistics in Table 3.3.

responses (**Suppl. Fig. S3.1B.1, B.4**) and other studies (Holt et al., 1999). The response skew contributed to the phase-frequency relationship in control type II hair cells where V_{RP} phase lead increased from 2 to 5 Hz (**Suppl. Fig. S3.2C.2**).

In $K_V1.8^{-/-}$ type II hair cells, V_{RP} showed simple lowpass tuning (f_{LP} = 27 Hz, **Suppl. Fig. 3.2**). $K_V1.8^{-/-}$ type I and II hair cells had similar tuning because they share the same K_V7 delayed rectifiers (Martin et al., 2024).

Synaptic transmission at $K_V1.8^{-/-}$ calyces

The type I hair cell-calyx synapse fosters an unusual non-quantal form of synaptic transmission that involves K^+ flow in the calyceal cleft, primarily through $g_{K,L}$ (Govindaraju et al., 2023).

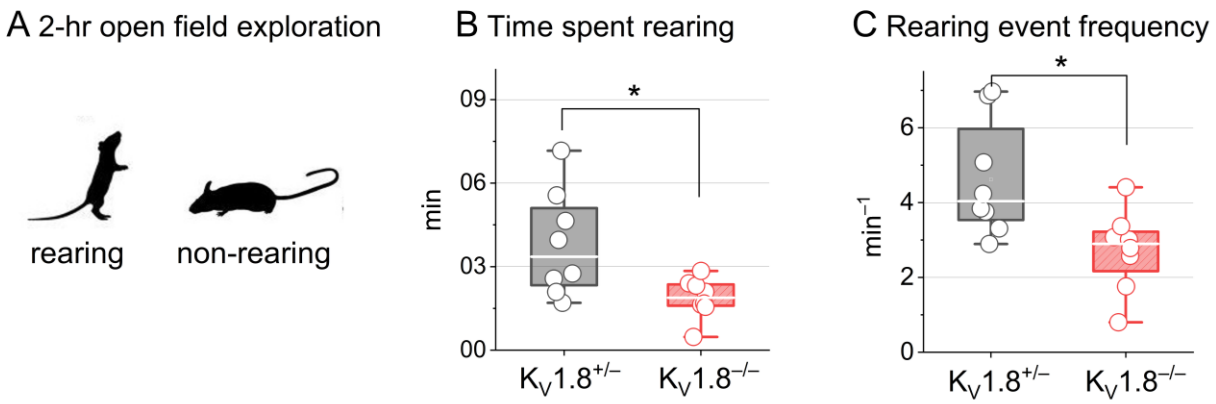

Figure 3.6. $K_V1.8^{-/-}$ mice were less likely to rear on their hind paws. (**A**) Time spent rearing was compared to time spent not-rearing, which included quiet rest as well as active movement on all four paws. $K_V1.8^{-/-}$ mice spent less time rearing (**B**) and reared less often (**C**). No differences were detected in overall activity and centrophobism (**Table 3.4**).

Without $g_{K,L}$, $K_V1.8^{-/-}$ type I hair cells may drive slower nonquantal responses. We first characterized the intrinsic properties of calyces and did not detect differences between control and $K_V1.8^{-/-}$ calyces in their passive properties (R_{in}, V_m, C_m), firing patterns elicited by current injection, or voltage-gated currents ($I_{K,L}$, I_H) (**Suppl. Fig. S3.4, Suppl. Table S3.1**), indicating similar baseline conditions and absence of noticeable compensation. To measure nonquantal transmission, we displaced the bundle of a type I hair cell while recording from its calyx in whole-cell patch clamp (**Fig. 3.3A**).

Sinusoidal bundle stimulation evoked bidirectional voltage fluctuations in the calyx that closely resembled hair cell receptor potentials (**Fig. 3.3B**). Quantal events such as excitatory postsynaptic potentials were not observed. Peak-to-peak responses were greatest at 2 Hz (~4 mV/μm, **Fig. 3.3C.1**). We fit population averages to Eq. 3.4 to estimate f_{LP}, which quantifies how response magnitude and phase decrease with increasing frequency. f_{LP} was higher in control (14 Hz, n=6) than $K_V1.8^{-/-}$ calyces (7 Hz, n=6, **Fig. 3.3C.2**). In the absence of $g_{K,L}$, signals produced by non-quantal transmission were smaller at higher frequencies (**Fig. 3.3C.1-C.2**) and slower at all

frequencies tested (**Fig. 3.3C.3**). These deficits likely affect downstream vestibular circuits that compensate for rapid head motions.

$K_V1.8^{-/-}$ mice had specific deficits on challenging balance tasks

Behavioral experiments were conducted in 73 mice between 2 and 12 months old (distribution of ages and sex found in **Table 3.3** and **Suppl. Table S3.2**). $K_V1.8^{+/-}$ littermates were used as controls for three reasons: (1) the dominant breeding strategy produced many $K_V1.8^{+/-}$ pups, (2) type I hair cell K_V currents did not differ between $K_V1.8^{+/+}$ and $K_V1.8^{+/-}$ (Martin et al., 2024), and (3) $K_V1.8^{+/-}$ mice carried a copy of the genetic locus that was disrupted with a beta-galactosidase gene (Lee et al., 2013).

$K_V1.8^{-/-}$ mice were healthy, developed normally, and did not display overt signs of vestibular dysfunction such as circling and head tilt (Lee et al., 2013, **Suppl. Fig. 3.4A**). $K_V1.8$ is not expressed in neural tissue, but some reports in skeletal muscle and kidney led us to first characterize their behavior on general motor and motor learning tasks. Motor learning was similar in $K_V1.8^{-/-}$ and control mice as both learned a rotarod task in the light (**Suppl. Fig. 3.4B, Suppl. Table S3.2**). Genotype differences in gait and grip strength were not detected (**Suppl. Table S3.2**).

In an open area, $K_V1.8^{-/-}$ and control mice behaved similarly on most counts, including overall activity, distance travelled, and centrophobism (**Suppl. Table S3.2**). However, $K_V1.8^{-/-}$ mice were less likely to rear up on their hindlegs, a normal exploratory behavior (**Fig. 6**). The absence of anxiety-like symptoms in $K_V1.8^{-/-}$ mice suggests that deficits in this exploratory behavior may have arisen because $K_V1.8^{-/-}$ mice are less able to balance in unstable bipedal positions. We further investigated mouse performance on challenging balance tasks.

Ono et al. (2020) showed that a narrow balance beam can reveal balance deficits that are not evident in standard tests, such as rotarod or balance beam of typical (wider) dimensions. Most

Table 3.3. Vestibulomotor performance was significantly different between $K_V1.8^{+/-}$ and $K_V1.8^{-/-}$ mice. Mean ± SEM (number of mice). g is effect size, Hedge's g. KWA is Kruskal-Wallis ANOVA.

Balance Beam								
Genotype	Instability score	Paw Slips	Tail Wraps	Beam Slips	Success Rate	Time To Cross (s)	N	Age range (month, median)
$K_V1.8^{+/-}$	2 ± 0.4	1.1 ± 0.2	0.7 ± 0.2	0.3 ± 0.1	0.83 ± 0.07	15 ± 2	9M, 11F	3.1-6.9 (4.4)
$K_V1.8^{-/-}$	4.3 ± 0.6	1.6 ± 0.3	1.7 ± 0.3	1 ± 0.4	0.56 ± 0.08	20 ± 4	8M, 11F	2-6.9 (3.8)
p-value:	KWA 0.002	KWA 0.2	KWA 0.004	KWA 0.0096	KWA 0.0095,	KWA 0.28		
effect size:	3.17		g	g	2.55			
power:								

Swim Posture						
Genotype	Waterline-Chin-Hindleg angle (°)	Waterline-Chin-Tail angle (°)	Waterline-Neck-Nose angle (°)	Waterline-Neck-Tail (°)	N	Age range (month, median)
$K_V1.8^{+/-}$	21 ± 3	10 ± 3	164 ± 3	17 ± 4	4M, 4F	2.9-5.5 (5.2)
$K_V1.8^{-/-}$	32 ± 3	20 ± 3	156 ± 2	20 ± 4	6M, 4F	2.9-7 (5.5)
p-value:	ANOVA 0.03	ANOVA 0.054	KWA 0.03	ANOVA 0.048		
effect size:	2.4	2.1	2.4	2.1		
power:		0.5				

Open Field Test							
Genotype	Rearing event count	Time rearing	Centerphobism	Distance travelled	Average Velocity	N	Age range (month, median)
$K_V1.8^{+/-}$	550 ± 70	2.6 ± 0.5	11 ± 2	4.2 ± 0.5	115 ± 9	4M, 4F	1.4-3.7 (2.1)
$K_V1.8^{-/-}$	330 ± 30	1.3 ± 0.2	9 ± 2	3.7 ± 0.6	105 ± 5	4M, 4F	1.4-3.7 (1.9)
p-value:	ANOVA 0.01	Welch 0.02	ANOVA 0.5	ANOVA 0.8	Welch 0.3		
effect size:	2.0	2.7					
power:			0.09	0.08	0.2		

(83%) control but only half (56%) $K_V1.8^{-/-}$ mice crossed successfully without requiring rescue after slipping off the beam ($p<0.01$, **Fig. 3.4A**). Overall, $K_V1.8^{-/-}$ mice were more likely to slip off the beam and compensated by more frequently wrapping their tails around the beam for additional stability (**Fig. 3.4B**).

Vestibular input is particularly necessary in the water, where there is an absence of normal proprioceptive cues (Jones et al., 2004). When placed in water, both control and $K_V1.8^{-/-}$ mice

stayed afloat; however, $K_V1.8^{-/-}$ mice failed to maintain the horizontal, efficient swim posture adopted by control mice (**Fig. 3.5A**).

Head stabilization is an important application of vestibular information (Zobeiri et al., 2021). At postnatal day 9 (P9), $K_V1.8^{-/-}$ pups exhibited bouts of head tremor not observed at other ages or in control animals (anecdotal). We quantified the tremor phenotype in adult mice by recording head motion with head-mounted IMU gyroscopes and comparing the power spectra of head motion traces between control and $K_V1.8^{-/-}$ animals (**Fig. 3.5B**). In water, motion power was higher in the 10-30 Hz range in $K_V1.8^{-/-}$ mice for fore-aft (utricle), lateral (utricle and saccule), and vertical (saccule) translations (**Fig 3.5B, Suppl. Fig. S3.5**). We are currently collecting more data to enable statistical analysis.

Overall, $K_V1.8^{-/-}$ mice showed deficits in a range of balance tasks, but not general motor performance.

3.4 DISCUSSION

We have shown that constitutive knockout of $K_V1.8$ greatly decreased lowpass corner frequencies in type I and II hair cells, reducing non-quantal transmission to calyx afferents at very high frequencies. $K_V1.8$ knockout impaired multiple vestibulomotor behaviors: balancing on a narrow beam, posture stabilization in water, suppression of head tremor, and voluntary engagement in unstable exploratory behaviors. $K_V1.8$ knockout did not affect transduction currents, calyx intrinsic properties, or non-balance motor tasks. We conclude that $K_V1.8$'s role in extending the

frequency range of receptor potentials in both type I and II hair cells is necessary for performing challenging balance tasks.

K_V1.8 and signal processing (receptor potentials and synaptic transmission)

K_V1.8 extended receptor potential tuning to higher frequencies because it lowered the membrane time constant by reducing input resistance. The biophysical properties of each K_V1.8 conductance tuned receptor potentials differently in type I and II hair cells. $g_{K,L}$ confers such a low R_{in} that type I HC receptor potentials had flat, frequency-independent phase and gain relationships up to 100 Hz. In type II HCs, g_A's rapid activation generated a more dynamic phase and gain relationship with bandpass tuning that peaked at 20 Hz.

Like controls, $K_V1.8^{-/-}$ calyces produced nonquantal voltage responses to hair bundle displacement. These postsynaptic depolarizations occur when K^+ flows into the cleft from hair cell voltage-gated K and HCN channels; K^+ accumulation in the cleft raises E_K, which reduces resting K^+ current through low-voltage-activated K channels on the calyx inner face and depolarizes the calyx arbor (Govindaraju et al., 2023). In $K_V1.8^{-/-}$ calyces, nonquantal postsynaptic signals had greater phase (slower response) and lower f_{LP} than control counterparts. Slower nonquantal transmission in $K_V1.8^{-/-}$ calyces may be due to slower receptor potentials as well as the additional time required for the residual delayed rectifier channels to open relative to $g_{K,L}$ (Martin et al., 2024).

In this study, we observed substantial lowpass filtering in the synaptic transfer function at calyces. For displacement-evoked signals, f_{LP} was much lower in calyces (*control*, ~14 Hz; *null*, ~7 Hz) than type I hair cells (*control*, >100 Hz; *null*, ~20 Hz). We attribute some of this lowpass filtering to the calyx's own membrane time constant, an estimated 1.2 ms (**Suppl. Table S3.1**),

which corresponds to a theoretical f_{LP} of 110 Hz. To understand other factors in nonquantal transmission, we are collaborating on a computational model of the type I HC-calyx synapse with Rob Raphael's group at Rice University.

We have previously reported non-quantal transmission with higher frequency tuning (Songer et al., 2013). In that study, wildtype subthreshold nonquantal responses had f_{LP} = ~70 Hz (estimated from Songer's Fig. 5D), much higher than the 14 Hz value in this study (our **Fig. 3.3C.2**). Meaningful differences between the experiments could account for the discrepancy: organ (Songer, saccule; here, utricle), epithelia zone (striola; extrastriola), calyx type (double; single), displacement intensity (0.3 μm; 1 μm), species (rat; mouse), and age (P4; P12-202).

Greater f_{LP} is part of the saccule striola's specialization for high frequency stimuli in many species. The saccule striola serves as a hearing organ in fish, responds to bone-conducted vibrations (Curthoys et al., 2016), and drives the ultrafast vestibular-evoked potential (VsEP). The VsEP is the extremely rapid (latency ~80 μs, Jones et al., 2011) and synchronized activity of striolar saccule afferents in response to head jerk (derivative of acceleration). VsEPs are absent in $K_V1.8^{-/-}$ mice (Lee et al., 2013), and our data from the utricle extrastriola suggest that $K_V1.8^{-/-}$ hair cells in the saccule striola would also be unable to detect and transmit the high frequency jerk stimulus to afferents. It is further possible that $K_V1.8$ plays additional roles in the saccule striola to facilitate the afferent synchronization necessary for the VsEP.

Our single-cell experiments may not fully explain the nature of $g_{K,L}$'s relationship with nonquantal transmission. Deflection of single hair bundles does not perfectly replicate the forces at play *in vivo* during simultaneous displacement of all utricular bundles, when the rise in global extracellular K^+ may have a cooperative effect on afferent excitation that increases with the number of hair cells recruited. Extracellular K^+ may serve as a non-synaptic means of synchronizing

multiple afferents. The inability of single-cell methods to capture network effects underscores the need for population studies of the utricle.

Relevance of $K_V1.8$ for vestibulomotor behaviors

Abolition of hair cell function can lead to overt vestibular deficits such as circling, head tilt, and inability to swim. In $K_V1.8^{-/-}$ mice, hair cell and synaptic function persisted with specific deficits only in the high frequency range, resulting in subtle but impactful impairments in challenging balance tasks.

$K_V1.8^{-/-}$ mice often required rescue to cross a narrow balance beam and wrapped their tails around the beam as a compensatory balance strategy. Tail wrapping has been observed in rod-crossing assays of deer mice (Hager & Hoekstra, 2021), but not previously reported in vestibular mutants. The emergence of tail wrapping in $K_V1.8^{-/-}$ mice may reflect the moderate phenotype or constitutive nature of the knockout, which allowed mice 2+ months to learn compensatory strategies.

$K_V1.8^{-/-}$ mice failed to maintain a horizontal, efficient swim posture. An impaired ability to sense gravity and adjust posture may reflect the $K_V1.8$ knockout's effect on type II hair cells, which are associated with detecting static position relative to gravity (Maroto et al., 2021).

A head tremor was transiently visible in $K_V1.8^{-/-}$ pups at P9 and subsided at older ages, potentially because mice began to rely on other sensory systems to stabilize head position. The tremor severity at P9 reflects a critical window in sensory development: after vestibular hair cells have acquired $K_V1.8$ conductances in controls (Martin et al., 2024; Scheffer et al., 2015) and before the eyes and middle ear open at P12.

A small head tremor persisted at higher frequencies (10-30 Hz) in $K_V1.8^{-/-}$ adults. We suggest two possibilities: (1) reduced detection of high frequency head motions by $K_V1.8^{-/-}$ vestibular hair cells was not enough to drive neck muscles to stabilize the head in real time, and (2) aberrant vestibulomotor activity arose from the spontaneous 2-20 Hz resonance observed in some $K_V1.8^{-/-}$ type II hair cells (Martin et al., 2024). Comparison to a related vestibular mutant, *Striolarless*, supports (1). *Striolarless* mice lack the zone specialized for high frequency head motion detection, have absent VsEPs, have normal type II HCs, and, like $K_V1.8^{-/-}$ mice, have a transient head tremor at P9 that becomes smaller and higher frequency with age (Ono et al., 2020).

Since $K_V1.8$ has been deleted everywhere, not all deficits can be attributed to specific zones, cell types, or endorgans within the inner ear. However, the absence of general motor deficits in $K_V1.8^{-/-}$ mice suggests that these vestibulomotor deficits arise because information about high frequency head motions was not sufficiently transmitted to drive compensatory head, neck, and eye movements.

3.5 MATERIALS AND METHODS

Preparation

All procedures for handling animals followed the NIH Guide for the Care and Use of Laboratory Animals and were approved by the Institutional Animal Care and Use Committees of the University of Chicago and the University of Illinois Chicago. All mice belonged to a transgenic line with a knockout allele of *Kcna10* (referred to here as $K_V1.8^{-/-}$). Our breeding colony was established with a generous gift of such animals from Sherry M. Jones and Thomas Friedman. These animals are described in their paper (Lee et al., 2013). Briefly, the Texas A&M Institute for

Genomic Medicine generated the line on a C57BL/6;129SvEv mixed background by replacing Exon 3 of the *Kcna10* gene with an IRES-bGeo/Purocassette. Mice in our colony were raised on a 12:12h light-dark cycle with access to food and water *ad libitum*.

Preparation, stimulation, and recording methods followed our previously described methods for the mouse utricle (Vollrath and Eatock, 2003). Mice (P6-60) were anesthetized through isoflurane inhalation. After decapitation, each hemisphere was bathed in ice-cold, oxygenated Liebowitz-15 (L15) media. The temporal bone was removed, the labyrinth was cut to isolate the utricle, and the nerve was cut close to the utricle. The utricle was treated with proteinase XXIV (100 mg/mL, ~10 mins, 22ºC) to facilitate removal of the otoconia and attached gel layer and mounted beneath two glass rods affixed at one end to a coverslip.

Electrophysiology

We used the HEKA Multiclamp EPC10 with Patchmaster acquisition software, filtered by the integrated HEKA filters (a 6-pole Bessel filter at 10 kHz and a 4-pole Bessel filter at 5 kHz), and sampled at 10-100 kHz. Recording electrodes were pulled (PC-100, Narishige) from soda lime glass (King's Precision Glass R-6) wrapped in paraffin to reduce pipette capacitance. Internal solution contained (in mM) 135 KCl, 0.5 $MgCl_2$, 3 MgATP, 5 HEPES, 5 EGTA, 0.1 $CaCl_2$, 0.1 Na-cAMP, 0.1 LiGTP, 5 $Na_2CreatinePO_4$ adjusted to pH 7.25 and ~280 mmol/kg by adding ~30 mM KOH. External solution was Liebowitz-15 media supplemented with 10 mM HEPES (pH 7.40, 310 ± 10 mmol/kg). Recordings were conducted at room temperature (22-25ºC) to preserve the lifespan of valuable preps and to minimize the electrical noise and physical constraints of warming devices during challenging experiments. Pipette capacitance and membrane capacitance transients were subtracted online with Patchmaster software. Series resistance (8-12 MΩ) was

measured after rupture and compensated 0-80% with the amplifier. Potentials are corrected for remaining (uncompensated) series resistance and liquid junction potential of ~4 mV, calculated with LJPCalc software (Marino et al., 2014).

Type I HCs with $g_{K,L}$ were transiently hyperpolarized to –90 mV to close $g_{K,L}$ enough to increase R_{in} above 100 MΩ, as needed to estimate series resistance and cell capacitance. The average resting potential, V_{rest}, was –87 mV ± 1 (41), similar to the calculated E_K of –86.1 mV, which is not surprising given the large K^+ conductance of these cells. V_{rest} is likely more positive *in vivo*, where lower endolymphatic Ca^{2+} increases standing inward current through MET channels.

Transduction

Hair bundles were deflected by a stiff probe (borosilicate, tip width <1 μm) attached to a piezoelectric planar bimorph. Driving voltage to the bimorph was lowpass filtered by an 8-pole Bessel filter (Active Tunable Filter Model 900, Frequency Devices, Ottawa, IL) at a corner frequency of 1000 Hz (resonant frequency = 2250 Hz). Probe time course was monitored offline by projecting the probe image onto the edge of a photodiode (PIN-6D). At the end of each experiment, steady-state probe tip distance per driving voltage was measured using a slow step stimulus, camera, and DIC illumination. In figures, probe stimuli traces are photodiode signals scaled to the known voltage sensitivity of the probe.

We evoked I_{MET} and V_{RP} by displacing the hair bundle along its sensitive axis with a stiff glass rod placed behind and approximately halfway up the hair bundle. Resting probe position was selected to be 10-20% of the operating range of the bundle, evoking 16 ± 2 % (n = 38) of maximum I_{MET} $[100*(I_{X=0} – I_{min})/(I_{max} – I_{min})]$. We expect this imposed resting position to be slightly higher

than natural resting position because we pushed the bundle slightly to ensure mechanical coupling with the probe. To record I_{MET}, most HCs were held at –84 mV to increase driving force on IMET and reduce noise from voltage-gated channels. Some type I HCs were held negative to –84 mV to fully deactivate $g_{K,L}$, which is so large as to degrade the voltage clamp (see Chapter 4).

Behavior

Animals were introduced to the behavior room the day before experiments.

Balance Beam: Animals were allowed at least 5 minutes to acclimate to the testing room. Mice were trained for 3 trials on a wide beam (12 mm wide), given 10 minutes of rest, and then tested for 3 trials on a narrow beam (6 mm wide). To incentivize mice to cross the flat beam, a bright lamp was put at the start of the beam, and a dark goal box (5 in x 5 in x 5 in) filled with food and bedding from their home cage was placed at the end of the beam. Mice were given at least 20 seconds to rest in the end box between trials. The beam was cleaned with Clidox-S between mice. Videos of the trial were taken at 30 frames per second (fps) with a lateral view of the beam. For manual scoring analysis, two genotype-blind scorers marked the following behaviors: “beam slip”, hanging upside down on the beam and needing rescue to finish (rescue time was included in total time to cross); “tail wrap”, wrapping the tail around the beam instead of having it in the air; and “paw slip”, a single paw slipping off the beam without the mouse falling off the beam. The crossing time was recorded as the time between the nose crossing the starting line and the nose crossing the finish line (64 cm). Crossing time included non-ambulatory epochs, including while the mouse was being rescued and while the mouse stopped and sniffed the air.

Swim test: A clear aquarium (38x30x25 cm) was filled with warm water (30°C) and placed in front of a white background. Animals were placed directly into the water. Videos (30 fps) of the animal's swim were recorded from the lateral side of the container, with the height aligned to the waterline. After 30 seconds, animals were retrieved, dried with paper towels, and placed in a cardboard box under a heat lamp. Videos were trimmed to the first section where the animal was swimming straight on the side closest to the camera. In eight random frames, two genotype-blind scorers marked body parts and calculated body angles in FIJI (Enthoven et al., 2004).

Open field: Animals were placed in open field boxes (17 in. x 17 in.) with dim lighting (16 lux) to avoid excessive stress. After 10 minutes of acclimation, mouse movement was recorded for 2 hours via infrared beam interruption. Activity Monitor 7 software (Med Associates, Inc, Fairfax, VT) returned data on the location of the mouse through time, and calculated Distance Travelled, Number of Ambulatory Episodes, Average Speed, Centrophobism, Jump Events, Rearing Events, and Rearing Time.

Rotarod: The Columbus Instruments Rotarod was used with large dowels (diameter = 7 cm) and was cleaned with Clidox-S between mice. We used a 2-day protocol. On Day 1, there were 6-8 training trials wherein mice were initiated at 5 rpm before the ramp accelerated from 5 rpm to 44 rpm at a rate of 2.4 rpm per 4 seconds, with 30 sec rest between trials. On Day 2, the same protocol was used, with 4 refresher trials, a 20-minute break, and then 3 test trials. This 2-day protocol, which is shorter than some other rotarod protocols, is based on other studies of vestibular function (Tung et al., 2014; Jones et al., 2018; Rahman et al., 2022).

DigiGait: Mice were placed on a treadmill-like apparatus with a clear belt and an internal camera, which records the ventral view of a mouse as it runs on the belt. Mice were recorded in a slow (15 cm/s) and fast (25 cm/s) trial, and the belt was cleaned with Clidox-S between mice.

Analysis of gait parameters was based on the quantitative methods in (Fiker et al., 2020). Briefly, in DeepLabCut, bodyparts were labelled for 35-70 frames per mouse for both the slow and fast trials. These labelled frames were used to train a DeepLabCut model in a Google Colab environment, which then applied labels to all frames. We wrote custom Matlab functions to analyze gait parameters from these body part positions based on Fiker et al., 2020.

Analysis

Data analysis was performed using OriginLab (Northampton, MA) and custom MATLAB scripts.

Fitting sensitivity and time course of transduction currents

G-X curves. Peak transduction currents were the greatest absolute difference between the baseline and step current. Current was converted to conductance (G) using a reversal potential of +2.6 mV (Kros et al., 1992). Sigmoidal dependence of G-X curves was fit with a first-order (Eq. 1) or second-order Boltzmann equation (Eq. 2).

$$G(X) = G_{min} + \frac{G_{max}}{1 + e^{\frac{X_{half} - X}{k}}} \qquad (3.1)$$

$$G(X) = G_{min} + \frac{G_{max}}{1 + (\exp\frac{X_1 - X}{k_1}) * (1 + \exp\frac{X_2 - X}{k_2})} \qquad (3.2)$$

X_1 is the first order midpoint, k_1 is the first order slope factor, inversely related to curve steepness at the midpoint, X_2 is the second order midpoint, and k_2 is the second order slope factor.

Adaptation time course. Adaptation of transduction currents were fit with Eq. 2.

$$I(t) = I_{SS} + A_f * \exp\left(-\frac{t}{\tau_f}\right) + A_s * \exp\left(-\frac{t}{\tau_s}\right) \qquad (3.3)$$

I_{SS} is steady-state current, A_f and A_s are amplitudes of fast and slow adaptation, and τ_f and τ_s are time constants of fast and slow adaptation, respectively.

Lowpass filter. The AC component of responses to sinusoidal bundle displacement were determined with a custom peak-finding MATLAB script, and then divided by the bundle displacement to calculate gain with units of pA/μm or mV/μm. To characterize tuning, gain was normalized to the greatest response at all frequencies measured. Normalized gain as a function of frequency was then fit with a one-pole lowpass filter (Peterson & Heil, 2020).

$$G(f) = \frac{1}{(1 + \left(\frac{f}{f_{LP}}\right)^{2n})^{1/2}} \qquad (3.4)$$

f_{LP} is the lowpass corner frequency and n is the order of the filter, which varied between 0.5 and 1. Phase shift was fit as a function of frequency with Eq. 5, where a is the steepness of the phase-frequency relation and b is the baseline phase.

$$\varphi(f) = -a * \arctan\left(\frac{f}{f_{LP}}\right) + b \qquad (3.5)$$

Statistics

We give means ± SEM for normally-distributed data, and otherwise, median and range. Data normality was assessed with the Shapiro-Wilk test for n<50 and the Kolmogorov-Smirnov test for n>50. To assess homogeneity of variance we used Levene's test. With homogeneous variance, we used one-way ANOVA for genotype with the posthoc Tukey's test. When variance was non-homogeneous, we used one-way Welch ANOVA with the posthoc Games-Howell test. For data that were not normally distributed, we used the non-parametric one-way Kruskal-Wallis ANOVA

(KWA) with posthoc Dunn's test. Effect size is Hedge's g (g). For age dependence, we used partial correlation coefficients controlling for genotype and zone. Statistical groups may have different median ages, but all have overlapping age ranges. In figures, asterisks represent p-value ranges as follows: *, $p<0.05$; **, $p<0.01$; ***, $p<0.001$; ****, $p<0.0001$.

Acknowledgements

This study was supported by NIH grant R01 DC012347 to RAE, NSF Graduate Research Fellowship to HRM, UChicago Quad Summer Undergraduate Research Award (ES), 1U01-NS111695 (KEC), and NIH K12-GM123914 (BMV).

Author Contributions

HRM and RAE designed electrophysiological experiments and analyzed data; HRM executed electrophysiological experiments; OLR executed nonquantal transmission experiments; HRM and DS analyzed behavioral data; DS and ES executed behavioral experiments; HRM and RAE wrote the paper. BMV designed, executed, and analyzed VOR; KC designed VOR.

CHAPTER 4

LOW ELECTRICAL RESISTANCE OF TYPE I HAIR CELLS PRODUCES ARTIFACTS IN MECHANOTRANSDUCTION MEASUREMENTS

4.1 ABSTRACT

Investigating type I *vs*. type II hair cell physiology can reveal meaningful differences in synaptic transmission, hair cell regeneration, and hair bundle mechanics. However, the large, low-voltage-activated conductance ($g_{K,L}$) can confound accurate measurements of physiological properties in type I hair cells. In the presence of $g_{K,L}$, very low input resistance can cause significant voltage-clamp errors. Here, we examine how $g_{K,L}$ introduced an artifact into whole-cell recordings of mechanotransduction in type I hair cells.

In cells with $g_{K,L}$, transduction currents often had creep: a rounded, slow onset (10-90% rise time >0.5 ms) not seen in type II hair cells (rise time <0.5 ms). Slow rise times were corrected when $g_{K,L}$ channels were closed or eliminated with hyperpolarization, pharmacology, or genetic knockout. Slow rise times were also corrected by aggressive series resistance compensation. Computational modeling of a realistic voltage-clamp circuit showed that $g_{K,L}$ was sufficient to introduce a creep in recorded mechanotransduction.

$g_{K,L}$'s low input resistance elongated the apparent rise times of recorded mechanotransduction current. Investigations in mechanotransduction in type I hair cells should minimize this artifact by reducing series resistance, using cesium-based internal solutions, hyperpolarizing below $g_{K,L}$'s activation range, blocking $g_{K,L}$ with 4-AP, and using faster voltage clamp settings.

4.2 INTRODUCTION

Vestibular hair cells transduce head motions into receptor potentials that are strongly shaped by large outwardly rectifying K^+ conductances according to cell type. In type I hair cells, the large, low-voltage-activated K^+ conductance, $g_{K,L}$, reduces input resistance (R_{in}) to 50 MΩ. Low R_{in} can cause artifacts in recordings in whole-cell voltage clamp mode, especially when series resistance (R_S) is high. In voltage-clamp, the amplifier injects current to keep the cell at the command voltage. Voltage clamp is ideal when $R_{in} >> R_S$ because injected current flows down the path of least resistance. However, when R_{in} approaches R_S (~10 MΩ in our experiments), voltage clamp is no longer ideal, and artifacts arise.

We became concerned about these artifacts when we recorded abnormal mechanotransduction currents in type I hair cells. Type I hair cells are particularly challenging to patch because the calyx must be brushed aside to expose the hair cell membrane to the pipette, and the residues of synaptic proteins lingering on the hair cell membrane slow down and attenuate the process of forming a gigaseal between the pipette glass and the phospholipids. After breakthrough is achieved, R_{in} is typically too low to estimate capacitance and series resistance. $g_{K,L}$ must be deactivated by hyperpolarizing below –90 mV, and then capacitance and series resistance can be estimated and compensated for.

These difficulties have led mechanotransduction in type I hair cells to be relatively understudied compared to type II hair cells, as recently noted by others (Caprara & Peng, 2022). Here, we document how experimenters should take extra precautions to minimize timing artifacts when recording mechanotransduction in type I hair cells.

4.3 RESULTS

We recorded from type I and II hair cells from the extrastriolar utricles of mice between postnatal day (P) 7 and P60. Hair bundles were displaced by a stiff probe with steps. Drugs were delivered with an apical pipette.

Head motion-induced bundle deflections can be mimcked *in vitro* with stiff probe deflection of hair bundles. A single hair bundle is displaced in its preferred direction while a patch electrode has whole-cell access to the hair cell body. In **Figure 4.1**, inward transduction currents flowed when step displacements opened mechanotransduction channels at the tips of the stereocilia that make up the hair bundle.

In several mature type I hair cells, these mechanically evoked inward currents had a rounded tip (**Fig. 4.1A**) and a 10-90 % rise time >0.5 ms. In contrast, type II hair cells had sharp adaptation

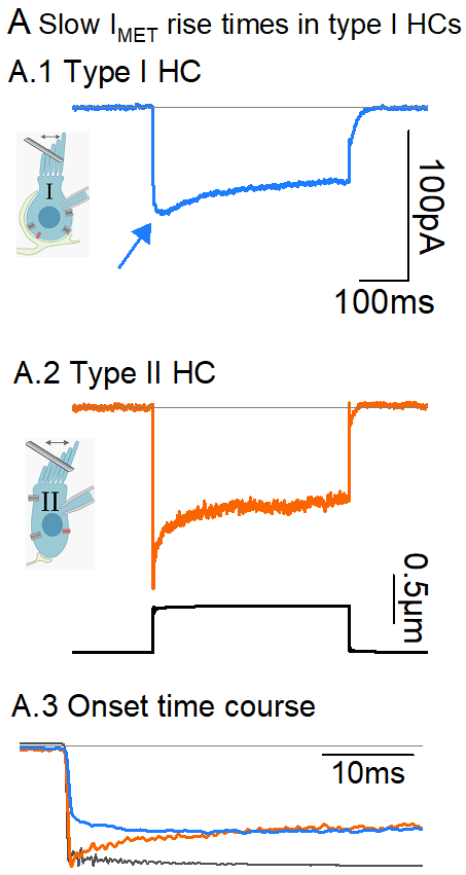

Figure 4.1. Stiff probe displacement of hair bundles evoked I_{MET} with slow rise times in type I but not type II hair cells. (**A**) Transduction current (I_{MET}) had a 10-90% rise time of 2.7 ms in a type I HC (**A.1**, arrow points to rounded onset) and 0.4 ms in a type II HC (**A.2**, arrow points to adaptation that follows sharp onset). Holding potential –84 mV. Step to 0.45 µm. (**A.3**) Overlaid and normalized stimuli and responses emphasize difference in response speed at the beginning of the step.

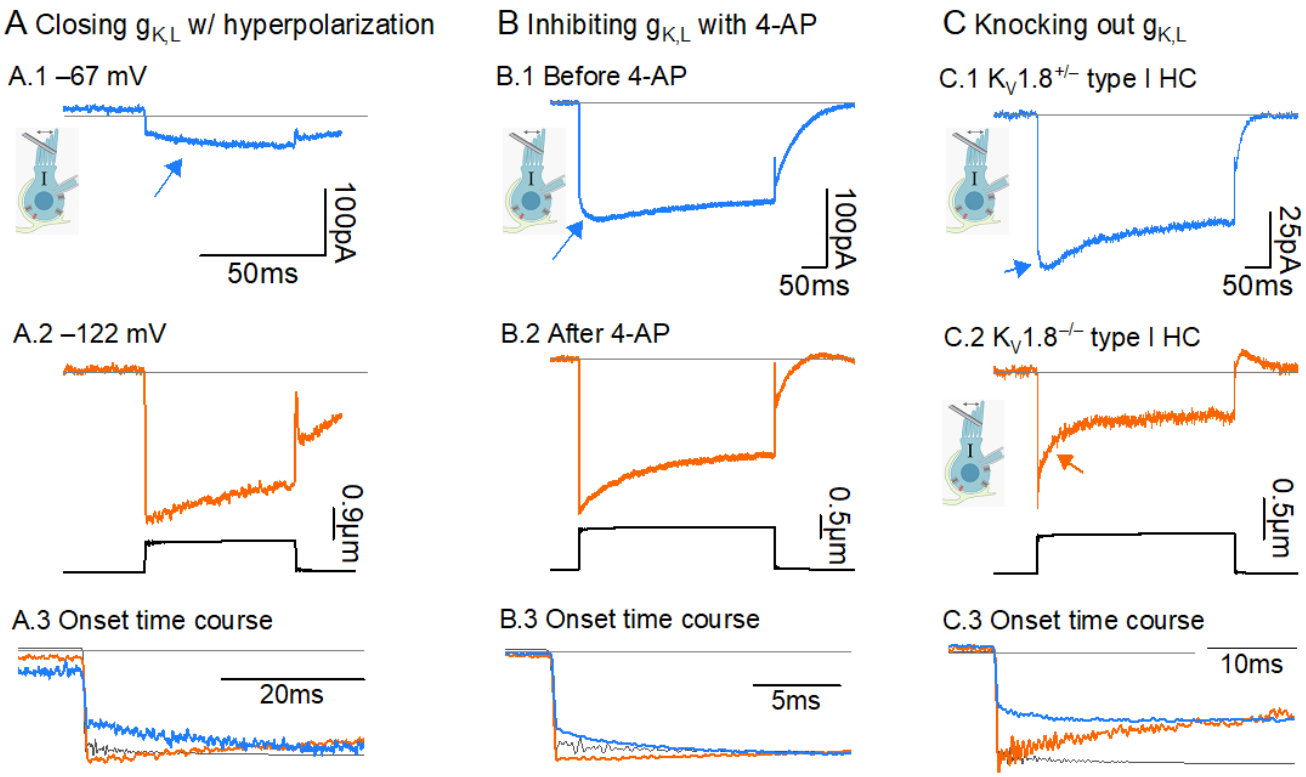

Figure 4.2. Closing or eliminating $g_{K,L}$ restored fast rise times in type I HCs. (**A**) I_{MET} rise times were reduced by closing $g_{K,L}$ channels by hyperpolarizing below their activation threshold. In a type I HC, I_{MET} rise time was 14.9 ms at –67 mV (**A.1**) and decreased to 0.6 at –122 mV (**A.2**), after $g_{K,L}$ channels had been deactivated. Step to 0.91 µm. (**A.3**) Overlaid and normalized stimuli and responses emphasize difference in response speed at the beginning of the step. (**B**) I_{MET} rise times were reduced by inhibiting $g_{K,L}$ channels with 5 mM 4-AP. In a type I HC, I_{MET} rise time was X before 4-AP (**B.1**) and decreased to Y after 4-AP (**B.2**). Holding potential –74 mV. Step to 0.95 µm. (**B.3**) Overlaid and normalized stimuli and responses emphasize difference in response speed at the beginning of the step. (**C**) I_{MET} rise times were smaller in $K_V1.8^{-/-}$ type I hair cells, which lack $g_{K,L}$ (X ms, **C.1**), than in $K_V1.8^{+/-}$ type I hair cells (X ms, **C.2**). Holding potential –84 mV. Step to 0.45 µm. (**B.3**) Overlaid and normalized stimuli and responses emphasize difference in response speed at the beginning of the step.

(**Fig. 4.1A.1**) and rise times <0.5 ms. It was initially unclear whether slow rise times indicated a true difference in the mechanotransduction complex in type I hair cells. The next step was determining if these slow rise times were an artifact arising from the type I hair cells' low R_{in}. We reduced R_{in} by closing or eliminating $g_{K,L}$ using three different methods. Hyperpolarizing the cell to deactivate $g_{K,L}$ decreased the rise time of I_{MET} (**Fig. 4.2A**), which represented the artifact being

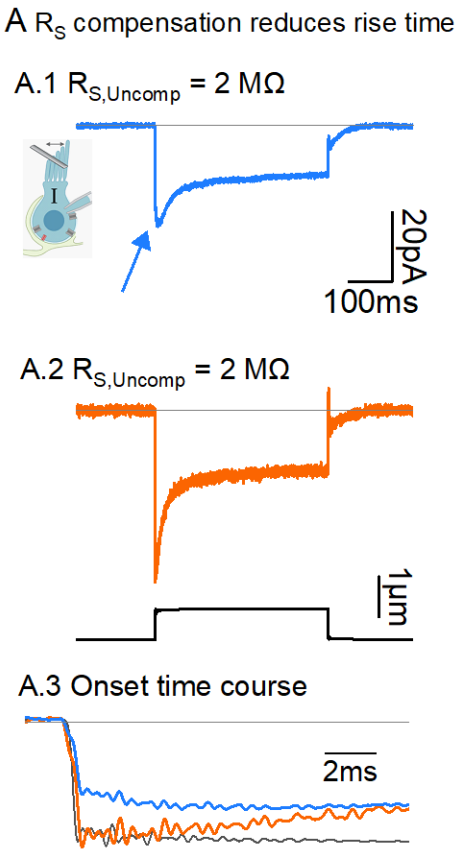

Figure 4.3. Series resistance compensation corrected slow rise times. A type I HC (220108-2456-03 P23 LES, 6pF) had 10 MΩ series resistance (R_S). (**A.1**) At 0% R_S compensation, rounding was present (arrow points to rounded onset). 10-90% rise time was 2.3 ms. **(A.2)** At 80% R_S compensation, rounding was absent (arrow points to adaptation that follows sharp onset). 10-90% rise time was 0.4 ms. *Bottom:*. Holding potential –84 mV. Step to 0.78 µm. (**A.3**) Overlaid and normalized stimuli and responses emphasize difference in response speed at the beginning of the step

corrected. The critical range of hyperpolarization coincided with the activation range of $g_{K,L}$. Reducing $g_{K,L}$ by other means—pharmacology (**Fig. 4.2B**) and knockout (**Fig. 4.2C**)—also eliminated rounding and shortened rise times to more normal values.

We altered series resistance compensation to determine if the presence of open $g_{K,L}$ channels interacted with low-quality voltage-clamp. Rounding was most evident and rise times longest when there was no compensation (**Fig. 4.3A.1**). Increasing compensation to 80% eliminated rounding and shortened rise times (**Fig. 4.2A.2**).

Evidence suggested that low R_{in} and high $R_{S,Uncomp}$ were necessary for slow rise times. We next explored the mechanism. Transducer channels open after displacement, allowing positive ions to enter the cell. Under ideal voltage clamp conditions, the amplifier injects an equal and opposite current into the cell to keep net voltage change at zero. However, the amplifier cannot achieve this instantly. The cell manages to depolarize a blip, and open $g_{K,L}$ channels immediately pass outward

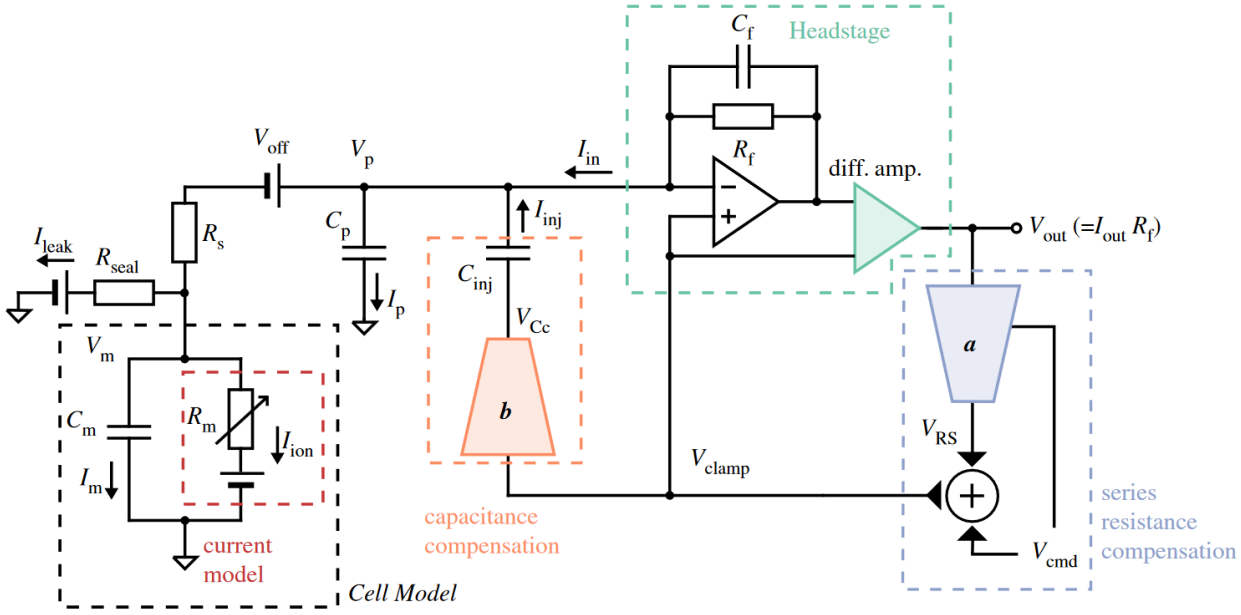

Figure 4.4. A realistic voltage-clamp circuit. Experimental factors that can introduce artifacts include voltage offset (V_{off}), series resistance (R_S) between the pipette electrode and cell, cell capacitance (C_m), pipette (parasitic) capacitance (C_p), and leakage current (I_{leak}). A typical amplifier has circuits (*a, b*) to compensate for these artifacts. See Table S4.1 for a description of each component. Adapted from Lei et al., 2020.

current. Then, the amplifier slowly wrestles back control, and the rate at which the ampifier re-clamps the voltage depends on several electrical and biological parameters.

The recorded trace on the oscilloscope registers a total current equal to inward (negative) I_{MET} *plus* outward (positive) $I_{K,L}$. Total current is initially inward (–) because $I_{MET} > I_{K,L}$, and subsequently creeps more negative as the amplifier clamps the voltage and minimizes the outward current escaping through $I_{K,L}$(+). Creep inflates rise times.

Simulations in a voltage-clamp equivalent circuit quantitatively confirmed this explanation. We modified the realistic voltage-clamp model from Lei et al., 2020, to run in MATLAB (**Fig. 4.4**). **Figure 4.5** includes two simulations with R_S = 10 MΩ, C_m = 5 pF, and compensation at 80%., Without $g_{K,L}$, displacement-evoked current had rapid rise times (*simulation*, <0.1 ms; *experimental*, 0.2-0.4 ms). The addition of $g_{K,L}$ caused currents to creep (**Fig. 4.5B**) and rise times

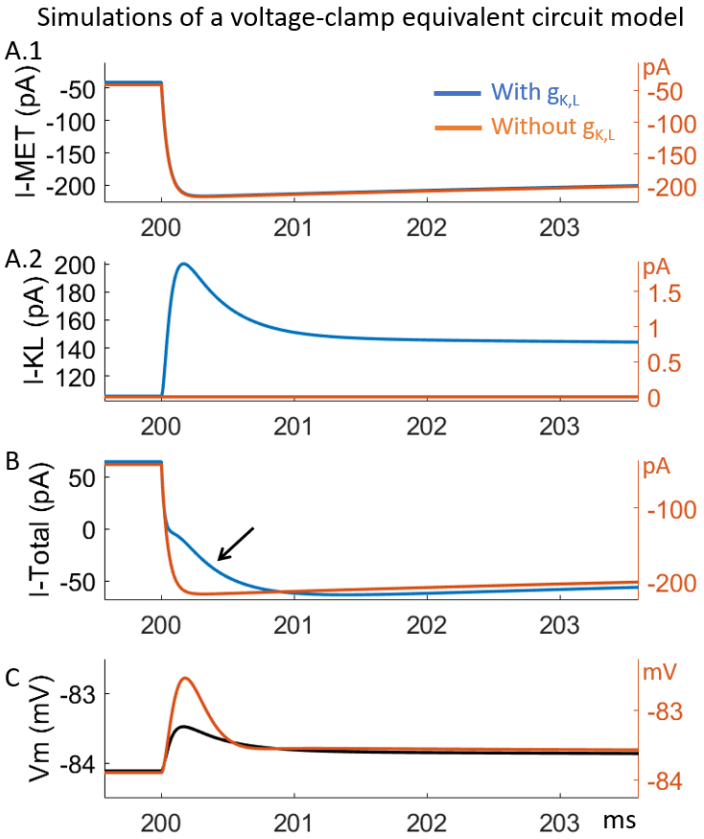

Figure 4.5. Simulated $g_{K,L}$ introduces creep to apparent recorded I_{MET}. I-MET (**A.1**) and I-KL (**A.2**) are summed (**B**) to show current recorded during a whole-cell patch clamp experiment. Arrow points to creep: the slower, two-phase onset of I-Total in the presence of $g_{K,L}$. 10-90% rise time was 0.6 ms with $g_{K,L}$ and 0.1 ms without $g_{K,L}$. (**C**) V_m from the model. Model parameters are in Tables S4.1 and S4.2.

to lengthen (*simulation*, 0.6-0.9 ms; *experimental*, 0.4-15 ms). Simulation rise times were faster than experimental rise times because simulations did not lowpass filter the displacement stimulus.

4.4 DISCUSSION

This investigation has shown that low R_{in} and high $R_{S,Uncomp}$ present real challenges to accurately measuring mechanotransduction in type I hair cells. Others have taken the approach of using large pipettes to minimize R_S (Spaiardi et al., 2017). The most effective and flexible solution is blocking $g_{K,L}$ with 4-AP, which has not been reported to interact with the mechanotransduction complex.

Table 4.1. I_{MET} rise time summary. Experimental stimulation had a 10-90% rise time of 0.27 ms.

Condition	Holding Potential (mV)	R_S (MΩ)	% Compensation	10-90% rise time (ms)
Experimental				
Type I HC 210527-8644-03	–84	32	0	2.7
Type II HC 210625-01	–84	9.3	38	0.4
Type I HC before 4-AP *211208-2379-02*	–76	9.8	0	6.5
Type I HC after 4-AP *211208-2379-02*	–75	9.8	0	0.24
Type I HC 211117-2366-03	–122	11	0	0.6
Type I HC 211117-2366-03	–67	11	0	14.9
$K_V1.8^{-/-}$ Type I HC *210518-1587-02*	–84	13	40	0.3
Type I HC 220108-2456-03	–84	10	0	2.3
Type I HC 220108-2456-03	–84	10	80	0.4
Simulated				
$g_{K,L}$	–84	10	0	0.6
$g_{K,L}$	–84	10	80	
No $g_{K,L}$	–84	10	0	<0.1
No $g_{K,L}$	–84	10	80	<0.1
$g_{K,L}$	–60	10	0	0.9

4.5 MATERIALS AND METHODS

Preparation

All procedures for handling animals followed the NIH Guide for the Care and Use of Laboratory Animals and were approved by the Institutional Animal Care and Use Committees of the University of Chicago and the University of Illinois Chicago. Most mice belonged to a transgenic line with a knockout allele of *Kcna10* (referred to here as $K_V1.8^{-/-}$). Our breeding colony was established with a generous gift of such animals from Sherry M. Jones and Thomas Friedman. These animals are described in their paper (Lee et al., 2013). Briefly, the Texas A&M Institute for Genomic Medicine generated the line on a C57BL/6;129SvEv mixed background by replacing Exon 3 of the *Kcna10* gene with an IRES-bGeo/Purocassette. Mice in our colony were raised on a 12:12h light-dark cycle with access to food and water *ad libitum*.

Semi-intact utricles were prepared from ~150 male and ~120 female mice, postnatal days (P) 6-60, for same-day recording. Hair cell transduction data were pooled across sexes.

Preparation, stimulation, and recording methods followed our previously described methods for the mouse utricle (Vollrath and Eatock, 2003). Mice were anesthetized through isoflurane inhalation. After decapitation, each hemisphere was bathed in ice-cold, oxygenated Liebowitz-15 (L15) media. The temporal bone was removed, the labyrinth was cut to isolate the utricle, and the nerve was cut close to the utricle. The utricle was treated with proteinase XXIV (100 mg/mL, ~10 mins, 22ºC) to facilitate removal of the otoconia and attached gel layer and mounted beneath two glass rods affixed at one end to a coverslip.

Electrophysiology

We used the HEKA Multiclamp EPC10 with Patchmaster acquisition software, filtered by the integrated HEKA filters: a 6-pole Bessel filter at 10 kHz and a second 4-pole Bessel filter at 5 kHz, and sampled at 10-100 kHz. Recording electrodes were pulled (PC-100, Narishige) from soda lime glass (King's Precision Glass R-6) wrapped in paraffin to reduce pipette capacitance. Internal solution contained (in mM) 135 KCl, 0.5 $MgCl_2$, 3 MgATP, 5 HEPES, 5 EGTA, 0.1 $CaCl_2$, 0.1 Na-cAMP, 0.1 LiGTP, 5 $Na_2CreatinePO_4$ adjusted to pH 7.25 and ~280 mmol/kg by adding ~30 mM KOH. External solution was Liebowitz-15 media supplemented with 10 mM HEPES (pH 7.40, 310 ± 10 mmol/kg). Recording temperature was 22-25ºC. Pipette capacitance and membrane capacitance transients were subtracted online with Patchmaster software. Series resistance (8-12 MΩ) was measured after rupture and compensated 60-80% with the amplifier, to final values of ~2 MΩ. Potentials are corrected for remaining (uncompensated) series resistance and liquid junction potential of ~+4 mV, calculated with LJPCalc software (Marino et al., 2014).

Transduction

Hair bundles were deflected by a stiff probe (borosilicate, tip width <1 μm) attached to a piezoelectric planar bimorph. Driving voltage to the bimorph was lowpass filtered by an 8-pole Bessel filter (Frequency Devices Active Tunable Filter Model 900) at a corner frequency of 1000 Hz for a probe with a resonant frequency of 2250 Hz. Probe time course was monitored offline by projecting the probe image onto the edge of a photodiode (PIN-6D). At the end of each experiment, steady-state probe tip distance per driving voltage was measured using a slow step stimulus, camera, and DIC illumination. In figures, probe stimuli traces are photodiode signals scaled to the known voltage sensitivity of the probe.

We evoked I_{MET} and V_{RP} by displacing (X) the hair bundle along its sensitive axis with a stiff glass rod placed behind and approximately halfway up the hair bundle. Resting probe position was selected to be 10-20% of the operating range of the bundle, evoking 16±2 % (n=38) of maximum I_{MET} [$100*(I_{X=0} - I_{min})/(I_{max} - I_{min})$]. We expect this imposed resting position to be slightly higher than natural resting position because we pushed the bundle slightly to ensure mechanical coupling with the probe. To record I_{MET}, most HCs were held at –84 mV to increase driving force on IMET and reduce noise from voltage-gated channels. Some type I HCs were held negative to –84 mV to fully deactivate $g_{K,L}$, which is so large as to degrade the voltage clamp.

Pharmacology

Drug-containing solutions were locally with BASI Bee Hive syringes at a final flow rate of 20 µL/min and a dead time of ~30 s. Global bath perfusion was paused during drug perfusion and recording, and only one cell was used per utricle. Aliquots of test agents in solution were prepared, stored at –20°C, and thawed and added to external solution on the recording day (fampridine/4-AP, Sigma-Aldrich).

Analysis

Data analysis was performed using OriginLab (Northampton, MA) and custom MATLAB scripts.

CHAPTER 5

CONCLUSION

A core question driving this project was a longstanding mystery about hair cell K channels and their role in type I hair cell-calyx transmission and vestibular circuit function. Such features that speed up vestibular receptor potentials and non-quantal afferent transmission may have helped stabilize locomotion as tetrapods moved from water to land.

In Chapter 2, we found that $K_V1.8$ was necessary not just for $g_{K,L}$ but also for fast-inactivating and delayed rectifier currents in the more ancient type II HCs, which activate positive to resting potential. These findings contributed significantly to the field's understanding of the molecular identity of K channels in mammalian vestibular hair cells. Two outstanding questions remain about how $K_V1.8$ channels generate the biophysical properties of $g_{K,L}$ and g_A.

In type I HCs, $g_{K,L}$ has a V_{half} (–84 mV) that is far negative to the V_{half} of $K_V1.8$ in other cell types (–25 mV to 0 mV, Lang et al., 2000; Dierich et al., 2020; Ranjan et al., 2019; Martin et al., 2024). Factors that could account for the difference in activation voltage include the high density of $g_{K,L}$, interaction with the calyx environment, modulation by accessory subunits, and RNA editing.

In type II HCs, g_A has rapid N-type inactivation not seen in $K_V1.8$ homomers in heterologous systems (Lang et al., 2000; Dierich et al., 2020; Ranjan et al., 2019). $K_V1.8$-containing g_A may acquire rapid inactivation by heteromerization with the $K_V1.4$, $K_V\beta1$, and $K_V\beta2$ subunits that are also expressed in type II hair cells. These findings highlight type I and II hair cells as good models to explore the complex regulatory network that governs ion channels to achieve different physiological profiles.

In Chapter 3, we showed that higher input resistance in $K_V1.8^{-/-}$ hair cells decreased the frequency range of head motion detection, to the effect of impairing performance on challenging balance tasks that require rapid and linear compensation for head motions.

We tested the hypothesis that $g_{K,L}$ augments nonquantal transmission and found that $g_{K,L}$ knockout reduced nonquantal transmission at very high frequencies and reduced phase at all frequencies tested. Further comparison of nonquantal transmission in control and knockout conditions should be higher throughput, such as with *in vivo* sharp electrode recordings from the vestibular ganglion (Holt et al., 2007), maintain spatiotemporal resolution, and capture population effects, such as with microscopy (K^+, Ca^{2+}, and voltage imaging).

There is a growing awareness in the vestibular field that nonquantal transmission is a more robust driver of vestibular function than quantal transmission. Pharmacological and genetic inhibition of glutamatergic transmission shows that quantal transmission is not necessary for some vestibular outputs (Mukhopadhyay et al., 2023; Pastras et al., 2023), consistent with how rarely we observe quantal transmission in mature utricle preps. Our understanding of amniote vestibular function would be incomplete without a description of nonquantal transmission.

We have established $K_V1.8^{-/-}$ mice as the first model of "perturbation of nonquantal transmission". Complementary models would modify calyx height, which computational models predict is the most essential factor enabling nonquantal transmission (Govindaraju et al., 2023). Calyces are abnormally loose in the absence of the septate junction protein Caspr (Sousa et al., 2009), presenting a promising complementary model, but vestibular phenotypes in $Caspr^{-/-}$ mice are unknown because pups develop severe ataxia and die before P20 (Bhat et al., 2001). Our interpretation of the $K_V1.8^{-/-}$ phenotype is also complicated by the null mutation's effect on type II HCs and thus quantal transmission. Future research should develop type I HC-specific

knockouts of $K_V1.8$ and Caspr to avoid systemic side effects and isolate the phenotypes that depend on nonquantal transmission.

In Chapter 4, we investigated how low electrical resistance in type I hair cells makes it difficult to accurately record mechanotransduction. This artifact can be minimized by reducing both $g_{K,L}$ and uncompensated series resistance to achieve a more ideal voltage clamp. Other hair cell researchers may not have considered these concerns because other hair cells do not have such low input resistance. With this information, they will be better equipped to collect clean data on type I hair cell physiology.

In this work, we investigated a novel cell type that may have arisen to meet the challenges of life on land by speeding up head motion detection and enabling fast balance reflexes. We followed this trail from molecular assembly of ion channel complexes to sensory physiology to downstream behaviors. These projects highlighted for me how productive it can be to examine the cell type expansions that occur during critical points in evolution.

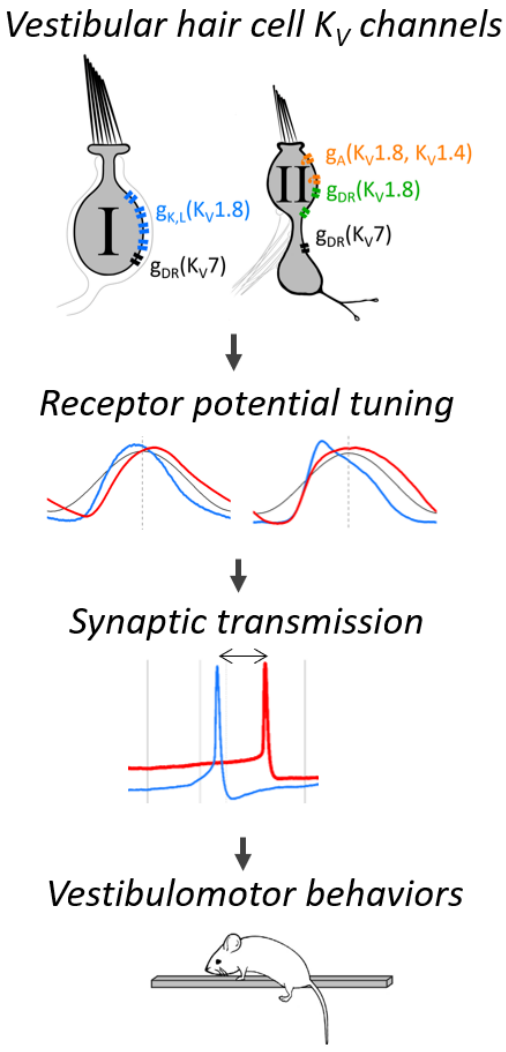

Figure 5.1. Graphical summary.

REFERENCES

Alexander SPH et al. (2019) The Concise Guide to Pharmacology 2019/20: Ion channels. Br J Pharmacol 176

Al-Sabi A, Kaza S, Le Berre M, O'Hara L, Bodeker M, Wang J, Dolly JO (2011) Position-dependent attenuation by Kv1.6 of N-type inactivation of Kv1.4-containing channels. Biochem J 438:389–396.

Ashmore JF (1983) Frequency tuning in a frog vestibular organ. Nature 304:536–538.

Bao H, Wong WH, Goldberg JM, Eatock RA (2003) Voltage-Gated Calcium Channel Currents in Type I and Type II Hair Cells Isolated From the Rat Crista. J Neurophysiol 90:155–164.

Baukrowitz T, Yellen G (1995) Modulation of K+ current by frequency and external [K+]: A tale of two inactivation mechanisms. Neuron 15:951–960.

Behrend O, Schwark C, Kunihiro T, Strupp M (1997) Cyclic GMP inhibits and shifts the activation curve of the delayed rectifier (I(K1)) of type I mammalian vestibular hair cells. NeuroReport 8:2687–2690.

Bhat MA, Rios JC, Lu Y, Garcia-Fresco GP, Ching W, St Martin M, Li J, Einheber S, Chesler M, Rosenbluth J, Salzer JL, Bellen HJ (2001) Axonglia interactions and the domain organization of myelinated axons requires neurexin IV/Caspr/Paranodin. Neuron 30:369 –383

Brown DA, Selyanko AA, Hadley JK, Tatulian L (2002) Some Pharmacological Properties Of Neural KCNQ Channels. Neurophysiology 34:91–94.

Brugeaud A, Gaboyard-Niay S, Puel J-L, Chabbert C (2006) Hypergravity affects the developmental expression of voltage-gated sodium current in utricular hair cells. NeuroReport 17:1697–1701.

Brugeaud A, Travo C, Dememes D, Lenoir M, Llorens J, Puel J-L, Chabbert C (2007) Control of Hair Cell Excitability by Vestibular Primary Sensory Neurons. J Neurosci 27:3503–3511**.**

Caprara GA, Peng AW (2022) Mechanotransduction in mammalian sensory hair cells. Molecular and Cellular Neuroscience 120:103706.

Carlisle FA, Steel KP, Lewis MA (2012) Specific expression of Kcna10, Pxn and Odf2 in the organ of Corti. Gene Expression Patterns 12:172–179.

Chen JWY, Eatock RA (2000) Major Potassium Conductance in Type I Hair Cells from Rat Semicircular Canals: Characterization and Modulation by Nitric Oxide. J Neurophysiol 84:139–151.

Contini D, Holstein GR, Art JJ (2020) Synaptic cleft microenvironment influences potassium permeation and synaptic transmission in hair cells surrounded by calyx afferents in the turtle. J Physiol 598:853–889.

Contini D, Price SD, Art JJ (2017) Accumulation of K^+ in the synaptic cleft modulates activity by influencing both vestibular hair cell and calyx afferent in the turtle: K^+ modulation of synaptic transmission between hair cell and afferent. J Physiol 595:777–803.

Contini D, Zampini V, Tavazzani E, Magistretti J, Russo G, Prigioni I, Masetto S (2012) Intercellular K^+ accumulation depolarizes Type I vestibular hair cells and their associated afferent nerve calyx. Neuroscience 227:232–246.

Correia MJ, Lang DG (1990) An electrophysiological comparison of solitary type I and type II vestibular hair cells. Neuroscience Letters 116:106–111.

Correia MJ, Ricci AJ, Rennie KJ (1996) Filtering Properties of Vestibular Hair Cells: An Update. Ann NY Acad Sci 781:138–149.

Correia MJ, Weng T, Prusak D, Wood TG (2008) Kvβ1.1 Associates with Kv1.4 in Chinese Hamster Ovary Cells and Pigeon Type II Vestibular Hair Cells and Enhances the Amplitude, Inactivation and Negatively Shifts the Steady-State Inactivation Range. Neuroscience 152:809–820.

Crawford AC, Fettiplace R (1981) An electrical tuning mechanism in turtle cochlear hair cells. J Physiol 312:377–412.

Curthoys IS, Vulovic V, Burgess AM, Sokolic L, Goonetilleke SC (2016) The response of guinea pig primary utricular and saccular irregular neurons to bone-conducted vibration (BCV) and air-conducted sound (ACS). Hear Res 331:131–143.

Desai SS, Zeh C, Lysakowski A (2005) Comparative Morphology of Rodent Vestibular Periphery. I. Saccular and Utricular Maculae. J Neurophysiol 93:251–266.

Dierich M, Altoè A, Koppelmann J, Evers S, Renigunta V, Schäfer MK, Naumann R, Verhulst S, Oliver D, Leitner MG (2020) Optimized Tuning of Auditory Inner Hair Cells to Encode Complex Sound through Synergistic Activity of Six Independent K+ Current Entities. Cell Reports 32:107869.

Dwenger MM, Raph SM, Baba SP, Moore JB, Nystoriak MA (2022) Diversification of Potassium Currents in Excitable Cells via Kvβ Proteins. Cells 11:2230.

Eatock RA, Songer JE (2011) Vestibular Hair Cells and Afferents: Two Channels for Head Motion Signals. Annu Rev Neurosci 34:501–534.

Enthoven L, Dalm S, de Kloet ER, Oitzl MS (2004) Swim posture of mice does not affect performance in the water maze. Brain Research 1003:36–41.

Erickson T, Nicolson T (2015) Identification of sensory hair-cell transcripts by thiouracil-tagging in zebrafish. BMC Genomics 16:842.

Fettiplace R (1987) Electrical tuning of hair cells in the inner ear. TINS 10:5.

Fiker R, Kim LH, Molina LA, Chomiak T, Whelan PJ (2020) Visual Gait Lab: A user-friendly approach to gait analysis. Journal of Neuroscience Methods 341:108775.

Géléoc GS, Risner J, Holt JR (2004) Developmental Acquisition of Voltage-Dependent Conductances and Sensory Signaling in Hair Cells of the Embryonic Mouse Inner Ear. J Neurosci 24:11148–11159.

Goldberg JM (2000) Afferent diversity and the organization of central vestibular pathways. Exp Brain Res 130:277–297.

González-Garrido A, Pujol R, López-Ramírez O, Finkbeiner C, Eatock RA, Stone JS (2021) The Differentiation Status of Hair Cells That Regenerate Naturally in the Vestibular Inner Ear of the Adult Mouse. J Neurosci 41:7779–7796.

Govindaraju AC, Quraishi IH, Lysakowski A, Eatock RA, Raphael RM (2023) Nonquantal transmission at the vestibular hair cell–calyx synapse: K_{LV} currents modulate fast electrical and slow K^+ potentials. Proc Natl Acad Sci USA 120:e2207466120.

Gulley A, Bagger-Sjöbäck D (1979) Freeze-fracture studies on the synapse between the type I hair cells and the calyceal terminal in the guinea-pig vestibular system. J Neurocytol 8:591–603.

Hager ER, Hoekstra HE (2021) Tail Length Evolution in Deer Mice: Linking Morphology, Behavior, and Function. Integrative and Comparative Biology 61:385–397.

Heinemann SH, Rettig J, Graack HR, Pongs O (1996) Functional characterization of Kv channel beta-subunits from rat brain. J Physiol 493:625–633.

Holt JR, Stauffer EA, Abraham D, Geleoc GSG (2007) Dominant-Negative Inhibition of M-Like Potassium Conductances in Hair Cells of the Mouse Inner Ear. J Neurosci 27:8940–8951.

Hudspeth AJ, Lewis RS (1988) A model for electrical resonance and frequency tuning in saccular hair cells of the bull-frog, Rana catesbeiana. J Physiol 400:275–297.

Hurley KM, Gaboyard S, Zhong M, Price SD, Wooltorton JRA, Lysakowski A, Eatock RA (2006) M-Like K^+ Currents in Type I Hair Cells and Calyx Afferent Endings of the Developing Rat Utricle. Journal of Neuroscience 26:10253–10269.

Imbrici P, D'Adamo MC, Kullmann DM, Pessia M (2006) Episodic ataxia type 1 mutations in the *KCNA1* gene impair the fast inactivation properties of the human potassium channels Kv1.4-1.1/Kvβ1.1 and Kv1.4-1.1/Kvβ1.2. Eur J Neurosci 24:3073–3083.

Jamali M, Chacron MJ, Cullen KE (2016) Self-motion evokes precise spike timing in the primate vestibular system. Nat Commun 7:13229.

Jan TA, Eltawil Y, Ling AH, Chen L, Ellwanger DC, Heller S, Cheng AG (2021) Spatiotemporal dynamics of inner ear sensory and non-sensory cells revealed by single-cell transcriptomics. Cell Reports 36:109358.

Jensen HS, Grunnet M, Olesen S-P (2007) Inactivation as a New Regulatory Mechanism for Neuronal Kv7 Channels. Biophys J 92:2747–2756.

Jones SM, Erway LC, Johnson KR, Yu H, Jones TA (2004) Gravity receptor function in mice with graded otoconial deficiencies. Hearing Research 191:34–40.

Jones SM, Vijayakumar S, Dow SA, Holt JC, Jordan PM, Luebke AE (2018) Loss of α-Calcitonin Gene-Related Peptide (αCGRP) Reduces Otolith Activation Timing Dynamics and Impairs Balance. Front Mol Neurosci 11:289.

Jones TA, Jones SM, Vijayakumar S, Brugeaud A, Bothwell M, Chabbert C (2011) The adequate stimulus for mammalian linear vestibular evoked potentials (VsEPs). Hear Res 280:133–140.

Keine C (2024) HEKA Patchmaster Importer. Available at: https://github.com/ChristianKeine/HEKA_Patchmaster_Importer.

Kharkovets T, Hardelin J-P, Safieddine S, Schweizer M, El-Amraoui A, Petit C, Jentsch TJ (2000) KCNQ4, a K^+ channel mutated in a form of dominant deafness, is expressed in the inner ear and the central auditory pathway. Proc Natl Acad Sci USA 97:4333–4338.

Kole MJ, Qian J, Waase MP, Klassen TL, Chen TT, Augustine GJ, Noebels JL (2015) Selective Loss of Presynaptic Potassium Channel Clusters at the Cerebellar Basket Cell Terminal Pinceau in Adam11 Mutants Reveals Their Role in Ephaptic Control of Purkinje Cell Firing. J Neurosci 35:11433–11444.

Kros CJ, Rüsch A, Richardson GP (1992) Mechano-electrical transducer currents in hair cells of the cultured neonatal mouse cochlea. Proc R Soc Lond B 249:185–193.

Kubisch C, Schroeder BC, Friedrich T, Lütjohann B, El-Amraoui A, Marlin S, Petit C, Jentsch TJ (1999) KCNQ4, a Novel Potassium Channel Expressed in Sensory Outer Hair Cells, Is Mutated in Dominant Deafness. Cell 96:437–446.

Lang R, Lee G, Liu W, Tian S, Rafi H, Orias M, Segal AS, Desir GV (2000) KCNA10: A novel ion channel functionally related to both voltage-gated potassium and CNG cation channels. American Journal of Physiology - Renal Physiology 278.

Lee SI, Conrad T, Jones SM, Lagziel A, Starost MF, Belyantseva IA, Friedman TB, Morell RJ (2013) A null mutation of mouse Kcna10 causes significant vestibular and mild hearing dysfunction. Hear Res 300:1–9.

Lei CL, Clerx M, Whittaker DG, Gavaghan DJ, de Boer TP, Mirams GR (2020) Accounting for variability in ion current recordings using a mathematical model of artefacts in voltage-clamp experiments. Phil Trans R Soc 378:20190348.

Lewis ER (1988) Tuning in the bullfrog ear. Biophysical Journal 53:441–447.

Liberman MC, Gao J, He DZZ, Wu X, Jia S, Zuo J (2002) Prestin is required for electromotility of the outer hair cell and for the cochlear amplifier. Nature 419:300–304.

Lim R, Kindig AE, Donne SW, Callister RJ, Brichta AM (2011) Potassium accumulation between type I hair cells and calyx terminals in mouse crista. Exp Brain Res 210:607–621.

Liu H, Chen L, Giffen KP, Stringham ST, Li Y, Judge PD, Beisel KW, He DZZ (2018) Cell-Specific Transcriptome Analysis Shows That Adult Pillar and Deiters' Cells Express Genes Encoding Machinery for Specializations of Cochlear Hair Cells. Front Mol Neurosci 11:356.

López-Barneo J, Hoshi T, Heinemann SH, Aldrich RW (1993) Effects of external cations and mutations in the pore region on C-type inactivation of Shaker potassium channels. Recept Channels 1:61–71.

Lysakowski A, Gaboyard-Niay S, Calin-Jageman I, Chatlani S, Price SD, Eatock RA (2011) Molecular Microdomains in a Sensory Terminal, the Vestibular Calyx Ending. J Neurosci 31:10101–10114.

Lysakowski A, Goldberg JM (2004) Morphophysiology of the vestibular periphery. In: The Vestibular System, pp 57–152 Springer Hearing and Auditory Research. Springer New York. Available at: https://doi.org/10.1007/0-387-21567-0_3.

Manca M, Yen P, Spaiardi P, Russo G, Giunta R, Johnson SL, Marcotti W, Masetto S (2021) Current Response in $Ca_V1.3^{-/-}$ Mouse Vestibular and Cochlear Hair Cells. *Front Neurosci* 15:749483. doi:10.3389/fnins.2021.749483

Marino M, Misuri L, Brogioli D (2014) A new open source software for the calculation of the liquid junction potential between two solutions according to the stationary Nernst-Planck equation. Available at: http://arxiv.org/abs/1403.3640 [Accessed October 23, 2023].

Martin HR, Lysakowski A, Eatock RA (2024) The potassium channel subunit $K_V1.8$ (Kcna10) is essential for the distinctive outwardly rectifying conductances of type I and II vestibular hair cells. eLife 13:RP94342

McInturff S, Burns JC, Kelley MW (2018) Characterization of spatial and temporal development of Type I and Type II hair cells in the mouse utricle using new cell-type-specific markers. Biol Open 7:bio038083.

Meredith FL, Rennie KJ (2016) Channeling your inner ear potassium: K+ channels in vestibular hair cells. Hear Res 338:40–51.

Mukhopadhyay M, Yang-Hood A, Ohlemiller KK, Xiao M, Warchol M, Lee SJ, Seal R, Rubio ME, Rutherford M, Pangrsic T (2023) Glutamatergic Quantal Transmission in Peripheral Vestibular Function. Association for Research in Otolaryngology Midwinter Meeting Conference Poster.

Ono K, Keller J, López Ramírez O, González Garrido A, Zobeiri OA, Chang HHV, Vijayakumar S, Ayiotis A, Duester G, Della Santina CC, Jones SM, Cullen KE, Eatock RA, Wu DK (2020) Retinoic acid degradation shapes zonal development of vestibular organs and sensitivity to transient linear accelerations. Nat Commun 11:63.

Orvis J et al. (2021) gEAR: Gene Expression Analysis Resource portal for community-driven, multi-omic data exploration. Nat Methods 18:843–844.

Pastras CJ, Curthoys IS, Asadnia M, McAlpine D, Rabbitt RD, Brown DJ (2023) Evidence that ultrafast non-quantal transmission underlies synchronized vestibular action potential generation. J Neurosci:JN-RM-1417-23.

Perez-Flores MC, Lee JH, Park S, Zhang X-D, Sihn C-R, Ledford HA, Wang W, Kim HJ, Timofeyev V, Yarov-Yarovoy V, Chiamvimonvat N, Rabbitt RD, Yamoah EN (2020) Cooperativity of K_v 7.4 channels confers ultrafast electromechanical sensitivity and emergent properties in cochlear outer hair cells. Sci Adv 6:eaba1104.

Peterson AJ, Heil P (2020) Phase Locking of Auditory Nerve Fibers: The Role of Lowpass Filtering by Hair Cells. J Neurosci 40:4700–4714.

Pujol R, Pickett SB, Nguyen TB, Stone JS (2014) Large basolateral processes on type II hair cells are novel processing units in mammalian vestibular organs: Basolateral Processes of Type II Hair Cells. J Comp Neurol 522:3141–3159.

Rahman SM, Hauser C, Faucher S, Fine E, Jonnala R, Duzgezen V, Strangio B, Liang B, Luebke AE (2022) Role of Calcitonin Gene-Related Peptide (CGRP) in Auditory, Static, and Dynamic Imbalance Behaviors: Implications for Vestibular Migraine. bioRXIV Available at: http://biorxiv.org/lookup/doi/10.1101/2022.06.03.494764 [Accessed July 19, 2022].

Ramanathan K, Fuchs PA (2002) Modeling Hair Cell Tuning by Expression Gradients of Potassium Channel. Biophys J 82:64–72.

Ranjan R, Logette E, Marani M, Herzog M, Tache V, Scantamburlo E, Buchilier V, Markram H (2019) A Kinetic Map of the Homomeric Voltage-Gated Potassium Channel (Kv) Family. Front Cell Neurosci 13:358.

Rennie KJ, Correia MJ (1994) Potassium currents in mammalian and avian isolated type I semicircular canal hair cells. J Neurophysiol 71:317–329.

Rennie KJ, Weng T, Correia MJ (2001) Effects of KCNQ channel blockers on K^+ currents in vestibular hair cells. Am J Physiol Cell Physiol 280:C473–C480.

Ricci AJ, Rennie KJ, Correia MJ (1996) The delayed rectifier, IKI, is the major conductance in type I vestibular hair cells across vestibular end organs. Pflüg Arch Eur J Physiol 432:34–42.

Rothman JS, Manis PB (2003) Kinetic Analyses of Three Distinct Potassium Conductances in Ventral Cochlear Nucleus Neurons. J Neurophysiol 89:3083–3096.

Rüsch A, Eatock RA (1996a) A delayed rectifier conductance in type I hair cells of the mouse utricle. J Neurophysiol 76:995–1004.

Rüsch A, Eatock RA (1996b) Voltage Responses of Mouse Utricular Hair Cells to Injected Currents. Ann NY Acad Sci 781:71–84.

Rüsch A, Lysakowski A, Eatock RA (1998) Postnatal development of type I and type II hair cells in the mouse utricle: Acquisition of voltage-gated conductances and differentiated morphology. Journal of Neuroscience 18:7487–7501.

Scheffer DI, Shen J, Corey DP, Chen Z-Y (2015) Gene Expression by Mouse Inner Ear Hair Cells during Development. J Neurosci 35:6366–6380.

Scheibinger M, Janesick A, Benkafadar N, Ellwanger DC, Jan TA, Heller S (2022) Cell-type identity of the avian utricle. Cell Reports 40:111432.

Schroeder BC, Hechenberger M, Weinreich F, Kubisch C, Jentsch TJ (2000) KCNQ5, a Novel Potassium Channel Broadly Expressed in Brain, Mediates M-type Currents. Journal of Biological Chemistry 275:24089–24095.

Schweizer FE, Savin D, Luu C, Sultemeier DR, Hoffman LF (2009) Distribution of high-conductance calcium-activated potassium channels in rat vestibular epithelia. J Comp Neurol 517:134–145.

Smith GT, Proffitt MR, Smith AR, Rusch DB (2018) Genes linked to species diversity in a sexually dimorphic communication signal in electric fish. J Comp Physiol A 204:93–112.

Songer JE, Eatock RA (2013) Tuning and Timing in Mammalian Type I Hair Cells and Calyceal Synapses. J Neurosci 33:3706–3724.

Sousa AD, Andrade LR, Salles FT, Pillai AM, Buttermore ED, Bhat MA, Kachar B (2009) The Septate Junction Protein Caspr Is Required for Structural Support and Retention of KCNQ4 at Calyceal Synapses of Vestibular Hair Cells. J Neurosci 29:3103–3108.

Spaiardi P, Tavazzani E, Manca M, Milesi V, Russo G, Prigioni I, Marcotti W, Magistretti J, Masetto S (2017) An allosteric gating model recapitulates the biophysical properties of $I_{K,L}$ expressed in mouse vestibular type I hair cells: Allosteric gating of $I_{K,L}$. J Physiol 595:6735–6750.

Spaiardi P, Tavazzani E, Manca M, Russo G, Prigioni I, Biella G, Giunta R, Johnson SL, Marcotti W, Masetto S (2020) K+ Accumulation and Clearance in the Calyx Synaptic Cleft of Type I Mouse Vestibular Hair Cells. Neuroscience 426:69–86.

Spitzmaul G, Tolosa L, Winkelman BHJ, Heidenreich M, Frens MA, Chabbert C, de Zeeuw CI, Jentsch TJ (2013) Vestibular Role of KCNQ4 and KCNQ5 K+ Channels Revealed by Mouse Models*. Journal of Biological Chemistry 288:9334–9344.

Stone JS, Pujol R, Nguyen TB, Cox BC (2021) The Transcription Factor Sox2 Is Required to Maintain the Cell Type-Specific Properties and Innervation of Type II Vestibular Hair Cells in Adult Mice. J Neurosci 41:6217–6233.

Stühmer W, Ruppersberg JP, Schröter KH, Sakmann B, Stocker M, Giese KP, Perschke A, Baumann A, Pongs O (1989) Molecular basis of functional diversity of voltage-gated potassium channels in mammalian brain. EMBO J 8:3235–3244.

Takahashi S, Sun W, Zhou Y, Homma K, Kachar B, Cheatham MA, Zheng J (2018) Prestin Contributes to Membrane Compartmentalization and Is Required for Normal Innervation of Outer Hair Cells. Front Cell Neurosci 12:211.

Tanimoto M, Watakabe I, Higashijima S (2022) Tiltable objective microscope visualizes selectivity for head motion direction and dynamics in zebrafish vestibular system. Nat Commun 13:7622.

Tung VWK, Burton TJ, Dababneh E, Quail SL, Camp AJ (2014) Behavioral Assessment of the Aging Mouse Vestibular System. J Vis Exp:51605.

Vollrath MA, Eatock RA (2003) Time course and extent of mechanotransducer adaptation in mouse utricular hair cells: Comparison with frog saccular hair cells. Journal of Neurophysiology 90:2676–2689.

Wang H (1998) KCNQ2 and KCNQ3 Potassium Channel Subunits: Molecular Correlates of the M-Channel. Science 282:1890–1893.

Wersäll J (1956) Studies on the structure and innervation of the sensory epithelium of the cristae ampulares in the guinea pig; a light and electron microscopic investigation. Acta Otolaryngol Suppl 126:1–85.

Wong WH, Hurley KM, Eatock RA (2004) Differences Between the Negatively Activating Potassium Conductances of Mammalian Cochlear and Vestibular Hair Cells. J Assoc Res Otolaryngol 5:270–284.

Xu T, Nie L, Zhang Y, Mo J, Feng W, Wei D, Petrov E, Calisto LE, Kachar B, Beisel KW, Vazquez AE, Yamoah EN (2007) Roles of Alternative Splicing in the Functional Properties of Inner Ear-specific KCNQ4 Channels. J Biol Chem 282:23899–23909.

Yao X (2002) Expression of KCNA10, a Voltage-Gated K Channel, in Glomerular Endothelium and at the Apical Membrane of the Renal Proximal Tubule. Journal of the American Society of Nephrology 13:2831–2839.

Zobeiri OA, Ostrander B, Roat J, Agrawal Y, Cullen KE (2021) Loss of peripheral vestibular input alters the statistics of head movement experienced during natural self-motion. J Physiol 599:2239–2254.

APPENDIX A

SUPPLEMENTAL FIGURES AND TABLES FOR CHAPTER 2

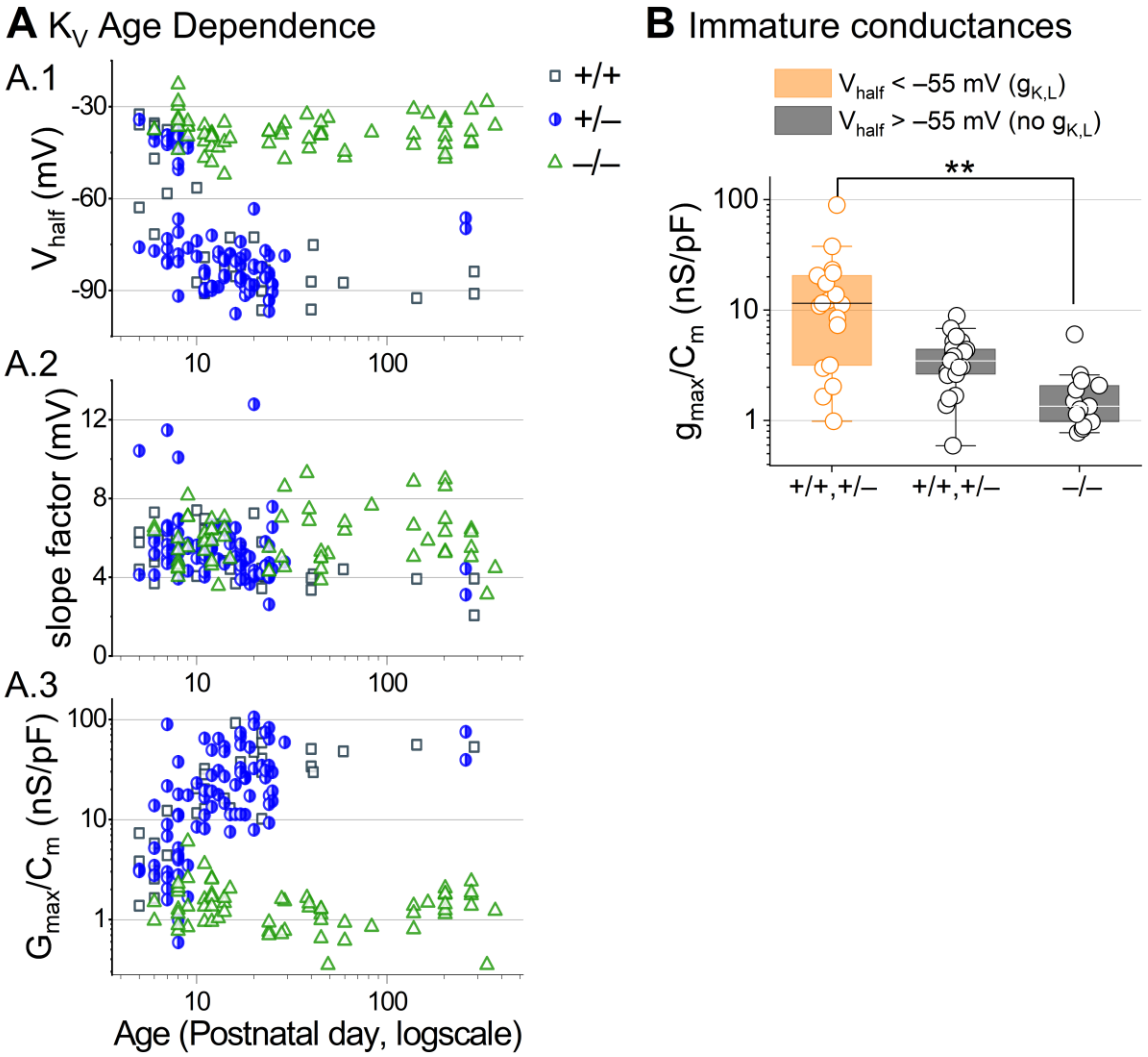

Supplemental Figure S2.1. Developmental changes in type I HC K_V conductances. (**A**) Parameters from Boltzmann fits of tail G-V relations for type I HCs plotted against age. (**B**) Conductance density is similar in young (P5-P10) type I HCs that lack $g_{K,L}$. $g_{K,L}$ is defined here as having a V_{half} negative to –55 mV. $K_V1.8^{+/+,+/-}$ *with* $g_{K,L}$, 17 ± 5 nS/pF (19); $K_V1.8^{+/+,+/-}$ *without* $g_{K,L}$, 3.7 ± 0.4 nS/pF (22); $K_V1.8^{-/-}$, 1.8 ± 0.4 nS/pF (13). $K_V1.8^{+/+,+/-}$ *with* $g_{K,L}$ vs. $K_V1.8^{-/-}$: p = 0.007, KWA, g 1.0.

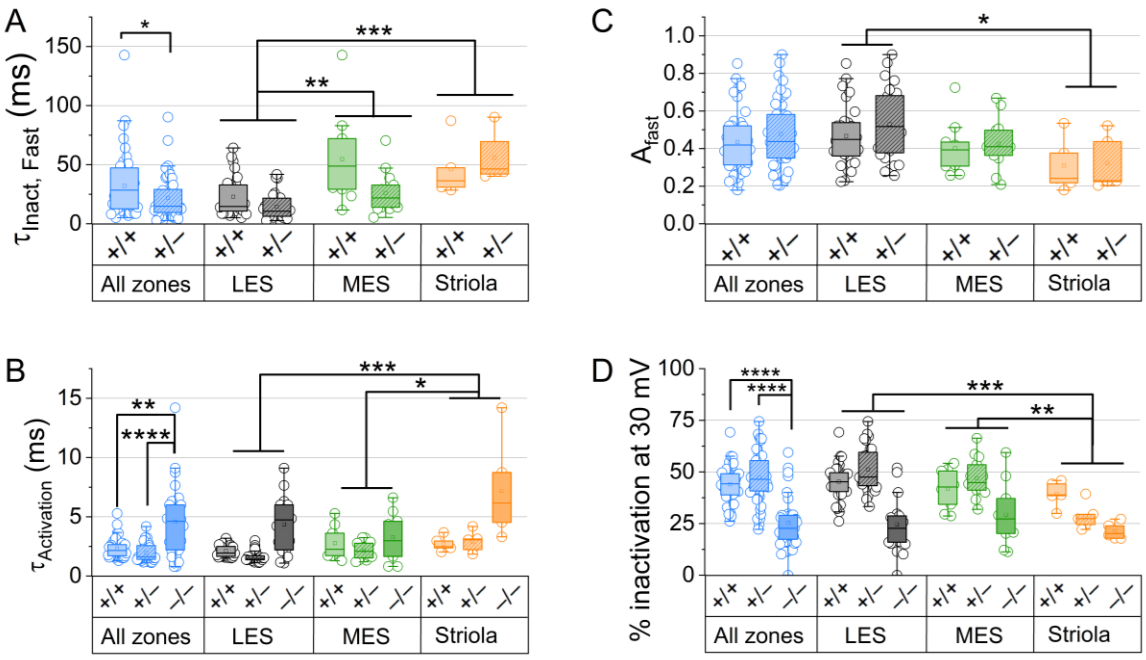

Supplemental Figure S2.2. For type II HCs older than P12, K_V conductance activation and inactivation differed across zones and genotypes.
(**A**) $\tau_{inact,Fast}$ at 30 mV was fastest in LES in $K_V1.8^{+/+}$ and $K_V1.8^{+/-}$ HCs, and faster in $K_V1.8^{+/-}$ than $K_V1.8^{+/+}$ HCs (see Table 2.3 for p-values).
(**B**) Fast inactivation was a larger fraction of the total in LES than striola.
(**C**) τ_{Act} at 30 mV was slower in $K_V1.8^{-/-}$ than $K_V1.8^{+/+}$ and $K_V1.8^{+/-}$, and slower in striola than LES and MES.
(**D**) Percent inactivation at 30 mV was lowest in striola (zone effect), and lowest in $K_V1.8^{-/-}$ HCs (genotype effect).

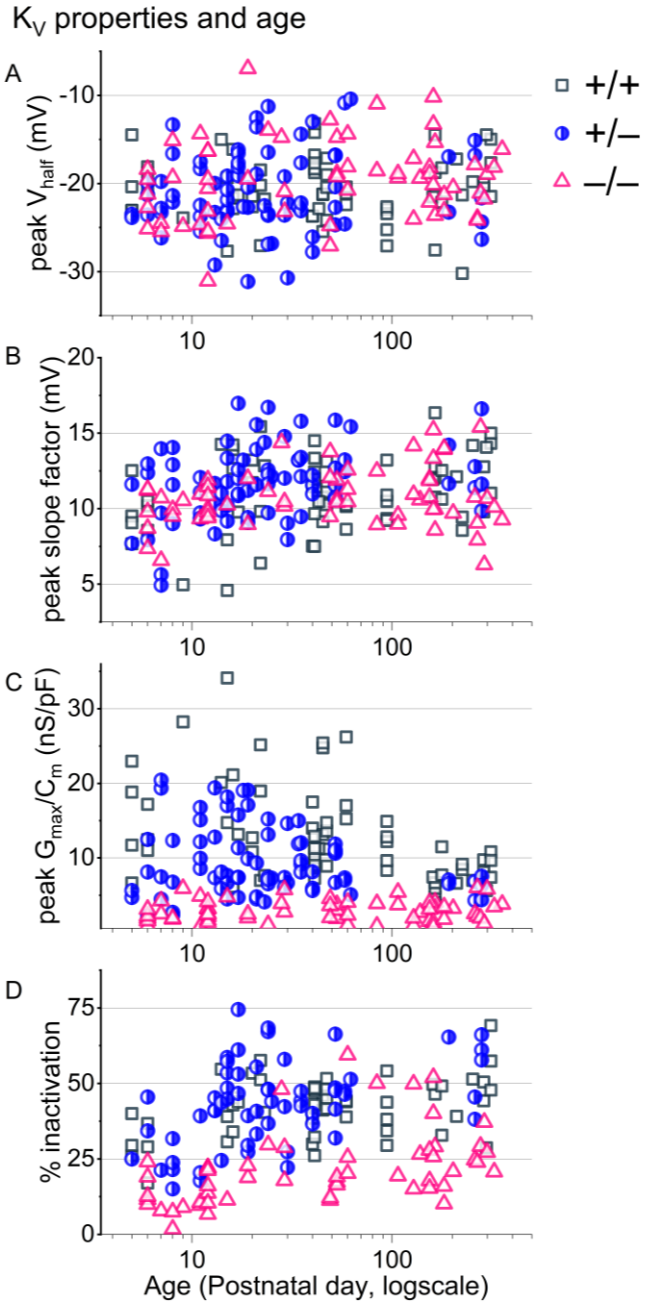

Supplemental Figure S2.3. For type II HCs older than P12, K_V conductances were stable.

(**A-C**) Parameters from Boltzmann fits of peak G-V relations and (**D**) % inactivation at +30 mV plotted against age from all zones. Overlaid curves are smoothing cubic β-splines. Note the seven extrastriolar $K_V1.8^{-/-}$ type II HCs with % inactivation >30%.

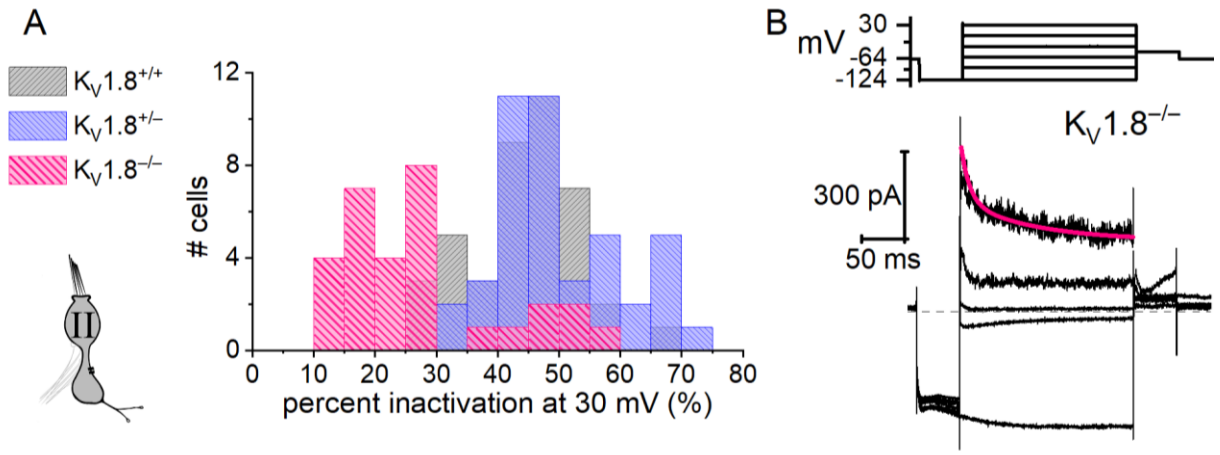

Supplemental Figure S2.4. A minority of extrastriolar $K_V1.8^{-/-}$ type II HCs had a very small fast-inactivating outward rectifier current.

(**A**) All extrastriolar $K_V1.8^{+/+,+/-}$ type II HCs inactivated by >30%. Most mature (>P12) extrastriolar $K_V1.8^{-/-}$ type II HCs inactivated by <30% but some inactivated by >30% (7/30, 23%) because they had fast inactivation (B).

(**B**) Exemplar residual fast inactivation ($\tau_{FastInact}$ = 10 ms at +30 mV). For the 7 cells in this group, $\tau_{FastInact}$ = 30 ± 6 ms, amplitude of fast inactivation = 310 ± 70 pA; activation peak V_{half} = –15 ± 2 mV and slope factor = 12.4 ± 0.9 mV. These parameters are similar to g_A but for the much smaller conductance (one-way ANOVAs).

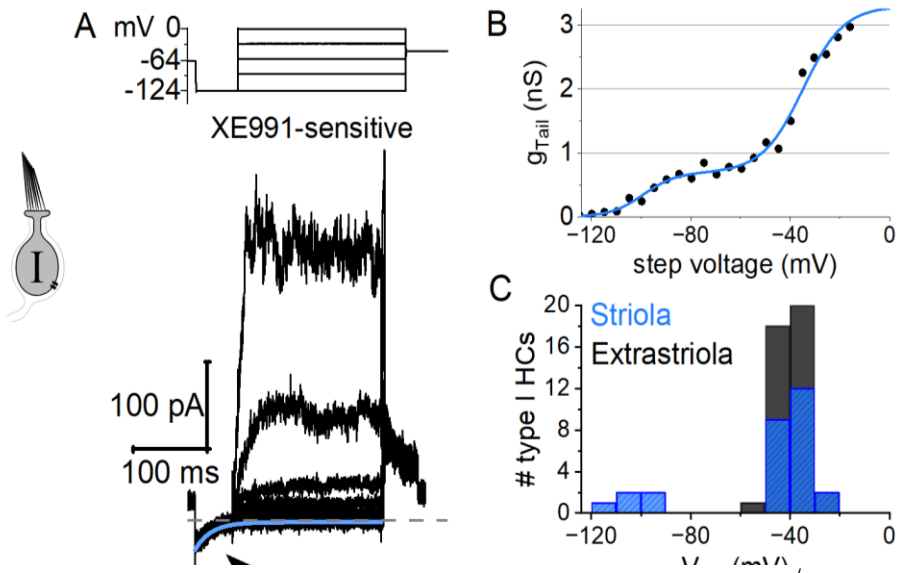

Supplemental Figure S2.5. A minority of striolar $K_V1.8^{-/-}$ type I HCs had a small low-voltage-activated outward rectifier current.

(**A**) Low-voltage-activated current from one cell was isolated by 10 μM XE991 (P39), suggesting it was a K_V7 current. Deactivation of XE991-sensitive current after step from –64 mV to –124 mV *(arrow*) was fit with exponential decay (τ = 21 ms).

(**B**) Tail G-V curve fit with a sum of two Boltzmann equations: $V_{half,1}$ = –102 ± 4 mV (n=5) and $V_{half,2}$ = –41 ± 1 mV. Ages: P11, 39, 202, 202, 202.

(**C**) Bimodal V_{half} distribution was specific to striolar type I HCs. 5/23 (22%; P6-P370) of striolar type I HCs had this low-voltage-activated component, but no extrastriolar type I HCs (0/45; P6-277).

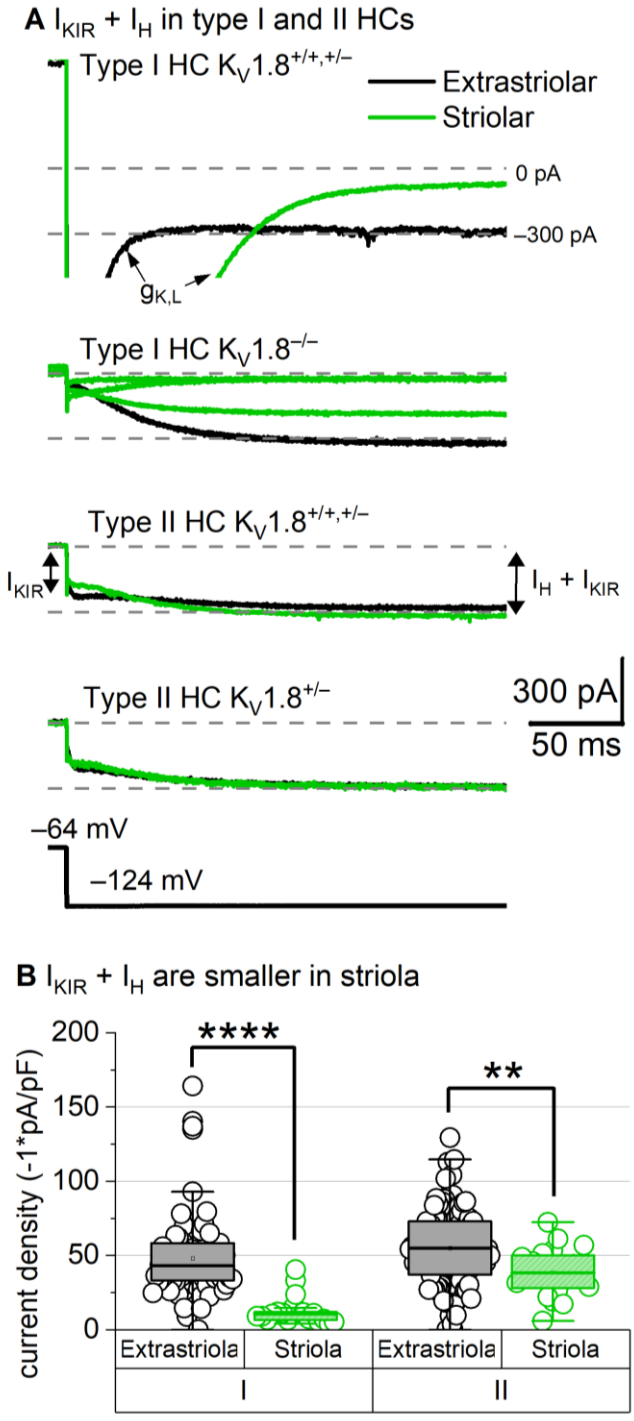

Supplemental Figure S2.6. No difference was detected in H (HCN) and KIR (fast inward rectifier) currents between $K_V1.8^{+/+}$ and $K_V1.8^{-/-}$ hair cells, consistent with a specific involvement of $K_V1.8$ in *Kcna10* expression.

(**A**) Hyperpolarizing voltage steps evoked I_{KIR} and I_{HCN} in $K_V1.8^{+/+,+/-,-/-}$ type I and II HCs. Note the prominent fast activation of I_{KIR} in type II but not type I HCs. Arrows in top panel show deactivation of $g_{K,L}$. I_H and I_{Kir} were measured as inward current after 250 ms at –124 mV.

(**B**) Summed I_{KIR} and I_H density was the same across genotypes but smaller in striola than extrastriola (see Supplemental Table S2.2 for statistics).

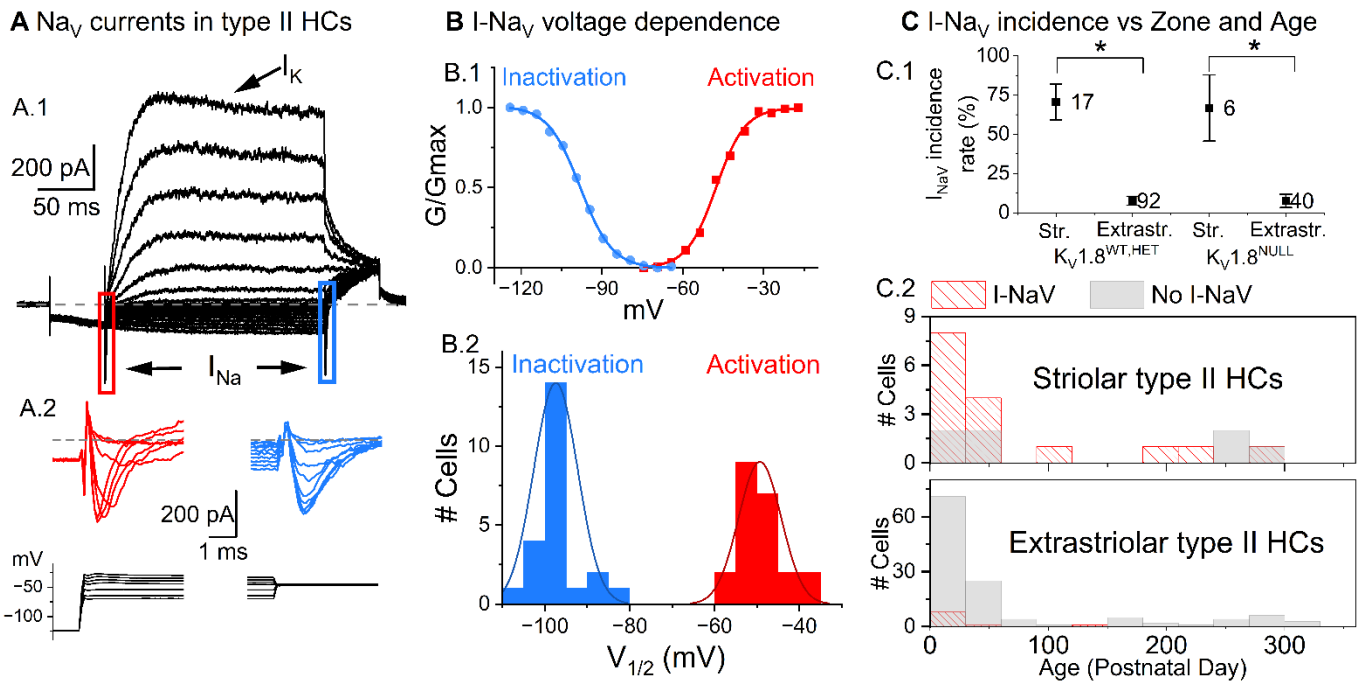

Supplemental Figure S2.7. Regional differences in I_{NaV} in type II HCs.

(**A**) Voltage-clamp recordings from some type II hair cells revealed voltage-gated I_{NaV}, evident as transient inward currents at the beginning of the step and tail potentials. (A.2) Insets correspond to the boxed regions in A.1 showing Na_V activation (red) in response to depolarization from –124 mV to the various step potentials and Na_V inactivation (blue) in response to depolarization from various step potentials to –44 mV. The current's transient nature (it rapidly returned to 0 pA) indicated that it flowed through Na_V channels, not Ca_V channels, which are relatively sustained in HCs (Bao et al., 2003; Manca et al., 2021). The maximal inward current in these two regions provided data points for the GV curves in B.1.

(**B**) The voltage dependence of Na_V activation and inactivation was found by fitting GV points to Eq. 2.1 (exemplars in B.1), with the histogram of V_{half} values in B.2 showing a mean inactivation V_{half} of –97 ± 1 (23) and activation V_{half} of –49 ± 1 (22).

(**C**) Likelihood of observing I_{NaV} in type II HCs of different zones, ages, and genotypes. (C.1) I_{NaV} was more likely to occur in striolar type II HCs (S, 71 ± 9% (24); ES, 8 ± 2% (133); p = 2E-8; g = 2.0), with no detectable effect of genotype ($K_V1.8^{+/+}$, 14 ± 5% (43); $K_V1.8^{+/-}$, 21 ± 5% (67); $K_V1.8^{-/-}$, 17 ± 6% (47); p = 0.5, 0.9, 0.8; power = 0.26). Statistics are from 2-way ANOVA with zone and genotype; and data labels are the number of cells in each group. (C.2) I_{NaV} was more likely in all type II HCs below P20 but persisted in many striolar type II HCs above P20.

Supplemental Table S2.1. *Test of sex differences in hair cell K_V channel data.*

Cell Type	Parameter	Subgroup	Male vs Female posthoc p-value	Test
Type I HC	Tail V_{half}	+/+,+/–	0.0023 ** [a]	Normal, homogeneous variance ANOVA: Genotype (2 levels), Sex (2 levels), Zone (2 levels), Genotype*Sex.
		–/–	0.57	
	Tail S	+/+,+/–	0.98	ANOVA: Genotype (2 levels), Sex (2 levels), Zone (2 levels), Genotype*Sex. Normal, homogeneous variance
		–/–	0.58	
	Tail $g_{Density}$	+/+,+/–	0.999	Normal, nonhomogeneous variance Welch ANOVA: Genotype*Sex
		–/–	0.936	
Type II HC	Peak V_{half}	+/+,+/–	0.95	Normal, homogeneous variance ANOVA: Genotype (2 levels), Sex (2 levels), Zone (2 levels), Genotype*Sex.
		–/–	0.28	
	Peak S	+/+,+/–	0.999	Normal, homogeneous variance ANOVA: Genotype (2 levels), Sex (2 levels), Zone (2 levels), Genotype*Sex.
		–/–	0.97	
	Peak $g_{Density}$	+/+,+/–	0.64	Normal, nonhomogeneous variance Welch ANOVA: Genotype*Sex
		–/–	0.43	
	% inactivation at 30 mV	+/+,+/–	0.98	Normal, homogeneous variance ANOVA: Genotype (2 levels), Sex (2 levels), Zone (2 levels), Genotype*Sex.
		–/–	0.82	

[a] g, 0.9. Male $K_V1.8^{+/+,+/–}$, –85 ± 1 mV (40) vs. Female $K_V1.8^{+/+,+/–}$, –79 ± 2 mV (12)

Supplemental Table S2.2. *Detected zonal but not genotype differences in hair cell I_{KIR} and I_H.*

Cell Type	Zone	I_H + I_{Kir} current density (-1*pA/pF)	$K_v1.8^{+/+,+/–}$ *vs* $K_v1.8^{–/–}$ p-value	ES *vs* Striola p-value	Test
Type I HC	ES Striola	48 ± 3 (78) 13.0 ± 2 (19)	0.3	4E-9 **** [a]	Non-normal, KWA
Type II HC	ES Striola	55 ± 2 (116) 39 ± 4 (20)	0.19 (0.25 power)	0.0058 ** [b]	Normal, homogeneous variance. 2-way ANOVA: Genotype (2 levels), Zone (2 levels)

[a] g 1.4
[b] g 0.6

APPENDIX B

SUPPLEMENTAL FIGURES AND TABLES FOR CHAPTER 3

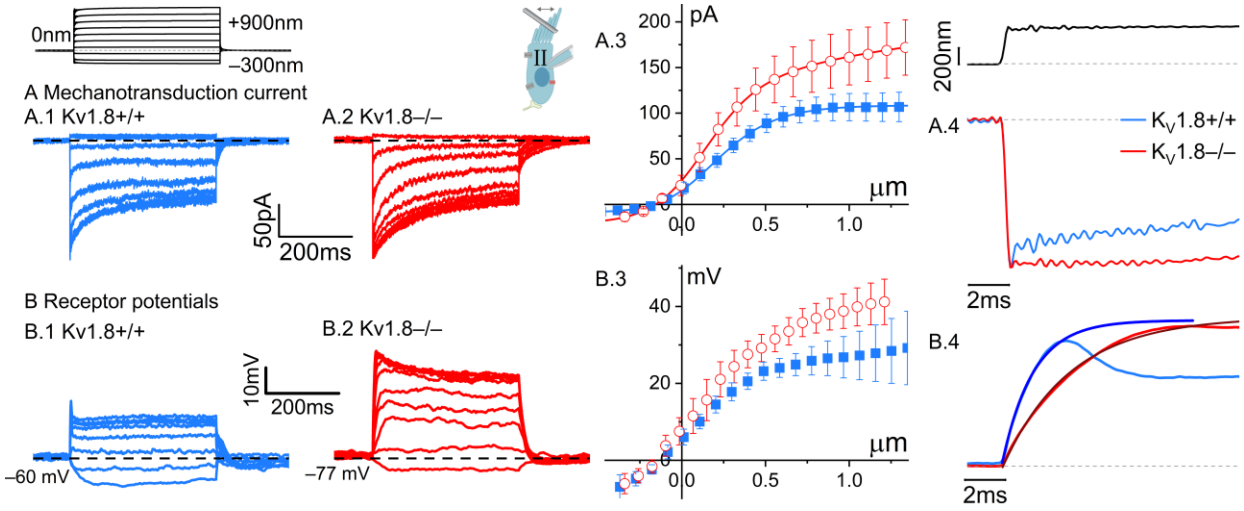

Supplemental Figure S3.1. $K_V1.8^{-/-}$ type II hair cells produced larger but more delayed receptor potentials than $K_V1.8^{+/+,-/-}$ type II HCs. (**A**) Transduction current (I_{MET}) was similar across genotypes. The step stimulus above applies to the entire figure. Exemplar step-evoked transduction current at holding potentials –84 mV. Averages of 3-6 presentations. (**A.3**) Peak $I_{MET}(X)$ relation were averaged across multiple cells and then fit with Eq. 3.1, 3.2. (**A.4**) Onset responses to +0.5 µm displacement were similar. High frequency oscillations are undamped probe resonance.

(**B**) Receptor potentials (V_{RP}) were larger and slower in $K_V1.8^{-/-}$ type I HCs. Exemplar step-evoked receptor potentials are from cells with different V_m. (B.3) Peak $V_{RP}(X)$ were averaged across cells. (B.4) Onset responses from to +0.5 µm displacements show the faster membrane time constant in $K_V1.8^{+/+,-/-}$ type I HCs. Double-exponential fits (Eq. 3.3) are overlaid.

Statistics are in Table 3.1,3.2.

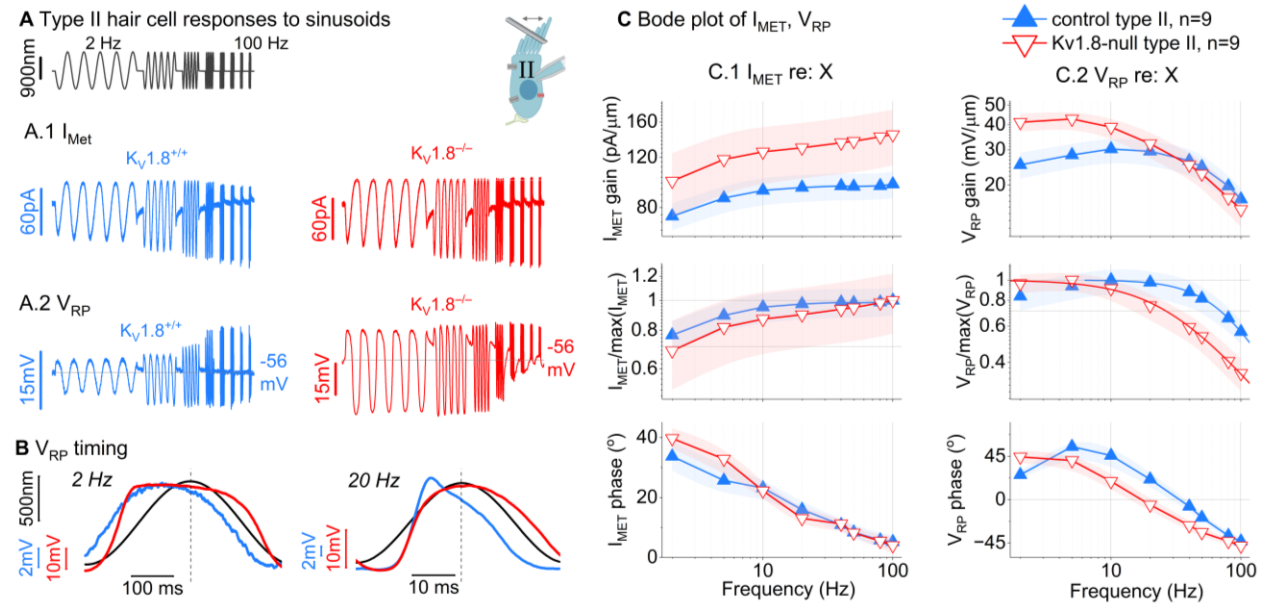

Supplemental Figure S3.2. $K_V1.8$ raises the lowpass corner frequency of receptor potentials in type II HCs. (**A**) I_{MET} and V_{RP} are averages of 6-13 presentations of the sinusoidal stimuli (X) at the top. Baseline potential is indicated to the right of each V_{RP} trace. (**B**) Single V_{RP} sinusoidal cycles are overlaid with the stimulus (grey) to show the phase (timing) advance of the peak response of control relative to $K_V1.8$-null HCs: (**C-D**) Gain and phase of responses referenced to input signals as functions of frequency; mean ± SEM values (see key for n). ***C***, I_{MET} referenced to X : peak-to-peak gain (***C.1,*** actual, ***C.2,*** normalized) and phase (***C.3***). ***D***, V_{RP} referenced to X; peak-to-peak gain (***D.1,*** actual, ***D.2,*** normalized) and phase (***D.3***).

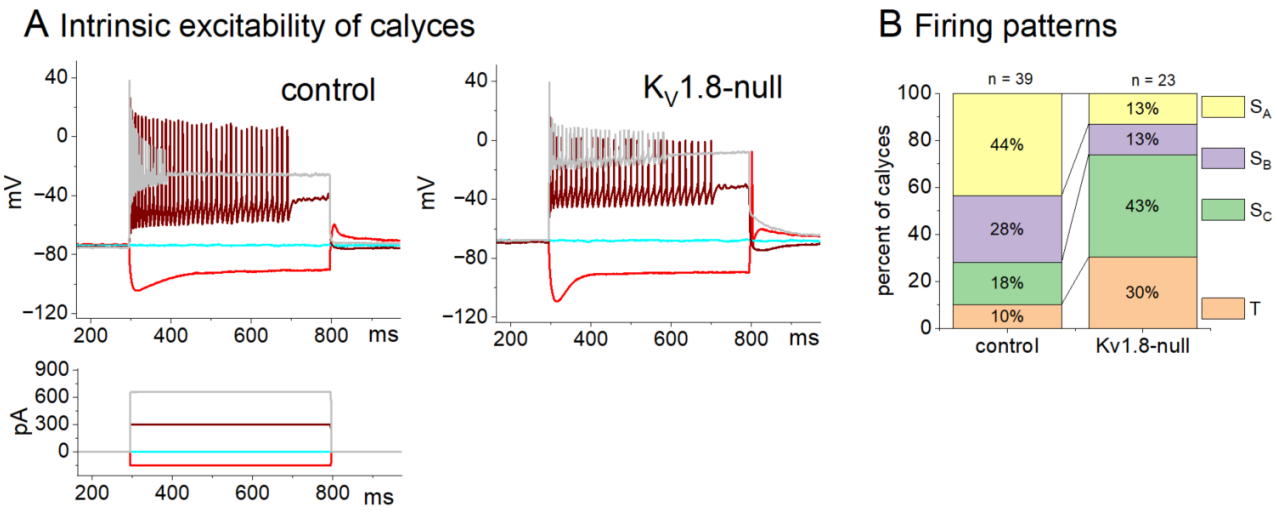

Supplemental Figure S3.3. Currents and excitability of calyces did not differ in control and K_V1.8-null utricles. (**A**) Representative current-clamp records from control and K_V1.8-null extrastriolar calyces. (**B**) The distribution of firing types (Sustained A, B, C, and Transient). Statistics in Suppl. Table S3.1.

Supplemental Table S3.1. Statistics of voltage-dependent currents and excitability in utricular calyces. Mean ± SEM (number of cells). KWA is Kruskal-Wallis ANOVA.

Currents and Excitability								
K_V1.8 Genotype	V_m (mV)	R_{in} (MΩ)	Rheobase (pA)	Sag Ratio	I_H (pA) at –124 mV	K_V g_{max} (nS)	C_m (pF)	Age range (days, median)
+/+,+/–	–69.8 ± 0.7 (39)	290 ± 20 (39)	0.7 ± 0.2 (34)	0.3 ± 0.02 (38)	–490 ± 60 (25)	13 ± 3 (25)	4 ± 1 (27)	8-259 (17)
–/–	–67 ± 1 (21)	240 ± 30 (22)	1.7 ± 0.3 (17)	0.33 ± 0.03 (22)	–620 ± 60 (17)	14 ± 2 (12)	5 ± 1 (23)	12-259 (38)
p-value:	t-test 0.07	KWA 0.3	KWA 0.4	t-test 0.3	KWA 0.07	KWA 0.4	KWA 0.3	
effect size:								
power:	0.45			0.16				

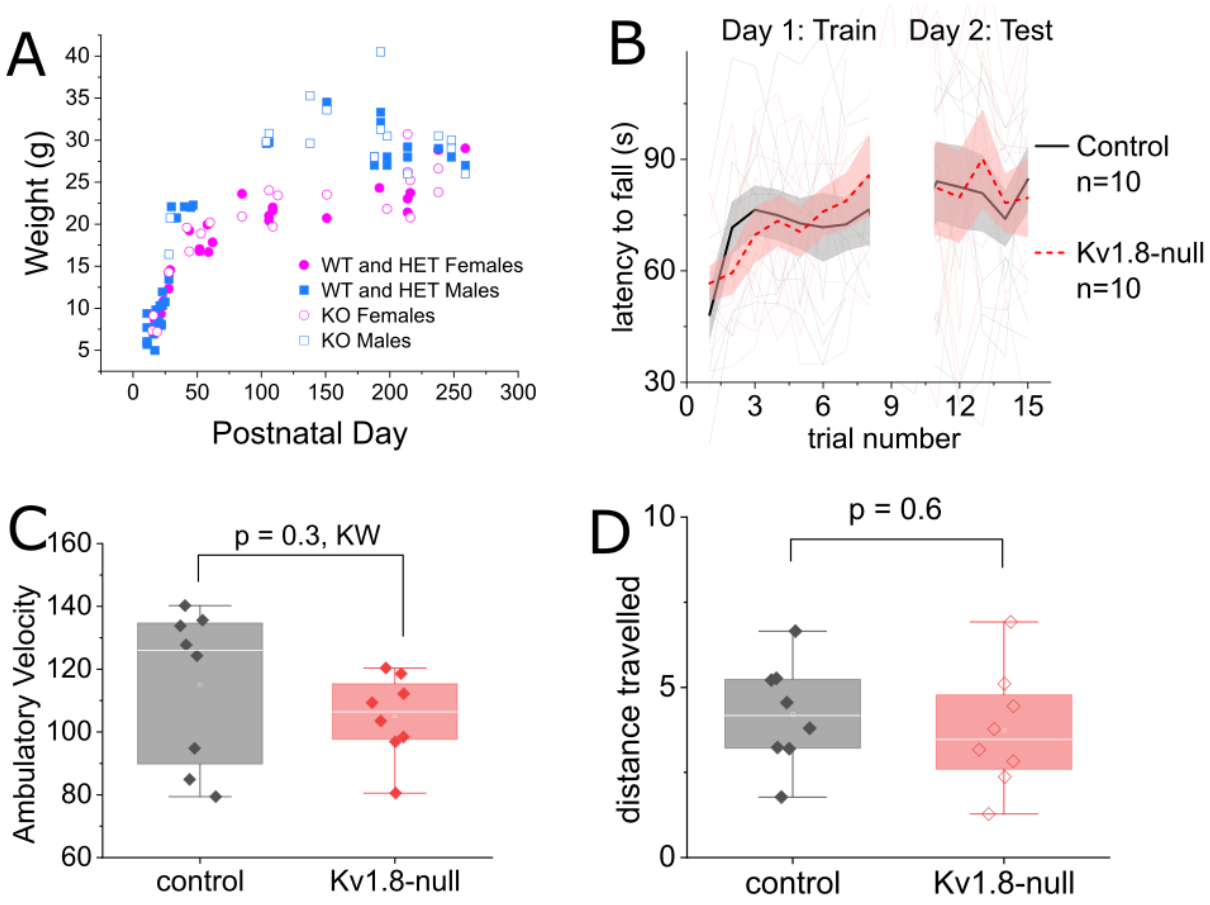

Supplemental Figure S3.4. Kv1.8-null mice have normal weight, motor learning, and motor abilities. (**A**) Weight developed normally. (**B**) Rotarod learning curve was similar for control and Kv1.8-null mice (shaded SEM). (**C**) Average ambulatory velocity and (**D**) total distance travelled during 2-hour open field test.

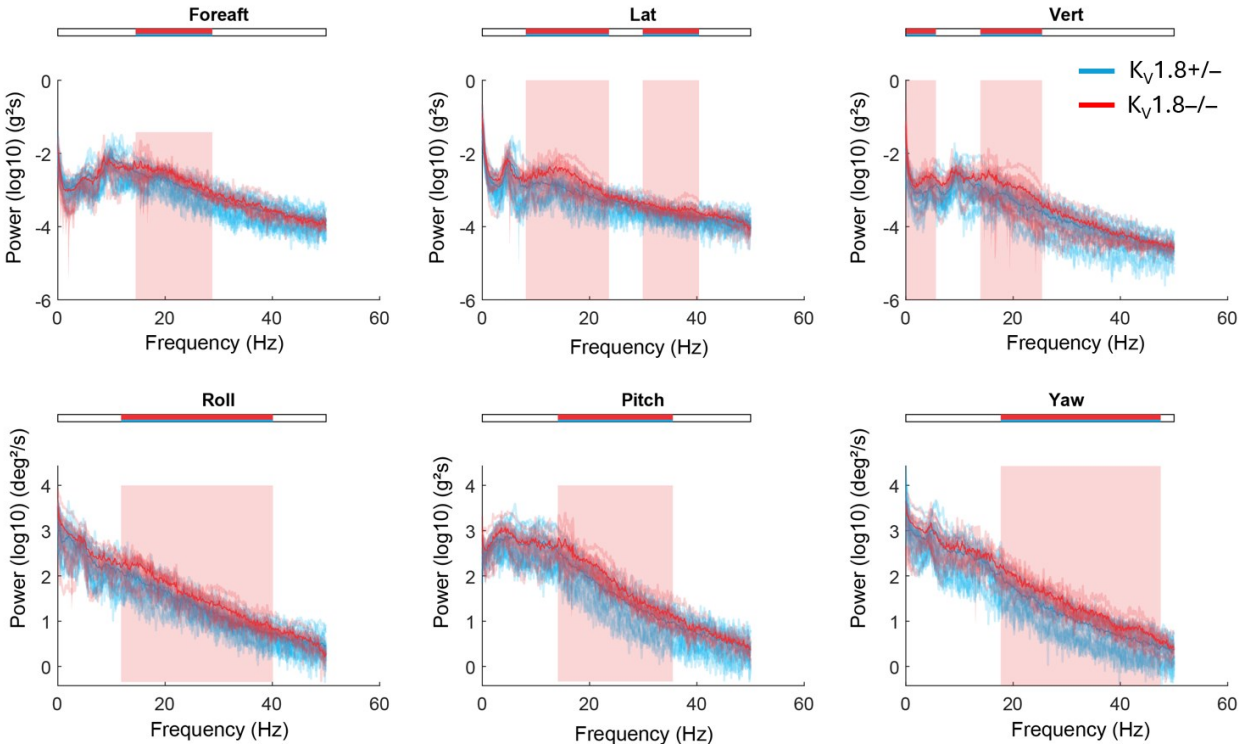

Supplemental Figure S3.5. Head motion power in $K_V1.8$-null mice and heterozygous littermates across various frequencies. N=2 $K_V1.8^{-/-}$ males, N=5 $K_V1.8^{+/-}$ males.

Supplemental Table S3.2. K_V1.8-null mice had normal motor abilities. Mean ± SEM. g is effect size, Hedge's g. KWA is Kruskal-Wallis ANOVA.

Grip strength			
K_V1.8	Grip strength (g) [a]	N animals	Age (median, range)
+/+	180 ± 10	6	142, 54-252
+/–	184 ± 9	12	149, 54-282
–/–	173 ± 8	12	134, 54-252

Power: 0.39

[a] +/– vs +/+: 2-way ANOVA, p = 0.998;
–/– vs +/+: 2-way ANOVA, p = 0.62;
–/– vs +/–: 2-way ANOVA, p = 0.45

Gait						
K_V1.8	Forepaw angle (degrees) [b]	Hindpaw angle (degrees) [b]	Forepaw stance width (mm)	Hindpaw stance width (mm)	N animals	Age (median, range)
+/+	24 ± 2	24 ± 2	7.3 ± 0.5	13 ± 0.9	3	68, 68-73
+/–	22 ± 0.5	26 ± 1	7.5 ± 0.2	13.3 ± 0.2	13	88, 75-211
–/–	22 ± 0.5	24 ± 1	7.6 ± 0.1	12.9 ± 0.3	12	84, 70-211
Power:	0.39	0.16	0.14	0.22	Sex n.s.	

[b] Genotype power = 0.39; Sex power = 0.45

Rotarod in the light			
K_V1.8	Latency to fall (s)	N animals	Age (median, range)
+/–	80 ± 7	5F, 5M	
–/–	82 ± 9	5F, 5M	
Power:	0.054, p = 0.85		

APPENDIX C

MODEL PARAMETERS FOR CHAPTER 4

Table S4.1. Model parameters of an expanded circuit of realistic voltage-clamp experiment in Figure 4.5.

Symbol	Value	Description
General		
t		Time variable
Capacitance		
C_f	0.3 pF	Feedback shunt capacitance (Lei et al., 2019)
C_m	5 pF	Membrane capacitance (Martin et al., 2024)
C_p	3-5 pF	
Current		
I_{in}		Voltage-clamp current
I_{ion}		Whole-cell ion channel current
I_{leak}		Leakage current through imperfect seal
I_m		Membrane current
I_{out}		Recorded current
Resistance		
R_f	500 MΩ	Feedback resistance (medium current gain on HEKA EPC 10)
R_S	10 MΩ	Series resistance between pipette electrode and cell (Martin et al., 2024)
R_{seal}	0.5-10 GΩ	Seal resistance of the pipette tip
Time constant		
τ_a	50 μs	Membrane access time constant, $\tau_a = R_s C_m$
τ_{sum}	40 μs	Response time of the summing amplifier (Lei et al., 2019)
τ_{clamp}	10 μs	Voltage-clamp time constant, $\tau_{clamp} = (1 - \alpha)^* \tau_a$
τ_z	150 μs	Transconductor time constant, $\tau_z = R_f C_f$
Voltage		
V_{cmd}		Command voltage, follows the voltage-clamp protocol
V_{clamp}		Clamp voltage
V_m		Membrane potential
V_{off}		Offset voltage, such as amplifier offsets, electrode offsets, junction potentials
V_{out}		Recorded voltage, $V_{out} = I_{out} R_f$
V_p		Pipette potential

Table S4.2. Ion channel parameters for model in Figure 4.5.

Symbol	Value	Description
$g_{K,L}$		
g_{max}	300 nS	Maximal conductance
V_{half}	–84 mV	Midpoint voltage activation (Martin et al., 2024)
dV	5 mV	Slope factor of voltage-dependence
τ_{act}	300 ms	Time constant of activation
E_K	–86 mV	K^+ reversal potential
g_{MET}		
g_{max}	3 nS	Maximal conductance (Chapter 3)
X_{half}	0.3 μm	Midpoint displacement activation (Chapter 3)
dX	0.2 μm	Slope factor of displacement sensitivity (Chapter 3)
τ_{Act}	50 μs	Activation time constant
τ_{Adapt}	10 ms	Adaptation time constant (Chapter 3)
E_{met}	2.6 mV	I_{MET} reversal potential (Kros et al., 1992)
Leak through seal		
E_{Leak}		V_m
g_{Leak}	2 nS	Lei et al., 2019; $1/R_{Seal}$